2015

Constitutive Modeling and Experiments for the Micro and Nano Behaviors in Metals

Cheng Zhang
Louisiana State University and Agricultural and Mechanical College

CONSTITUTIVE MODELING AND EXPERIMENTS FOR THE MICRO AND NANO BEHAVIORS IN METALS

A Dissertation

Submitted to the Graduate Faculty of the
Louisiana State University and
Agricultural and Mechanical College
in partial fulfillment of the
requirements for the degree of
Doctor of Philosophy

in

The Interdisciplinary Program
in Engineering Science

by
Cheng Zhang
B.E., University of Science and Technology of China, 2008
May 2016

TO MY BELOVED PARENTS

WHO NEVER END PATIENCE AND CONTINUOUS ENCOURAGEMENT

ACKNOWLEDGEMENTS

Firstly, I would like to thank my advisor Boyd Professor George Z. Voyiadjis for his patient guidance and solid support. Professor Voyiadjis introduced me into the world of scientific research. His mentorship was paramount in providing me with a well-round experience throughout my doctoral program. Without him, this work would never have started and not to mention the completion.

Secondly, I would like to thank my doctoral committee members: Dr. Wen Jin Meng, Dr. Dorel Moldovan, Dr. Guoxiang Gu and Dr. Kemin Zhu for their support and patience in reading this dissertation and supervising my general exam and final exam. Thank my committee for their pertinent comments and valuable advice.

I would also like to thank all the members of the advanced Computational Solid Mechanics (CSM) Laboratory: Dr. Babur Deliktas, Dr. Adam Lodygowaski, Dr. Danial Faghihi, Dr. Navid Mozaffari, Mohammed Yousef, Mohammadreza Yaghoobi, Aref Samadi-Dooki, Leila Malekmotiei, Yooseob Song and Reza Namakian for their companionship in providing an excellent working environment.

Last but certainly not least, I would like to thank my parents for their great support and love. They helped me through all the hard times. I am very grateful for the birth of my daughter Jessie on my way to my PhD. With my wife and Jessie, it feels like home when I spent time with them.

TABLE OF CONTENTS

ABSTRACT

This work addresses the micro- and nano-behaviors in metals through constitutive modeling and experiments. The size effect encountered during nanoindentation experiments, which is known as indentation size effect (ISE), is investigated for metal materials. The ISE is believed to be related with the strain gradient at small indentation depths. Geometrically necessary dislocations (GNDs) are formed in order to accommodate the strain gradient, which results in the increase in the material hardness. The grain boundaries in polycrystalline materials play an important role on the material hardness during nanoindentation experiments as there is a soften-hardening segment in the curve of hardness as a function of the indentation depth. The grain boundaries act as barriers of the movement of dislocations that leads to an increase of the dislocation density. The increasing dislocation density gives the additional increase in material hardness, resulting in the hardening phenomenon.

The classical continuum mechanics has to be enhanced with the strain gradient plasticity theory in order to address the ISE. Using the strain gradient plasticity theory, a material intrinsic length scale parameter is incorporated. The length scale bridges the gap between the behaviors in macro-scale and the micro-/nano-scale. The ISE of different materials can be characterized using this length scale parameter. The length scale parameter is determined through the strain plasticity model, the nanoindetation experiments using continuous stiffness measurement (CSM) mode in determining the fitting parameters and the finite element method (FEM) in determining the equivalent plasticity strain in the expression of the length scale.

The rate dependency of ISE is investigated and it shows that the hardness increases with the increasing strain rate. The length scales at different strain rates are determined and they decrease with the increasing strain rate, leading to the increase in the hardness. The grain boundary effect on the hardness is verified as there is no hardening-softening phenomenon in single crystalline materials as there is no grain boundary in them. The grain boundary effect is further isolated by using bicrystalline materials. The single grain boundary is investigated through nanoindentation experiments from different distances to the grain boundary. The results show that the hardness increase as the distance decreases, providing a new type of size effect.

CHAPTER 1
INTRODUCTION

The goal of the current research is to address the mechanical behaviors in metals during nanoindentation experiments through the constitutive modeling and experimental results. This introduction chapter presents the motivation and the importance of this work, while the details are presented in the following chapters.

1.1 Problem Statement

The scientific research on the mechanical behaviors in the micro- and nano-scale has shown its great importance over the past two decades in microelectronics, nanotechnology and micro-electro-mechanical systems (MEMS). It has a significant impact on the markets such as home appliances, transportation, aerospace, defense, etc. Moreover, addressing the mechanical behaviors in metals in small scales provides the opportunity to investigate the fundamental problems in micro- and nano-mechanics and material science.

Size effect has been found in metals in small scales such as micro-bending, micro-torsion and bulge test, etc (Fleck and Hutchinson, 1997; Stolken and Evans, 1998; Chen et al., 2007; Xiang and Vlassak, 2005). The classical continuum mechanics is not able to predict the size effect encountered in the above experiments. In order to address the size effect, the classical theory needs to be enhanced with the strain gradient plasticity theory. It is known that the size effect is mainly attributed to the geometrically necessary dislocations (GNDs) and the interaction between the statistically stored dislocations (SSDs) and the GNDs. It is also known that the grain boundaries play an important role in the size effect as the mechanical behaviors in metals depend on the grain size and position of the grain boundary.

In nanoindetation experiments, it shows that the hardness is greater at smaller indentation depth. This type of size effect encountered in nanoindentaion experiments is termed as indentation size effect (ISE). It has been found that in nanoindentation experiments for polycrystalline metals, there is a harden-softening segment in the curve of hardness as a function of the indentation depth instead of the solely decreasing hardness curve. It is attributed to the interactions between the dislocations and the grain boundaries. In order to address the ISE using strain gradient plasticity, a material intrinsic length scale parameter needs to be incorporated in order to bridge the gap between the macro-scale and the micro-/nano-scale, since the classical continuum mechanics is only capable to predict the hardness in the macro-scale. In addition, in order to address the hardening-softening phenomenon, the grain boundary effect must be considered in the modeling and the experiments. It also shows in nanoindentation experiments that the hardness is temperature and rate dependent. Therefore, the temperature and rate dependency of the length scale parameter needs to be investigated. The mechanical behaviors in different metals can then be characterized by the length scale parameter.

1.2 Objectives and Fundamental Concepts

The main objective of this research is to address the mechanical behaviors in metals during nanoindentation experiments. The strain gradient plasticity theory enhanced continuum mechanics is applied in order to predict the indentation size effect, incorporating a material intrinsic length scale parameter. The determination of the length scale parameter requires the modeling from the strain gradient plasticity theory and the nanoindentation experimental results. With the material intrinsic length scale parameter, ISE in different metals can be characterized. Moreover, the grain boundary effect is considered in order to predict the hardening-softening phenomenon. The grain boundary effect and the rate dependency are also investigated in this work. The framework of this dissertation is summarized as follows:

1. Developing the constitutive relations for modeling the flow stress of metals from micro-scale and macro-scales in order to derive the expression the length scale parameter. Strain gradient plasticity theory is enhanced in the continuum mechanics in order to connect the constitutive relations between the micro-scale and the macro-scale. In the micro-scale view, the dislocations play an important role in determining the inelastic behaviors of metals and the flow stresses. According to Taylor's hardening law, the shear flow stress is related to the dislocation density. In nanoindentation experiments in the submicron level, there are statistically stored dislocations (SSDs) generated from the plastic deformation. There are also geometrically necessary dislocations (GNDs) due to the inhomogeneous plastic flow from the strain gradient. Therefore, the flow stress in the micro-scale view is related to the coupling the GND density and the SSD density. In the macro-scale view, according to the strain gradient plasticity theory, the plastic strain at a point is not only dependent on the local counterpart at this point but also dependent on the strain gradient in the neighboring space. This means the total plastic strain is a coupling between the strain at the local point and the strain gradient. Because of the presence of the strain gradient, a length scale parameter is required in order to characterize the effect of the strain gradient and to maintain the dimension consistency at the same time. The flow stress can be derived in the macro-scale from the plastic strain, which means the flow stress in the macro-scale level is related with material length scale. Combining the flow stresses from the macro- and the micro-scales yields the expression of the length scale that is able to predict the behaviors in both micro-scale and the macro-scale.

2. Determining the length scale parameter through the nanoindentation experiments. The expression of the length scale has several material parameters that need to be determined through nanoindentation experiments. A computational model of the material hardness is proposed as a function of the indentation depth through the length scale parameter. By comparing the computational model and the hardness curve from the experiments, the material parameters can be determined. The model for hardness is derived through the GND and SSD densities. In macro-scale, the hardness is only related to the SSDs as there are no GNDs in large scales. However, in micro-scale, the hardness is dependent on both GNDs and SSDs. Combining the expression of hardness at different scales gives the hardness as a function of the macro-hardness

and the densities of GNDs and SSDs. The GND density can be calculated by the total dislocation length and the plastic volume under the indenter as a function of the indentation depth. The SSD density can be expressed through the strain gradient plastic theory with the length scale parameter incorporated. Therefore, the model for hardness is a function of the indentation depth as it is presented from the experiments and the length scale parameter is included in the expression so as the material parameters in the length scale expression.

3. Considering the grain boundary effect in order to capture the hardening-softening phenomenon in the hardness-indentation depth curve. The interaction between the moving dislocations and the grain boundaries is believed to cause the hardening-softening phenomenon in the nanoindentation experiments. Due to the difficulty of dislocations in transferring the grain boundary, the dislocations accumulate near the grain boundary, which leads to the increase of the dislocation density so as the material hardness. A grain size parameter is included in the expression of the length scale and the model of hardness. The hardness and the length scale varies with different grain sizes, providing another type of size effect as the smaller the grain, the greater the material hardness. In order to isolate the grain boundary effect, bicrystalline metals are chosen as the experimental specimens. As there is only one grain boundary in the specimen, the parameter of the grain size is replaced with the distance between the indenter and the grain boundary. The accumulation of the dislocations varies with the different distances. The nanoindentation experiments show that the smaller the distance, the greater the material hardness, providing a size effect about the distance between the indenter and the grain boundary. By determining the length scale parameter, the behaviors for various grain boundary conditions can be characterized.

4. Determining the parameter of the equivalent plastic strain during nanoindentation using finite element method (FEM). In the expression of the length scale, there is a parameter about the equivalent plastic strain. It is difficult to determine this parameter through the experiments. Therefore, numerical simulations using FEM for the indentation problem are used in order to determine the equivalent plastic strain as a function of the indentation depth. In addition, in order to characterize the difference between crystalline structures, such as face-centered cubic (FCC) and body-centered cubic (BCC), a user-subroutine VUMAT in numerical analysis software ABAQUS is implemented in the simulation. The VUMAT provides the constitutive relations for the simulation based on a framework of a thermodynamically consistent mathematical formulation for the condition of small deformations. Using a radial-mapping algorithm, the stress-strain relations can be provided for FCC and BCC metals. From the simulation with ABAQUS with VUMAT, the expression of the equivalent plastic strain can be obtained as a function of the indentation depth.

1.3 Outline

This dissertation presents the work in the 4 following chapters with the details of development of the models, the preparation of the testing samples and the nanoindentation experimental steps and results.

In Chapter 2, it presents the details in the work of the sample preparation and the nanoindentation technology. In order to prepare the sample appropriate for the nanoindentation experiments, it requires a flat and smooth surface of the sample without the plastic deformation and the contamination. Therefore, several grinding and polishing steps are needed. Mechanical grinding is required first in order to level the surface in order to obtain a flat surface. The following mechanical polishing steps are performed in order to decrease the surface roughness in order to obtain a smooth surface. In order to remove the plastic deformation layer from the previous mechanical polishing steps, chemical-mechanical polishing steps are performed in order to remove the strain hardening effect. Finally, the vibratory polishing is required in order to remove the contamination from the previous polishing steps.

The hardness during nanoindentation experiments is determined through the Oliver-Pharr method. The hardness value is determined through the contact stiffness in the initial unloading curve. Each loading-unloading cycle gives a single value of hardness. In order to obtain a curve of the hardness versus the indentation depth, the continuous stiffness measurement (CSM) mode is required as it provides the measurement of the hardness as a function of the indentation depth at a single indenting point. The Berkovich indenter tip needs to be calibrated in order to determine the accurate values for the hardness.

In Chapter 3, the modeling and experiments of the mechanical behaviors are presented for polycrystalline and single crystalline metals. Strain gradient plasticity theory enhanced continuum mechanics is applied in order to predict the indentation size effect (ISE) encountered during the nanoindenation experiments, which incorporates a material intrinsic length scale parameter. Grain boundary effect is considered in order to predict the hardening-softening segment in the hardness curve by adding a grain size parameter in the expression of the length scale and the computational model for the hardness. Nanoindentation experiments are performed on polycrystalline and single crystalline metals. The equivalent plastic strain as a function of the indentation depth is obtained through the finite element method (FEM) using numerical software ABAQUS with the user material subroutine VUMAT implemented. By comparing the hardness as a function of the indentation depth from the computational model and the nanoindentation experiments, the material length scale parameter for each material is determined.

The rate dependency of the length scale parameter is investigated by altering the strain rate parameter in the expression of the length scale and the computational expression of the hardness. Nanoindentation experiments with different strain rates are performed on polycrystalline metals. The length scales at different strain rates are determined from the model and the experiments.

In Chapter 4, the investigation of the ISE focuses on the bicrystalline metals to isolate the grain boundary effect in order to verify the contribution of the grain boundary on the hardening-softening phenomenon. Based on the modeling for polycrystalline metals, the model is modified in order to be compatible with bicrystalline metals. The grain size parameter in the polycrystalline metals is replaced with the distance between the indenter and the grain boundary in nanoindentation experiments. Nanoindentation experiments are performed on bicrystalline metals near the grain boundary with different distances to the grain boundary. By comparing the

modified model and the experiments on the bicrystalline sample, the new type of size effect about the distance between the indented position and the grain boundary is introduced. The length scale parameter that characterizes this type of size effect is determined.

The rate dependency of the bicrystalline metal sample is investigated by performing nanoindentation experiments at different strain rates with the same distance to the grain boundary. The length scales at different strain rates are determined from the model and the experiments.

In Chapter 5, the nonlocal theory is given beginning with the integral format. The formulations are provided in both macro-scale through the thermodynamic consistent framework and micro-scale through the dislocation theory. The starting equation in determining the length scale presented in Chapter 3 is derived in this chapter. Shear band problem is taken as an example of the use of nonlocal theory in solving the numerical simulation problems.

In Chapter 6, this work is summarized and future suggestions are given.

CHAPTER 2
NANOINDENTATION TESTING AND SAMPLE PREPARATION

Instrumented-indentation testing (IIT) has been developed over the last two decades for the purpose of determining the mechanical properties of small volumes of materials. IIT employs a high-resolution actuator to push the indenter into a sample surface and a high-resolution sensor to measure the penetration results continuously. One of the great advantages of this technique is that the contact area can be obtained from the testing data alone. It is not necessary to directly image the indentation. IIT is widely applied in order to measure the properties such as the hardness and the elastic modulus.

2.1 Determination of mechanical properties from basic IIT data

As the indenter is pushed in to the material, both elastic and plastic deformation takes place, causing the formation of an impression conforming to the shape of the indenter at certain contact depth h_c. As the indenter is withdrawn, only the elastic deformation recovers, which allows one to determine the elastic properties of a material. The hardness of the testing sample is determined using the equation

$$H = \frac{P}{A} \tag{2.1}$$

where P is the load applied to the testing sample an A is the projected contact area at that load. The elastic modulus of the testing sample, E, is determined through the reduced modulus, E_r, given by:

$$E_r = \frac{\sqrt{\pi} \cdot S}{2\beta\sqrt{A}} \tag{2.2}$$

where β is a constant that depends only on the geometry of the indenter; S is the elastic stiffness of the contact that can be determined from the slope of the initial portion of the unloading curve. The elastic modulus of the testing material, E, is calculated from the reduced modulus and the elastic modulus of the indenter in the following expression:

$$\frac{1}{E_r} = \frac{1 - \upsilon^2}{E} + \frac{1 - \upsilon_i^2}{E_i} \tag{2.3}$$

where υ is the Poisson's ratio for the testing material and E_i and υ_i are the elastic modulus and Poisson's ratio of the indenter, respectively. For a diamond indenter, the elastic modulus is $E_i = 1141\ GPa$ and $\upsilon_i = 0.07$. As the Equation (2.2) is founded through the elastic contact theory that holds for any indenter that can be expressed as a body of revolution of a smooth

function, it is derived for an axisymmetric indenter and only applies to the circular contacts with $\beta = 1$. However, if different values of β are used, it has been shown that Equation (2.2) works well even when the indenter is not axisymmetric. For instance, the Vickers pyramidal indenters with square cross sections can be used with $\beta = 1.012$; the Berkovich and the cube-corner indenters that have triangular cross sections can be used with $\beta = 1.034$.

From Equations (2.1) and (2.2), it is clear that the accurate measurement of the elastic contact stiffness *S* and the projected contact area under the load *A* must be obtained in order to calculate the hardness and the elastic modulus. One of the primary distinctions between IIT and the traditional hardness testing is that the area is established from the analysis of the indentation load versus indentation depth data, rather than by imaging. The most famous method for calculating the contact area was developed by Oliver and Pharr (1992). The analytical procedure starts by fitting the unloading curve into a power-law relation as:

$$P = B\left(h - h_f\right)^m \tag{2.4}$$

where *P* is the load applied to the testing sample, *h* is the resulting penetration depth, *B* and *m* are fitting parameters determined empirically, and h_f is the final indentation depth after the unloading is complete determined by curve fitting. As the unloading stiffness is equal to the slope of the unloading curve, *S* is determined by analytically differentiating Equation (2.4) at the maximum depth of penetration h_{max} such as

$$S = \frac{dP}{dh} = Bm\left(h - h_f\right)^{m-1}\Big|_{h=h_{max}} \tag{2.5}$$

It shows from experiments that Equation (2.4) does not provide an adequate description of the entire unloading curve. It is thus prudent practice to determine the contact stiffness by fitting only the initial 25% to 50% of the unloading data.

The contact depth over which the testing material makes contact with the indenter is generally different from the total indentation depth. Therefore, the contact depth, h_c is estimated using

$$h_c = h - \frac{\varepsilon P}{S} \tag{2.6}$$

where ε is a constant which depends on the geometry of the indenter. For spherical indenters, $\varepsilon = 0.75$ and for conical indenters, $\varepsilon = 0.72$. There is empirical justification for using $\varepsilon = 0.75$ for Berkovich and Vickers indenters as well. Although Equation (2.6) is established based on the elastic contact theory, it works well even when the contact causes significant plastic deformation. As stated in Equation (2.6), one can note that the contact depth is always less than the total indentation depth. Thus it cannot account for the plastic phenomenon of pile-up.

The projected contact area, A, is calculated by evaluating an empirically determined area function at the contact depth, h_c, that is

$$A = f(h_c) = 24.56h_c^2 + C_1h_c + C_2h_c^{1/2} + C_3h_c^{1/4} + \cdots + C_8h_c^{1/128} \tag{2.7}$$

Equation (2.7) is the area function for the Berkovich indenters. The lead term is the projected area of a perfect Berkovich indenter. The rest terms describe the deviations from the geometry of the Berkovich indenter due to blunting at the tip. C_1 through C_8 are constants determined from the tip calibration.

2.2 Continuous Stiffness Measurement (CSM)

From the previous section, one can note that the hardness of a material is determined through the beginning portion of the unloading curve which means each loading-unloading cycle can only provide one value for the calculated hardness at the maximum indentation depth. In order to investigate the relation between the hardness and the indentation depth, one must perform nanoindentation experiments at different indentation depths on different points. The hardness values are determined as discrete points and one needs to connect those points into a hardness curve. There are some limitations on this method. Firstly, in order to increase the efficiency, one can only perform experiments for a certain indentation depth interval, which may cause the miss capture of the material property between each two indentation depths. Secondly, for the experiments in each indentation depth, multiple indentations must be made for statistical consideration, which increases the total number of indentations greatly. Moreover, the surface conditions must be consistent for a large area in order to be capable for the large number of indentations, which increases the difficulty for the sample preparation.

The "Continuous Stiffness Measurement (CSM)" option allows the continuous measurement of the contact stiffness during the entire loading procedure, and not just the initial unload. This is accomplished by superimposing a small oscillation on the primary loading signal and analyzing the resulting response of the system by means of a frequency-specific amplifier. CSM relies on an accurate dynamic model of the indentation machine to allow the isolation of the material response from the total dynamic response and determine the material parameters from that. From the dynamic response, the elastic contact stiffness S is determined continuously. Therefore, with the CSM option, one can dynamically obtain the hardness and the elastic modulus as a continuous function of the indentation depth.

The CSM option in the nanoindenter allows one to perform the experiments at various constant strain rates. Unlike the tension or compression tests, the strain field underneath the indenter tip is not homogeneous but is a complex strain field does not have a single value. So the strain field in IIT experiments is characterized with a single quantity, often referred to as the characteristic strain. Empirical studies in metals (Tabor, 1951) have shown that the characteristic strain can be used to correlate the hardness determined with the indentation tests to the flow

stress in uniaxial tests. For spherical indenters, the characteristic strain changes continuously with the indentation depth as

$$\varepsilon = 0.2a/R \tag{2.8}$$

where a is the radius of the residual impression and R is the radius of the indenter. The factor 0.2 in Equation (2.8) is a fitting parameter, which is used for other indenter geometries as well.

For sharp self-similar indenters (Vickers, Berkovich), the derivative of the indenter profile function is constant no matter what the load or the indentation depth is. The characteristic strain is therefore independent of the indentation depth as:

$$\varepsilon = 0.2 \cot \psi \tag{2.9}$$

where ψ is the half-included angle of the indenter for cones. For pyramidal indenters, ψ is the half-included angle of the cone that has the same area-to-depth relationship. The shape of the indentation maed from a sharp indenter is therefore the same at all indentation depths and the characteristic strain is constant. The strain rate in the experiments with a sharp indenter is therefore a measure of the velocity of the penetration of the indenter but not exactly a measure of the rate of change in the characteristic strain. The strain rate, $\dot{\varepsilon}$, in nanoindentation experiments is then defined as

$$\dot{\varepsilon} = \frac{\dot{h_c}}{h_c} \quad or \quad \dot{\varepsilon} = \frac{\dot{P}}{P} \tag{2.10}$$

Therefore, a constant strain rate in nanoindentation experiments with CSM option implies an increasing indentation tip velocity.

2.3 Tip Calibration

The accuracy of the determined hardness and the elastic modulus of the testing material relies on the accuracy of the tip area function presented in Equation (2.7). Due to the shape change on the indenter tip from blunting after prolonged use, the projected contact area varies and the area function gives various constants. In order to determine the accurate constants for the area function, tip calibration needs be performed on the standard material, fused silica. Fused silica has a well-known elastic modulus $E = 72\ GPa$ and its property is stable and does not change along with time.

In a nanoindentation experiments, the load and the indentation depth are the quantities measured direct from the sensor of the machine and they are not dependent on the tip geometry. In addition, at small indentation depth for the self-similar indenters, the material hardness exhibits an indentation size effect. However, the elastic modulus does not have an indentation size effect. Therefore, as long as the testing results provide a correct and constant value of the

elastic modulus over the whole range of the indentation depth, the constants in the area function can be determined. Using the calibrated constants, one can determine the testing hardness accurately.

The tip calibration starts with performing nanoindentation experiments on the fused silica sample at a certain indentation depth that is needed. It should be noted that the calibration procedures for the basic option and the CSM option in the nanoindenter are not the same. For the CSM option, as the elastic modulus can be determined as a continuous function of the indentation depth at a single point, it requires to perform 20 to 25 indentations on the fused silica sample at the certain indentation depth. For the basic option, as each indentation only yields one value of the hardness at its maximum indentation depth, experiments must be performed on different points with different indentation depths. For each depth, multiple tests are recommended for the statistical consideration. Once the tests are complete, check the results of the load versus indentation depth curves and delete the curves with significant deviations from the most curves as this kind of deviations may be due to the different surface conditions at different indenting points. The Analyst software is applied in order to collect the load and indentation depth data in order to determine the constants in the area function. After loading the data into the Analyst software, lead term of the area function needs to be input. For a Berkovich tip, the manufacturer provides the data sheet for each tip and the lead term may be slightly different. Since the fused silica always has the constant elastic modulus about $72\ GPa$, one needs to input this value into the software. Then the software applies the testing data to calculate the elastic modulus to be $72\ GPa$. During the calculation, the constants in the area function can be determined through the curve fitting inside the software. The constants determined from the calibration need to be input into the nanoindenter software in the tip information option. With the new constants, there should be a constant value of the elastic modulus with $72 \pm 2\ GPa$ over the entire range of the indentation depth after recalculating the tests. The calibration results show that the nanoindentation experiments can determine the correct value of the elastic modulus. The elastic modulus is related with the projected area which is described as an area function with several constants. With the correct elastic modulus determined, it means that the hardness determined through the tests is the accurate value as the accuracy of the hardness calculation depends on the projected area.

2.4 Sample Preparation

In order to accurately determine the material parameters using IIT, it is imperative that the surface must be smooth with a low surface roughness. The mechanical properties are determined from the contact area and in the governing equations, it is assumed that the surface is flat. The allowable surface roughness in IIT depends on the anticipated indentation depth of the indenter. It should be noted that the greatest problem arise when the wavelength of the surface roughness is comparable to the contact diameter. Therefore, a surface roughness is desired to be less than 10% of the indentation depth (Samuels, 2003). Since the indentation size effect is always

observed in the submicron scale and the hardening-softening in the hardness curve begins at $50\ \mu m$, it is crucial to create a surface with the roughness less than 5 nm. The roughness is also important in the surface detection and the artifacts in the hardness curves. Peaks in the rough surface could result in an erroneous surface detection during nanoindentations, leading to a horizontal shift of the hardness curve giving rise to inconsistent occurrence of the anticipated hardening-softening phenomenon. This would make it impossible to conclude whether the indentation depth at which the hardening-softening phenomenon occurs is actually different between experiments or if the differences are caused by errors in the measurement.

In order to make sure the mechanical properties of the base material are measured instead of the properties of a work hardened material, the sample surface should be free of plastic deformation. The work hardening could result in the increase in the material hardness, which is difficult to be separated from the increase in hardness of the size effect and the grain boundary effect. In order to obtain a flat surface, mechanical polishing steps are applied, which leads to the plastic deformation in the new surface. This will locally change the mechanical properties at the surface thereby affecting the IIT measurement (Wang et al. 2011; Miyahara et al., 1998). The thickness of the plastic deformation layer depends on the size of the polishing abrasives and particles, the smaller the abrasives and the particles, the less thickness of the plastic deformation layer.

A preferred surface treatment starts with mechanical polishing with abrasive polishing papers with silicon carbide particles. The initial size of the particles in the polishing paper depends on the initial surface condition of the sample. The larger particles are chosen for the surface with higher roughness. The polishing using the polishing paper with a certain particle size is complete by observing the surface under the optical microscope. If the scratches are uniformly created by the current polishing step, the polishing can move to the next step with the polishing paper with a smaller particle size. Repeat the polishing in the initial step and then use smaller particle polishing paper in the next few steps. With decreasing polishing particles, the scratches become smaller. After changing to the next polishing paper, one needs to make sure that the scratches created from the previous steps are fully overridden. If there are scratches from the previous steps cannot be fully overridden using the current polishing particles, one needs to go back and use larger particles in order to override the previous scratches. The polishing paper in the first step could be the paper with 240 grits to the one with 800 grits depending on the initial surface condition. After the polishing using the paper with 1200 grits, the next step is an increasingly finer mechanical polishing with a suspension with various sizes of diamond particles. It usually starts with the suspension with $3\ \mu m$ diamond particles. The diamond particles are usually applied on a polishing cloth in a suspension with water and alcohol. Each polishing step should remove the deformed layer caused by the previous steps, leaving the deformation layer with the minimum thickness. The smaller the polishing particles chosen, the long the polishing time should be applied in order to remove the residual surface deformation from the steps with larger polishing particles. This is because the larger polishing particles induce a deformation layer with a greater thickness. The speed of removing a layer slows down as the particles become smaller.

After the final mechanical polishing step, a chemical-mechanical polishing step is required. During this step, a colloidal silica suspension with 0.05 μm sized particles is used. The chemical reaction between the suspension and the surface layer in the sample makes the sample more brittle, allowing the extremely small particles to remove the material without causing significant deformation. Small amounts of reagents may be added to the suspension in order to increase the polishing rate, without causing a significant etching effect. The chemical-mechanical should continue until the deformation layer from the mechanical polishing steps is fully removed, resulting in an almost deformation and scratch free surface.

Electro-polishing should be applied in order to obtain a truly deformation-free surface. The material removal in electro-polishing is based on oxidizing and subsequently dissolving material in an electrolyte. Therefore, it does not cause any deformation of the surface. The small deformation layer in the chemical-mechanical polishing step is completely removed, providing a surface with the same properties with the base material. As the electrical current density is greater at the surface peaks, electro-polishing has a higher removal rate at the surface peaks and smoothens the surface even further by reducing sharp surface asperities to more blunt wavelike asperities. The quality of the surface after the electro-polishing is therefore dependent on the quality of the previous polishing steps. Relatively large features such as scratches cannot be removed by the electro-polishing. The theory behind the electro-polishing is rather straightforward. However, the actual process is very sensitive to process parameters such as voltage, current, types of electrolytes and the material to be polished.

If the chemical-mechanical polishing step is performed in the vibratory polisher, the minor deformation remaining after the mechanical polishing can be removed, revealing a deformation-free surface without the need of the hazardous electrolytes required by electro-polishing (Dayton, 1963). The specimen finished using a vibratory is suitable for electron-backscatter diffraction (EBSD) or atomic force microscopy (AFM).

CHAPTER 3
MECHANICAL CHARACTERIZATION DURING NANOINDENTATION IN POLYCRYSTALLINE METALS*

3.1 Introduction

The size effects of the mechanical properties in metals such as the flow stress or the hardness have been widely investigated in the literature (Voyiadjis and Abu Al-Rub, 2004; Abu Al-Rub and Voyiadjis, 2004). The introduction of the material length scale shows its great importance in characterizing the size effects (Fleck and Hutchinson, 1993, 1997). The classical continuum mechanics (Hill, 1950) is not able to predict the size effects as it does not incorporate the material length scales.

As pointed out in many researches, the size effects of the mechanical properties are due to an increase in the strain gradient in the small deformation volume, which leads to the geometrically necessary dislocations (GNDs) (Nye, 1953). The GNDs are generated in order to accommodate the inhomogeneous plastic deformation, causing the additional strengthening (De Guzman et al., 1993; Stelmashenko et al., 1993; Fleck et al., 1994; Ma and Clark, 1995; Arsenlis and Parks, 1999; Busso et al., 2000; Gao and Huang, 2003). In order to address the size effects, the strain gradient plasticity theory are proposed by introducing the strain gradient in the constitutive relationships in order to account for the microstructural interaction (Aifantis, 1992; Zbib and Aifantis, 1992; Fleck and Hutchinson, 1997; Bammann et al., 1999; Voyiadjis and Deliktas, 2000, 2001; Voyiadjis and Dorgan, 2001; Voyiadjis et al., 2001; Wang et al., 2003). The plastic strain at a local point is assumed to be dependent not only on the strain at that point but also on the strain gradient in the neighboring volume. The representative length scale of the strain field is proposed in order to set the qualitative and quantitative behavior of the size effect. In this manner, the strain gradient plasticity enhanced continuum mechanics bridges the gap between the macro- and micro-/nano-scale by describing the behavior in small scales using the continuum theory in the large scale. This theory shows reasonable agreements with the size effects encountered at small scales through several applications such as the strengthening of twist wires with reducing diameters (Fleck et al., 1994), the strengthening in the micro-bending of beams with reducing thicknesses (Stolken and Evans, 1998; Gao and Huang, 2001; Wang et al., 2003), particle-reinforced composites (Begley and Hutchinson, 1998; Saha et al., 2001; Xue et al., 2002a), micro-electro-mechanical systems (MEMS) (Xue et al. 2002c) and indentations (Gao et al. 1999a,b; Huang et al., 2000; Guo et al., 2001; Xue et al., 2002b). The major issue in strain gradient plasticity theory is the determination of the material intrinsic length scale that scales with the strain gradient through the constitutive relations from the information of macroscopic tests as well as micro-mechanical tests. It is shown that the indentation tests may be the most

*This chapter previously appeared as [Voyiadjis, George Z., and Cheng Zhang. "The mechanical behavior during nanoindentation near the grain boundary in a bicrystal FCC metal." Materials Science and Engineering: A 621 (2015): 218-228.] and as [Zhang, Cheng, and George Z. Voyiadjis. "Rate-dependent size effects and material length scales in nanoindentation near the grain boundary for a bicrystal FCC metal." Materials Science and Engineering: A 659 (2016): 55-62.]. It is partially reprinted by permission of Elsevier.

effective tests in order to measure the length scale parameter (Begley and Hutchinson, 1998). The indentation test is able to measure the hardness of metals by pushing a hard indenter into a relatively softer material. The load to push the indenter is measured as a function of the indentation depth. Micro- and nanoindentation experiments have shown that the hardness increase with the decreasing indentation depth at small depths (McElhaney et al., 1998; Voyiadjis and Abu Al-Rub, 2004, 2005; Ma and Clarke, 1995; Voyiadjis and Peters, 2010). This phenomenon is termed as the indentation size effect (ISE) as shown in Figure 3.1. Since the ISE cannot captured by the classic continuum theory, it has been one of the motivations underlying the development of the plasticity theory in the micro-scale. The understanding of size effects and their relation with the mechanical properties of a material is desired in the applications such as thin film and multilayers, as nano- and micro-indentations are the important way in order to measure the mechanical properties (Voyiadjis and Almasri, 2009).

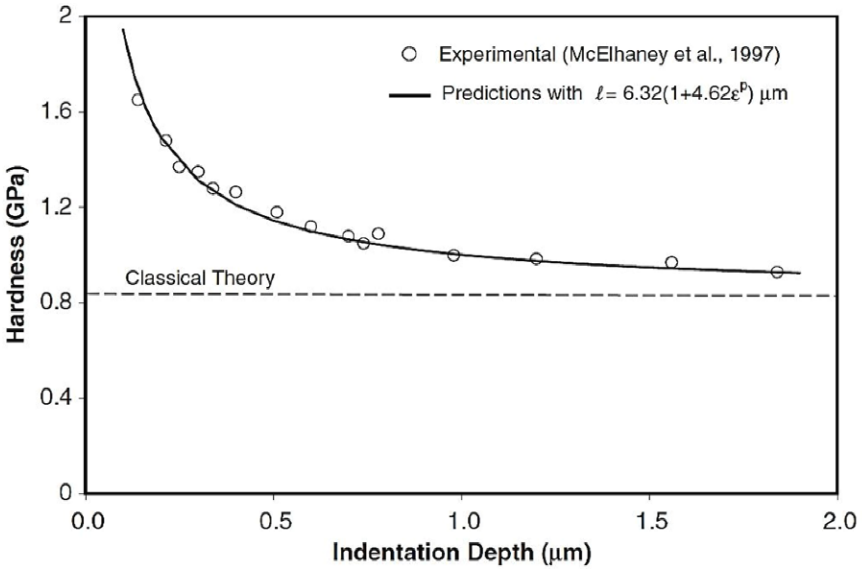

Figure 3.1 Indentation size effect (ISE) and the prediction of the hardness from the classical theory (dashed line) and the strain gradient plasticity with the length scale parameter.

The classical nanoindentation experiments show that the hardness decreases with the increasing indentation depth and approaches to the macro-hardness that can be predicted by the classical continuum theory (Figure 3.1). The increase of the hardness at small indentation depths is believed to be attributed with the GNDs and the interaction between the statistically stored dislocations (SSDs) and the GNDs. In the microscopic scale, the flow stress so as the hardness is related to the dislocation density. SSDs are generated along with the plastic deformation caused by the penetration of the indenter. However, in the small indentation depth, strain gradient is present due to the inhomogeneous deformation during the indentation, the smaller the indentation depth, the higher the strain gradient. GNDs are generated in order to accommodate this deformation, resulting in the increase of the dislocation density in the small volume. The increase of the dislocation density causes the increase in the hardness at small indentation depth.

In order to address the ISE, the classical theory needs to be enhanced with the strain gradient plasticity theory in order to include the strain gradient in the small volume. A material intrinsic length scale parameter is required in order to characterize the effects of the strain gradient and to keep the dimensions consistent. It is of great importance to determine the length scale parameter because it characterizes the size effect encountered during nanoindentations for different materials. Each material has its own intrinsic length scale.

In order to determine the material length scale through the strain gradient plasticity theory, an expression that describes the hardness as a function of the indentation depth is required because there are material parameters in the expression of the length scale and the parameters need to be determined by comparing the hardness expression and the nanoindentation results. Nix and Gao (1998) introduced the concept of the strain gradient plasticity theory on the basis of the dislocation density. They related the GND density with the indentation depth and therefore, the hardness as a function of the indentation depth can be expressed using GND density and SSD density. Voyiadjis and Abu Al-Rub (Voyiadjis and Abu Al-Rub, 2004, 2005; Abu Al-Rub and Voyiadjis, 2004) developed the method of Nix and Gao (1998) and obtained a correlation between the hardness for the spherical and conical indenters. The above studies were successful in predicting the ISE and in determining the indentation depth.

However, recent nanoindentation experiments have shown that, instead of the solely decreasing hardness with the increasing indentation depth, there is a hardening-softening segment in the hardness-indentation depth curve (Yang and Vehoff, 2007) as shown in Figure 3.2. Voyiadjis and Almasri (2008) addressed the hardening-softening phenomenon using a

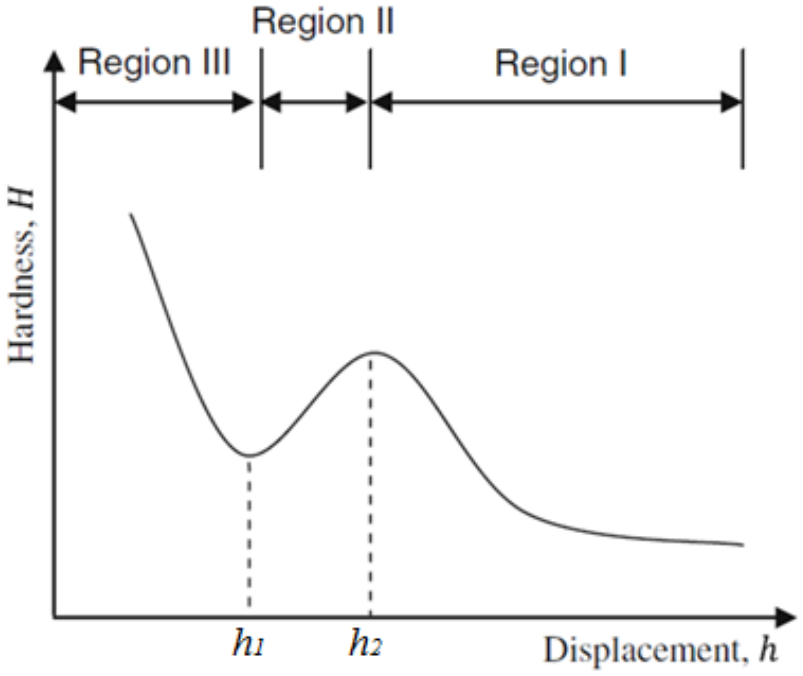

Figure 3.2 Schematic H-h curve from the experiments of Yang and Vehoff (2007).

framework of the empirical expressions for the hardness as a function of the indentation depth based on a power law relation (Almasri and Voyiadjis, 2007; Voyiadjis and Almasri, 2008, 2009; Almasri and Voyiadjis, 2010). The hardness curve was divided into three regions as the initial softening region, the following hardening region and the final softening region. Nanoindentation experiments were performed on several metals with a high surface roughness. The hardening-softening phenomenon was observed during nanoindentation experiments. This empirical framework showed a good agreement with the experimental results. However, it lacks the physical basis for the justification of these relations that describe the hardening-softening phenomenon. Voyiadjis and Peters (2010) provided the physical justification by attributing the hardening-softening phenomenon to the interaction between the dislocations and the grain boundary as shown in Figure 3.3. They indicated that the grain boundaries in polycrystalline metals act as barriers for the movement of the dislocations as there is difficulty for dislocations in transferring across the grain boundary. At very small indentation depth, there is no grain boundary effect as the plastic zone of dislocations is small (Figure 3.3, a). At this stage, the hardness curve follows the classical nanoindentations, giving a decreasing hardness as the increasing indentation depth as shown in Region III, Figure 3.2. With the increase of the indentation depth, the plastic zone expands due to the movement of dislocations and when it reaches the grain boundary, the dislocations accumulate near the grain boundaries (Figure 3.3, b), resulting in the increase in the dislocation density as well as the material hardness (Region II, Figure 3.2). Once the dislocations start to transfer across the grain boundary (Figure 3.3, c), the dislocation density decreases, leading to a decrease in hardness (Region I, Figure 3.2). They developed the expression for hardness based on a solid physical background and added the grain size parameter into the expression.

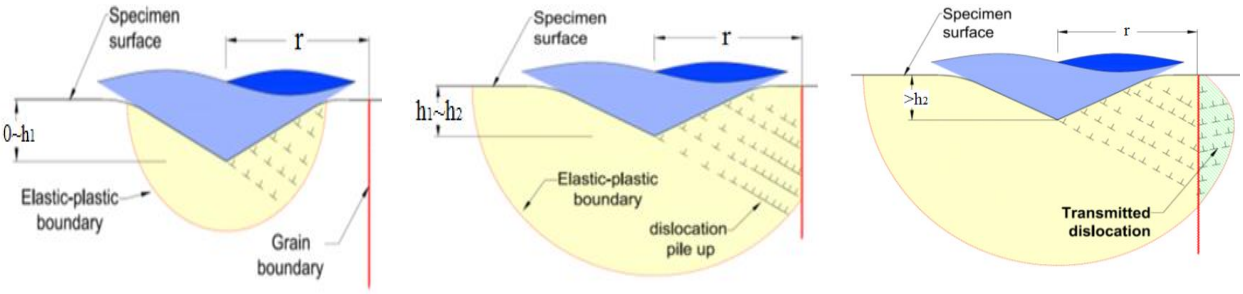

(a) (b) (c)

Figure 3.3 Interactions of the dislocations and the grain boundary.

By incorporating the expression of the hardness as a function of the indentation depth, the material length scales with constant values were obtained by several researchers using micro- and nanoindentation experiments (Begley and Hutchinson, 1998; Nix and Gao, 1998' Yuan and Chen, 2001). Voyiadjis and Abu Al-Rub (2005) observed that the material length scale is proportional with the mean free path. This observation suggests that the material length scale is not a constant material parameter but varies with the deformation of the microstructures. The

change in the length scale is also physically consistent because of the continuous modification of the material characteristics with deformation. Voyiadjis and Abu Al-Rub (2005) suggested a semi-empirical expression for the length scale as a function of the accumulated plastic strain, the grain size and the hardening exponent.

In the indentation tests, the hardness of a material depends on the indentation depth, which can be related to the equivalent plastic strain. Hardness in metals is also sensitive to the strain rate and the temperature. Koeppel and Subhash (1999) applied the elastic stress-wave propagation in a slender rod and then correlated the yield stress with the hardness in order to determine the Vickers indentation hardness. It showed that the size of the plastic zone under the indenter highly depended on yield. Anton and Subhash (2000) studied the rate effects in hardness and fracture toughness by using the same hardness tester. Lu et al. (2003) introduced a new way to deduce the dynamic rate sensitivity of materials using the measured time-resolved depth and load responses during indentation. Andrews et al. (2002) investigated the impact of a sharp indenter at low-impact velocities for elastoplastic materials. It showed that the rate dependency of a material can be involved by directly incorporating the relationship between the motion of the indenter and the flow properties of the material into the equation of motion for the indenter.

In the macroscopic scale, strain rate is known to be related to the dislocation density and the average dislocation velocity through the Orowan equation (Orowan, 1934). In addition, flow stress can be related to the dislocation density using Taylor hardening law. Staker and Holt (1972) developed a dislocation cell structure in polycrystalline oxygen-free high-conductivity (OFHC) copper by deforming tensile specimens by 10%. It has been found that the flow stress is related to the square root of the dislocation density. Senseny et al. (1978) performed experimental tests and showed that the flow stress can be influenced not only by the strain rate but also the strain rate history. Kumar and Kumble (1969) investigated the mechanical of OFHC copper at a wide range of strain rates through the dislocation mechanism. The strain rate behavior can be divided into two types: 1) if the strain rate is less than 10 s^{-1}, the dislocation motion is thermally activated over forest dislocation barriers; 2) if the strain rate is greater than $10^3\ s^{-1}$, a viscous-damping mechanism dominates. During the viscous damping, the relationship between the stress and the strain rate is linear and the mobile dislocation density is independent on both strain and strain rate. Voyiadjis and Almasri (2007) proposed two models in order to capture the strain rate sensitivity in material hardness. One of the model is a phenomenological power law model that uses the material constants related to the dependence of the flow stress of the material on the strain rate. The other model is a physically based one that is established on the dislocation behavior. In this model, when the strain rate is low (less than the order of $10^3\ s^{-1}$), the flow stress as well as the hardness is governed by the thermally activated mechanism. At high strain rates, the viscous-drag mechanism dominates and the hardness increases rapidly with the increasing strain rate. This micromechanical model shows a better agreement with the experimental results for both OFHC copper and 1018 steel at high strain rates than the power law model.

In this chapter, the mechanical behaviors in polycrystalline metals during nanoindentation experiments are investigated. The indentation size effect is captured through a material length scale parameter determined from the strain gradient plasticity theory and the nanoindentation experiments. The grain boundary effect is considered by performing experiments on polycrystalline metals and incorporating the grain size parameter into the expression of the length scale. The temperature and rate indentation size effect (TRISE) is investigated by developing a physically based TRISE model. The nanoindentaiton experiments are performed at different strain rates. In order to validate the grain boundary effect, research is made on single crystalline metals. Numerical analysis is applied with a rate dependent constitutive model in order to determine the equivalent plastic strain parameter required in determining the length scale. The material length scales are determined for different materials and at different strain rates.

3.2 Strain Gradient Theory and Material Intrinsic Length Scale

In order to address the indentation size effect using continuum theory, the classical continuum mechanics must be enhanced with the strain gradient plasticity theory, which incorporates a material length scale parameter that characterizes the size effect encountered during nanoindentations for different materials. With the length scale parameter incorporated in the constitutive equations, the enhanced continuum theory is able to predict the mechanical properties in both micro-/nano- and macro-scales.

The indentation size effect in metals can be characterized through the SSDs and GNDs and their interactions. The increase in hardness at small indentation depth is caused by the dislocation storage, which leads to an increase in the dislocation density. It is generally believed that the hardening is due to the increase in the strain gradient in small localized volumes. The presence of the strain gradient generates the formation of GNDs, which increases the dislocation density in the small volumes. The GNDs can also act as obstacles for the movement of SSDs, resulting in the additional increase in material hardness.

The SSDs are dislocations that move through the material during plastic deformation. They trap with each other in a random way and are related to the equivalent plastic strain. The GNDs are dislocations that are required for a compatible deformation in crystalline materials. They are required to accommodate the crystal lattice curvature arising from the inhomogeneous plastic deformation. In general, the GNDs are related to the strain gradients. In the indentation tests, the GNDs are generated as the indenter is pushed into the underlying substrate of the material. They are generated from the non-uniform deformation and thus give rise to an extra storage of materials defects compared with the uniform deformation at the same strain level. The storage of GNDs occurs when the characteristic length scale of the deformation is sufficiently small.

In this work, the gradient plasticity theory developed by Voyiadjis and Abu Al-Rub (2004) will be used. It is introduced by many authors (Fleck and Hutchinsion, 1993; Fleck et al., 1994; Flection and Hutchinson, 1997; Begley and Hutchinson, 1998) through the non-local weak

formulation of the conventional effective plastic strain. In general, the non-local form of strain $\hat{p}$ can be written in terms of its local counterpart p and high-order gradient terms:

$$\hat{p} = [p^{\gamma} + (l\eta)^{\gamma}]^{1/\gamma} \tag{3.1}$$

where l is the length-scale parameter to ensure dimensional consistency, p is the effective plastic strain, η is the effective plastic strain gradient of any order and γ is a material parameter.

The Taylor flow stress is used to define the shear stress that is required to untangle the interactive dislocations and to introduce a significant plastic deformation:

$$\tau = \left[\tau_S^{\beta} + \tau_G^{\beta}\right]^{1/\beta} \tag{3.2}$$

where β is a constant fitting parameter, τ_S and τ_G are given by Taylor's hardening laws related to the density of SSDs (ρ_S) and GNDs (ρ_G) respectively:

$$\tau_S = \alpha_S G b_s \sqrt{\rho_S} \tag{3.3}$$

$$\tau_G = \alpha_G G b_G \sqrt{\rho_G} \tag{3.4}$$

The parameters b_S and b_G are the magnitudes of the Burgers vectors for SSDs and GNDs respectively, G is the shear modulus and α_S and α_G are statistical coefficients which account for the deviation from regular spatial arrangements of SSDs and GNDs populations respectively.
Substituting Equations (3.3) and (3.4) into Equation (3.2) yields a general expression for the overall flow stress in terms of an equivalent total dislocation density, ρ_T:

$$\tau = \alpha_S G b_S \sqrt{\rho_T} \tag{3.5}$$

where

$$\rho_T = \left[\rho_S^{\beta/2} + (\alpha_G^2 b_G^2 \rho_G / \alpha_S^2 b_S^2)^{\beta/2}\right]^{2/\beta}. \tag{3.6}$$

The above equations are set at the micro-scale, but continuum plasticity is the macroscopic outcome from the combination of many dislocation properties at the micro- and meso-scopic scales. The flow stress can be written at the macroscopic level using a power law ($\sigma = k\hat{p}^{1/m}$). Combining this expression with Equation (3.1) yields:

$$\sigma = k[p^{\gamma} + l^{\gamma}\eta^{\gamma}]^{1/m\gamma} \tag{3.7}$$

where γ, k and m are material constants.

The non-local effects associated with the presence of local deformation gradients at a given point are incorporated into Equation (3.6) through the GND density ρ_G and into Equation (3.7)

through the strain gradient η. The gradient in the plastic strain field is accommodated by the GND density ρ_G so that the effective strain gradient η in Equation (3.1) is defined by Arsenlis and Parks (1999) as follows:

$$\eta = \frac{\rho_G b_G}{\bar{r}} \tag{3.8}$$

where $\bar{r}$ is the Nye factor that is defined as (Arsenlis and Parks, 1999):

$$\bar{r} = \frac{1}{nb}\sum_{i=1}^{n}\left|\rho_G\left(\alpha_{ij};\ \phi,\theta,\omega\right)\right|^i \tag{3.9}$$

where b is the magnitude of the Burgers vector; α_{ij} is Nye's tensor; ϕ, θ and ω are the Euler angles defining the orientation of the crystal i and n is the number of grains in the sample. Nye's factor is used to reflect the scalar measure of the GND density from the macroscopic plastic strain gradient. The plastic shear strain γ^p can be defined as a function of SSD density ρ_S as follows (Voyiadjis and Abu Al-Rub, 2004; Abu Al-Rub and Voyiadjis, 2005; Bamman and Aifantis, 1982):

$$\gamma^p = b_S L_S \rho_S \tag{3.10}$$

where L_S is the mean spacing between SSDs which is usually at the submicron order. Using the Schmid orientation tensor M_{ij} (Schmid and Boas, 1950), the plastic strain in the macroscopic plasticity theory can be defined in terms of the plastic shear strain γ^p as follows:

$$\varepsilon_{ij}^p = \gamma^p M_{ij}. \tag{3.11}$$

In relating the plastic strain at the macro-scale to the plastic shear strain at the micro-scale, an average form of the Schmid tensor is used since plasticity at the macro-scale incorporates a number of differently oriented grains into each continuum point (Aifantis, 1987; Bammann and Aifantis, 1987; Dorgan and Voyiadjis, 2003).

For proportional, monotonically increasing plasticity, the equivalent plastic strain variable p is defined as:

$$p = \sqrt{2\varepsilon_{ij}^p \varepsilon_{ij}^p/3}. \tag{3.12}$$

Combining Equations (3.10) and (3.11) and substituting the result into Equation (3.12) expresses p as a function of the SSD density as follows:

$$p = b_S L_S \rho_S M \tag{3.13}$$

with

$$M = \sqrt{2M_{ij}M_{ij}/3} \tag{3.14}$$

where M is the Schmid orientation factor that is usually taken to be 0.5 (Bammann and Aifantis, 1982).

Rewriting Equations (3.8) and (3.13) for ρ_G and ρ_S respectively, and substituting them into Equations (3.5) and (3.6) yields an expression for τ. Using Taylor's hardening law ($\sigma = Z\tau$), the flow stress can be obtained as follows:

$$\sigma = \alpha_S GZ\sqrt{b_S L_S M}\left[p^{\beta/2} + (\alpha_G^2 b_G L_S \bar{M}\bar{r}\alpha_S^2 b_S)^{\beta/2}\eta^{\beta/2}\right]^{1/\beta} \tag{3.15}$$

Comparing Equations (3.7) and (3.15) yields the following expressions:

$$\gamma = \beta/2 \tag{3.16}$$
$$m = 2 \tag{3.17}$$
$$k = \alpha_G GZ\sqrt{b_S/L_S M} \tag{3.18}$$
$$l = (\alpha_G/\alpha_S)^2(b_G/b_S)L_S M\bar{r} \tag{3.19}$$

Furthermore, Gracio (1994) indicated that in polycrystalline materials, L_S decreases when the plastic strain increases. It is equal to the grain size at the beginning of the deformation and saturates toward values in the order of micrometer in large strains. Voyiadjis and Abu Al-Rub (2005) proposed the following equation for L_S based on the work of Gracio (1994) as follows:

$$L_S = \frac{Dd}{D + dp^{1/m}} \tag{3.20}$$

where d is the average grain size in polycrystalline materials; D is the macroscopic characteristic size of the specimen; m is the hardening exponent and p is the equivalent plastic strain. Gracio (1994) also pointed out that L_S varies as the inverse of strain for single crystalline materials. He incorporated a material constant in his equation for L_S. However, the origins of nucleation of SSDs differ between single crystalline and polycrystalline materials. A dislocation structure is not formed in grains in polycrystalline materials, for instance.

On the basis of the expressions proposed by Gracio (1994) and Voyiadjis and Abu Al-Rub (2005), the equation for L_S is modified in order to account for the rate and temperature dependency (Faghihi and Voyiadjis, 2010, 2012; Voyiadjis et al., 2011). L_S is expressed as a function of temperature and the strain rate as follows:

$$L_S = \frac{g(T)}{(1 + Cp^{1/m})\left(1 + f(\dot{p})\right)} \tag{3.21}$$

$$L_S = \frac{g(T)d}{(1 + Cdp^{(1/m)})\big(1 + f(\dot{p})\big)} \tag{3.22}$$

where T is the temperature and $\dot{p}$ is the equivalent plastic strain rate. In these equations, the function $f(\dot{p})$ is defined as a power law $B(\dot{p})^q$, where q is the hardening exponent and B and C are constants added to calibrate the influence of the strain rate. The temperature dependency $g(T)$ is expressed through the Arrhenius equation as $Ae^{(-E_r/RT)}$, where A is a pre-exponential factor, R is the gas constant, E_r is the activation energy and T is the temperature in Kelvin. Only the latter formulation given by Equation (3.22) for polycrystalline materials includes the grain size d. Substituting these expressions for L_S into Equation (3.19) results in the following physically based description of the length scale l in terms of the equivalent plastic strain, equivalent plastic strain rate and temperature for single crystalline materials and polycrystalline materials, respectively (Voyiadjis et al., 2011):

$$l = (\alpha_G/\alpha_S)^2(b_G/b_S)M\bar{r}\left(\frac{\delta_1 e^{(-E_r/RT)}}{(1 + \delta_2 p^{(1/m)})(1 + \delta_3(\dot{p})^q)}\right) \tag{3.23}$$

$$l = (\alpha_G/\alpha_S)^2(b_G/b_S)M\bar{r}\left(\frac{\delta_1 d e^{(-E_r/RT)}}{(1 + \delta_2 d p^{(1/m)})(1 + \delta_3(\dot{p})^q)}\right) \tag{3.24}$$

However, it is noted in Equation (3.24) that for polycrystalline materials, the length scale is also a fution of the grain size d. the parameters $\delta_1, \delta_2, \delta_3$ are material constants that have to be determined from the results of the nanoindentation experiments. It can also be inferred from Equations (3.23) and (3.24) that the proposed physically based relations for single crystalline and polycrystalline materials show the agreement with the suggestions made by other researchers on the length scale parameter decreases with the hardening exponent m (Begley and Hutchinson, 1998) and increases with the grain size d (Haque and Saif, 2003) for single crystalline materials.

3.3 Determination of the Material Length Scale and the Hardening-Softening Effect

3.3.1 Derivation of the hardness expression based on the model of the temperature and rate indentation size effect (TRISE)

In order to determine the material intrinsic length scale from the experimental data, Abu Al-Rub and Voyiadjis (2004) derived the GND density and SSD density in the experiments for a conical/pyramidal indenter as follows.

The indentation profile shown in Figure 3.4 in the unloaded situation can be described as follows:

$$\omega(r) = r\tan\theta - h \;\; for \;\; 0 < r < a \tag{3.25}$$

where h is the indentation depth and θ is the angle between the indenter face and the sample surface. It is now assumed that the dislocation loops (GNDs) are equally spaced along the surface of the indentation and have a Burgers vector normal to the sample surface. One can then write the following expressions

$$\left|\frac{d\omega}{dr}\right| = \tan\theta = \frac{b_G}{s} = \frac{h}{a} \tag{3.26}$$

$$s = \frac{b_G a}{h} \tag{3.27}$$

where s is the mean spacing between the individual slip steps on the indentation surface. If λ is the total length of the injected loops between r and $r+dr$, one has

$$d\lambda = 2\pi r \frac{dr}{s} = 2\pi r \frac{h}{b_G a} dr \tag{3.28}$$

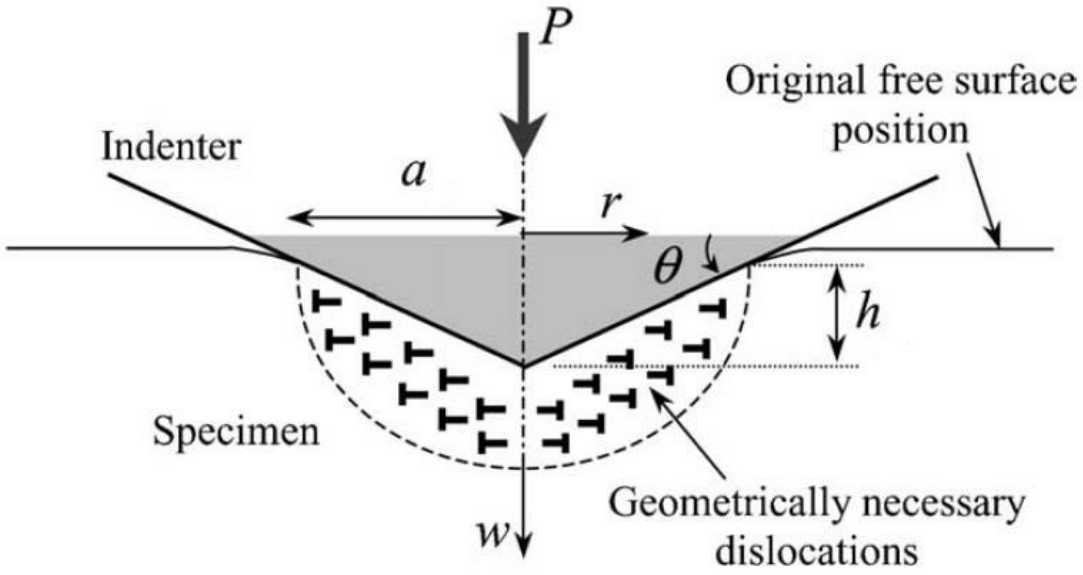

Figure 3.4 Specimen being indented by a rigid conical indenter. GNDs created during the indentation process and the relevant geometrical parameters are indicated.

Integrating from 0 to a gives the total dislocation length λ as follows:

$$\lambda = \int_0^a 2\pi r \frac{h}{b_G a} dr = \frac{\pi a h}{b_G} = \frac{\pi \tan\theta}{b_G} a^2 = \frac{\pi}{b_G} \frac{h^2}{\tan\theta} \tag{3.29}$$

Furthermore, it is assumed that the GNDs are contained within a hemispherical volume V that scales with the contact radius of the indentation profile a such that

$$V = \frac{2}{3}\pi a^3 \tag{3.30}$$

The equivalent plastic strain p can, in the case of a self-similar indenter, be expressed as follows:

$$p = c\frac{h}{a} = c\tan\theta \tag{3.31}$$

where c is a material constant of order 1. Substituting Equations (3.19) and (3.31) in Equation (3.3), the expression for ρ_S is obtained as follows:

$$\rho_S = \frac{c\bar{r}\alpha_G^2 b_G \tan\theta}{l b_S^2 \alpha_S^2} \tag{3.32}$$

Based on the work of Nix and Gao (1998) in considering the generation of GNDs under the indenter during hardness experiments, Voyiadjis and Abu Al-Rub (Voyiadjis and Abu Al-Rub, 2004; Abu Al-Rub and Voyiadjis, 2005) derived a more general framework of expressions that can be used to determine the material intrinsic length scale from micro-hardness results of spherical and pyramidal indenters. They proposed the expression for micro-hardness as follows:

$$H = Z\kappa\alpha_S G b_S\left[{\rho_S}^{\beta/2} + (\alpha_G b_G/\alpha_S b_S)^{\beta}{\rho_G}^{\beta/2}\right]^{1/\beta} \tag{3.33}$$

For the hardness at greater indentation depths where there is no size effect due to the absence of strain gradients and GNDs, the micro-hardness H_0 is defined as:

$$H_0 = Z\kappa\tau_S = Z\kappa\alpha_S G b_S\sqrt{\rho_S} \tag{3.34}$$

Using Equations (3.33) and (3.34) and simplifying the results by assuming that $\alpha_G = \alpha_S$ and $b_G = b_S$, the ratio $(H/H_0)^{\beta}$ can be derived as follows:

$$\left(\frac{H}{H_0}\right)^{\beta} = 1 + \left(\frac{\rho_G}{\rho_S}\right)^{\beta/2} \tag{3.35}$$

By substituting the relations of dislocation density for conical or pyramidal indenters into Equation (3.35), the following equation can be obtained as:

$$\left(\frac{H}{H_0}\right)^{\beta} = 1 + \left(\frac{h^*}{h}\right)^{\beta/2} \tag{3.36}$$

with

$$h^* = \varsigma l \tag{3.37}$$

and

$$\varsigma = \frac{3\tan\theta}{2c\bar{r}} \tag{3.38}$$

where h^* is the material specific parameter that characterizes the depth dependence of the hardness and depends on the indenter geometry as well as the plastic flow.

Equation (3.36) implies that when the indentation data is plotted as $(H/H_0)^{\beta}$ versus $h^{-\beta/2}$, it should give a straight line with a slope of $h^{*\beta/2}$. From this, the intrinsic length scale l can be determined through Equation (3.37) as $l = h^*/\varsigma$

For single crystalline materials, the expression for the GND density can be derived from the approach of Nix and Gao (1998) in the generation of GNDs under the indenter as follows:

$$\rho_G = \frac{3\tan^2\theta}{2b_G h} \tag{3.39}$$

Substituting the above equation into Equation (3.38) with the assumption of $\alpha_G = \alpha_S$ and $b_G = b_S$ yields the expression for hardness H as a function of the indentation depth h as follows:

$$H = H_0\left\{1 + \left[\frac{3M\tan\theta}{2ch} \times \frac{\delta_1 e^{-E_r/RT}}{(1+\delta_2 p^{1/m})(1+\delta_3 \dot{p}^q)}\right]^{\beta/2}\right\}^{1/\beta} \tag{3.40}$$

where $\delta_1, \delta_2, \delta_3$ and δ_4 are material parameters that can be obtained from the experiments.

For polycrystalline materials, the equation for hardness is obtained from a different expression for the GND density ρ_G. Voyiadjis and Peters (2010) included the hardening-softening effect in the expression for H as a function of indentation depth h. They attributed the hardening effect to the obstruction of dislocation propagation by the grain boundary due to a mismatch in the lattice and the disordered structure of the grain boundary. This causes a pile-up of dislocations at the grain boundary such that the GND density is increased. With ongoing indentation however, the increased stress at the grain boundary causes the resolved shear stress

in the adjacent grain to reach a critical value and dislocations start moving in the adjacent grain and softening occurs as shown in Figure 3.3.

On the basis of the works of Yang and Vehoff (2007), the volume of the plastic zone at the onset of hardening is defined by Voyiadjis and Peters (2010) as the volume of the semi-spherical plastic zone minus the volume taken up by the Berkovich indenter such that

$$V_{plastic} = V - V_{indent} = \frac{\pi}{12} d^3 - 8.19h^3 \tag{3.41}$$

where d is the grain size and h is the indentation depth. With this new definition for the volume of the plastic zone, the expression for GND density ρ_G for a polycrystalline material can be derived as follows:

$$\rho_G = \frac{\lambda}{V_{plastic}} = \frac{\frac{\pi}{b_G}\frac{h^2}{\tan\theta}}{\frac{\pi}{12} d^3 - 8.19h^3} \tag{3.42}$$

Making use of this new GND density, the expression for the hardness H is a function of the indentation depth h of the polycrystalline material and can be derived as follows:

$$H = H_0 \left\{ 1 + \left[\frac{M\pi(h - h_1)^2}{\left(\frac{\pi}{12} d^3 - 8.19h^3\right) c \tan^2\theta} \times \frac{\delta_1 d e^{-E_r/RT}}{(1 + \delta_2 d p^{1/m})(1 + \delta_3 \dot{p}^q)} \right]^{\beta/2} \right\}^{1/\beta} \tag{3.43}$$

In this relation, $\delta_1, \delta_2, \delta_3$ and h_1 are material parameters that have to be determined by fitting this expression for the hardness to the data from nanoindentation experiments after the equivalent plastic strain p has been determined numerically (Voyiadjis and Peters, 2010; Voyiadjis et al., 2011).

Furthermore, the cyclic plasticity model (Voyiadjis and Abu Al-Rub, 2003; Voyiadjis and Basuroychowdhury, 1998) is applied in order to obtain a more accurate hardness expression. The cyclic model is applied as follows:

$$H_{new} = H_{previous} + C(h) H_{previous} \tag{3.44}$$

with

$$C(h) = \sqrt{\frac{1}{h}} \tag{3.45}$$

where $H_{previous}$ is the hardness expressions from Equations (3.40) and (3.43) for single crystalline and polycrystalline materials, respectively.

3.3.2 Derivation of the macro-hardness

In order to compare Equations (3.40), (3.43) and (3.44) with nanoindentation experiment results, the macro-hardness H_0 is required as well as its rate and temperature dependency. In order to determine H_0, the physically based model was developed based on dislocation mechanism (Almasri and Voyiadjis, 2007). This model is based on the approach that is widely applied in the literatures (Shioiri and Satoh, 1985; Kumar and Kumble, 1969; Follansbee et al., 1984).

The intrinsic drag against the dislocation motion in FCC metals is given by the following equation through the linear viscous form (Moon and Vreeland, 1968):

$$\tau b = Bv \tag{3.46}$$

where τ is the applied shear stress; b is Burgers vector; B is the damping constant or dislocation drag and v is the dislocation velocity. However, this intrinsic drag is usually very small and is expected at very high strain rates. The dominant rate-controlling mechanism of the dislocation motion is the point obstacles that can be overcome with the aid of thermal activation. The forest dislocations are the dominant point obstacles in pure metals. The mobile dislocation segments move by repeating the thermally assisted cutting of the forest dislocation, whereas the jump motion is controlled by the viscous drag.

Since the thermal cutting requires a waiting time, the motion of the mobile segments in the previously described progress is "jerky" (Shioiri and Satoh, 1985). By simplifying the unit motion of the segment, the rate of the shear strain attributable to this jerky motion of the dislocation segments is given by

$$\dot{\gamma} = \frac{Nl^2 b}{t_t + t_v} = \frac{Nl^2 b}{\nu^{-1} e^{(U_0 - lb^2\tau_f)/KT} + t_v} v \tag{3.46}$$

where t_t is the waiting time for thermally assisted cutting; t_v is the time required by one jump motion under the control of viscous drag; N is the number of mobile segments per unit volume; l is the mean distance between the forest dislocations; U_0 is the energy required to form a jog; ν is a frequency factor; K is the Boltzmann constant; B is the dislocation drag coefficient and T is the absolute temperature. Nl also characterizes the total length of the moving segments per unit volume or density of the moving dislocations (Almasri and Voyiadjis, 2007).

At lower stresses, Equation (3.46) can be approximated by the same expression given by Gilman and Johnston (1957) for the thermal activation flow, in which the flow is linear on a logarithmic scale of the strain rate. At higher stresses, Equation (3.46) is approximated as the

viscous drag flow, in which the flow stress depends linearly upon the strain rate itself. In this flow range, the motion of dislocations should be continuous. By relating the shear strain rate to the total strain rate using the Schmid factor (Schmid and Boas, 1950), the Taylor equation to transmit the tensile flow stress to the shear flow stress and the Tabor (1951) equation, one can derive the hardness for the two low and high stresses as follows:

$$H_0 = \begin{cases} \dfrac{\kappa Z}{lb^2}\left[U_0 + KT\ln\left(\dfrac{\dot{\varepsilon}}{MNlb^2\nu}\right)\right], & \dfrac{H_0 b}{\nu\kappa Z lb} e^{\{(U_0/KT)-[(lb^2H_0)/\kappa ZKT]\}} \gg 1 \\ \dfrac{\kappa ZB}{MNlb^2}\dot{\varepsilon}, & \dfrac{H_0 b}{\nu\kappa Z lb} e^{\{(U_0/KT)-[(lb^2H_0)/\kappa ZKT]\}} \ll 1 \end{cases} \tag{3.47}$$

where $\dot{\varepsilon}$ is the strain rate, T is the temperature and the rest parameters are material constants.

3.3.3 Determination of the equivalent plastic strain

In Equations (3.40) and (3.43), there is a parameter of the equivalent plastic strain p that needs to be determined in order to express the hardness as function of the indentation depth. The equivalent plastic strain in the indented volume is a complicated value and the nanoindentation experiments are not able to determine such a value. Numerical analysis using finite element method (FEM) can be applied in order to obtain the relationship between the equivalent plastic strain and the indentation depth. Initially, the axisymmetric contact problem for the elastoplastic behavior of materials subjected to spherical static indentation was studied using the FEM with mixed boundary conditions (Voyiadjis and Buckner, 1983; Voyiadjis et al., 1986). Furthermore, the nanoindentation experiments were simulated using the indentation problem using ABAQUS software (Almasri and Voyiadjis, 2007; Voyiadjis and Peters, 2010). One of the most important parts of the finite element analysis is the choice of the constitutive relation. The rate and temperature dependency can be captured through a constitutive relation that depends on the strain rate and the temperature. The physically based viscoplastic constitutive relations were developed in order to capture the rate and temperature dependent (Abed and Voyiadjis, 2005, 2007a, 2007b; Voyiadjis and Abed, 2005a, 2005b, 2006). The relations also distinct the behaviors between the FCC and BCC metals in a thermodynamic basis.

The constitutive equations are introduced based on a framework of a thermodynamically consistent mathematical formulation for the condition of small deformations (Abed and Voyiadjis, 2005; Voyiadjis and Abed, 2005a, 2005b). The formal potential is described through the Helmholtz free energy

$$\Psi = e - sT \tag{3.48}$$

where s is the specific entropy, e is the internal energy and T is the absolute temperature. The Helmholtz potential in terms of observable and internal state variables is given as

$$\Psi = \left(\varepsilon_{ij}^{e}, T, p, \alpha_{ij}\right) \tag{3.49}$$

where p and α_{ij} characterize the isotropic and kinematic hardening in plasticity/viscoplasticity respectively. For small deformation, the total strain tensor can be decomposed into the elastic component $\dot{\varepsilon}_{ij}^{e}$ and the viscoplastic component $\dot{\varepsilon}_{ij}^{vp}$ such that

$$\dot{\varepsilon}_{ij} = \dot{\varepsilon}_{ij}^{e} + \dot{\varepsilon}_{ij}^{vp} \tag{3.50}$$

Taking the time derivative of Equation (3.50) with respect to its internal variables defined in Equation (3.49) gives

$$\dot{\Psi} = \frac{\partial \Psi}{\partial \varepsilon_{ij}^{e}} \dot{\varepsilon}_{ij}^{e} + \frac{\partial \Psi}{\partial T} \dot{T} + \frac{\partial \Psi}{\partial p} \dot{p} + \frac{\partial \Psi}{\partial \alpha_{ij}} \dot{\alpha}_{ij} \tag{3.51}$$

The internal variables are determined through several fundamental laws such as the conservation of mass, balance of linear momentum, balance of moment of momentum, the first law of thermodynamics for the conservation of energy and the second law of thermodynamics which reduces to the Clausius-Duhem inequality. The Clausius-Duhem inequality is defined as

$$\sigma_{ij}\dot{\varepsilon}_{ij} - \rho\left(\dot{\Psi} + s\dot{T}\right) - q_i \frac{T_{,i}}{T} \geq 0 \tag{3.52}$$

where ρ is the mass density and q_i is the heat flux vector. Substituting Equation (3.51) into Equation (3.52) using the decomposition in Equation (3.50), gives the following thermodynamic constraint

$$\left(\sigma_{ij} - \rho \frac{\partial \Psi}{\partial \varepsilon_{ij}^{e}}\right)\dot{\varepsilon}_{ij}^{e} - \rho\left(s + \frac{\partial \Psi}{\partial T}\right)\dot{T} + \sigma_{ij}\dot{\varepsilon}_{ij}^{vp} - \rho \frac{\partial \Psi}{\partial p}\dot{p} - p \frac{\partial \Psi}{\partial \alpha_{ij}}\dot{\alpha}_{ij} - q_i \frac{T_{,i}}{T} \geq 0 \tag{3.53}$$

For arbitrary reversible changes in the observable variables, the first two terms must vanish independently. Therefore, the following thermodynamic state functions are obtained as

$$\sigma_{ij} = \rho \frac{\partial \Psi}{\partial \varepsilon_{ij}^{e}}, \qquad s = -\frac{\partial \Psi}{\partial T} \tag{3.54}$$

The remaining terms in Equation (3.54) correspond to the dissipation energy. In the case of dissipative processes, the viscoplastic potential is represented as a continuous and convex scalar function of the flux variables as

$$\Theta^{vp} = \Theta^{vp}\left(\dot{\varepsilon}_{ij}^{vp}, \dot{p}, \dot{\alpha}_{ij}\right) \tag{3.55}$$

Using the Legender-Frenchel transformation of the above potential, one is able to obtain the complementary laws in the form of the evolution laws of flux variables as

$$F = F\left(\sigma_{ij}, R, X_{ij}\right) \tag{3.56}$$

where R and X_{ij} represent the isotropic and kinematic hardening parameters. As the above potential is only attributed to the viscoplastic mechanical process, the evolution laws of the internal state variables can be obtained using the maximum dissipation principle with the Lagrange multiplier $\dot{\lambda}^{vp}$ as

$$\Omega = \Pi - \dot{\lambda}^{vp} F \tag{3.57}$$

where Π is the dissipation energy which is the remaining terms in Equation (3.54) when the first two terms varnish. The objective function Ω is maximized using the following conditions as follows

$$\frac{\partial \Omega}{\partial \sigma_{ij}} = 0, \qquad \frac{\partial \Omega}{\partial R} = 0, \qquad \frac{\partial \Omega}{\partial X_{ij}} - 0 \tag{3.58}$$

The corresponding thermodynamic flow laws are obtained by substituting Equation (3.58) into Equation (3.57) as follows

$$\dot{\varepsilon}_{ij}^{vp} = \dot{\lambda}^{vp} \frac{\partial F}{\partial \sigma_{ij}}, \qquad \dot{p} = -\dot{\lambda}^{vp} \frac{\partial F}{\partial R}, \qquad \dot{\alpha}_{ij} = -\dot{\lambda}^{vp} \frac{\partial F}{\partial X_{ij}} \tag{3.59}$$

A proper definition for the viscoplastic potential as well as the Helmholtz free energy is required in order to represent the thermodynamic consistent constitutive relations that can describe the thermodynamic behaviors of the material. A general definition of the elastic-thermoviscoplastic energy for FCC metals is given as

$$\rho\Psi = \frac{1}{2}\varepsilon_{ij}^{e} E_{ijkl} \varepsilon_{kl}^{e} + \frac{1}{3} C \alpha_{ij} \alpha_{ij} + \rho\psi(p) \tag{3.60}$$

where E_{ijkl} is the fourth order elastic tensor and both the coefficient C and function $\Psi(p)$ may depend on the strain rate.

The yield function is defined based on that the thermal activation depends strongly on the plastic strain. Therefore, using the concept of additive decomposition of the flow stress, the general form of the yield function f for FCC metals is given as follows:

$$f = \sigma_{eq} - Y_a - R_{th}(p, \dot{p}, T) \tag{3.61}$$

In the above equation, the thermal part of the flow stress is mainly related to the hardening parameter R_{th} and the athermal part is dependent on the athermal yield stress Y_a and the equivalent stress σ_{eq} that is defined as follows

$$\sigma_{eq} = \sqrt{\frac{3}{2}\left(\tau_{ij} - X_{ij}\right)\left(\tau_{ij} - X_{ij}\right)} \tag{3.62}$$

The deviatoric part of the normal stress in the above equation is defined as

$$\tau_{ij} = \sigma_{ij} - \frac{1}{3}\sigma_{mm}\delta_{ij} \tag{3.63}$$

where σ_{mm} is the hydrostatic part of stress and δ_{ij} is the Kronecker delta. The back stress X_{ij} is assumed to be independent on the strain rates.

R_{th} is affected by a coupled temperature and strain rate relation. Therefore, the dynamic rate-dependent yield surface for FCC metals is written such that it is valid for any value of the strain rate as follows:

$$f_d = \sigma_{eq} - Y_a - R\left(1 - \left(-\beta_2 T \ln\left(\eta_0^{vp}\dot{p}\right)^{1/q_1}\right)\right)^{1/q_2} \tag{3.64}$$

where β_2 is a material parameter defined in terms of the Boltzmann's constant and the Gibbs free energy at zero Kelvin temperature as $\beta_2 = k_B/G_0$; η_0^{vp} denotes the reference viscosity parameter which is the minimum value when $T \to \infty$; q_1 and q_2 are constants that define the shape of the short-range barriers with $1.0 < q_1 < 2.0$ and $0 < q_2 < 1.0$. The threshold strain hardening can be defined as

$$R = \overline{B}(1 - e^{-kp})^{1/2} \tag{3.65}$$

where $\overline{B}$ is the hardening parameter and k is the annihilation factor.

If $\psi(p)$ in Equation (3.60) is written in a form that is able to restitute adequately the relation between R and p, the rate dependent definition is given as follows:

$$\rho\psi(p) = \vartheta\bar{B}p(1 - \exp(-kp))^{1/2} \tag{3.66}$$

where the rate-dependent coefficient ϑ is defined as follows:

$$\vartheta = \left(1 - \left(-\beta_2 T \ln\left(\eta_0^{vp}\dot{p}\right)^{1/q_1}\right)\right)^{1/q_2} \tag{3.67}$$

The constitutive equations for the stress and the back stress can be written based on the potential given in Equation (3.60) as follows:

$$\sigma_{ij} = E_{ijkl}\varepsilon_{kl}^{e} = E_{ijkl}(\varepsilon_{kl} - \varepsilon_{kl}^{vp}) \tag{3.68}$$

$$X_{ij} = \frac{2}{3} C \alpha_{ij} \tag{3.69}$$

The total strain tensor ε_{ij} is additively decomposed into the elastic component ε_{ij}^{e} and viscoplastic component ε_{ij}^{vp}.

In order to obtain the non-linear evolution rules for the viscoplasticity hardening variables, it is essential to obtain the non-linear kinematic hardening rules that give a more realistic characterization of the material behaviors during deformation. A viscoplastic potential that is not equal to the yield surface is proposed as follows

$$F = f + \frac{3\gamma}{4C} X_{ij} X_{ij} \tag{3.70}$$

where γ and C are material constants for the unit consistency. In the case of dynamic yielding for FCC metals given in Equation 3.64, the variables defined in Equation (3.59) can be rewritten as follows:

$$\dot{\varepsilon}_{ij}^{vp} = \dot{\lambda}^{vp} \frac{3\left(\tau_{ij} - X_{ij}\right)}{2\sigma_{eq}} = \dot{\lambda}^{vp} N_{ij} \tag{3.71}$$

$$\dot{\alpha}_{ij} = \dot{\lambda}^{vp} N_{ij} - \frac{3\gamma}{2C} \dot{\lambda}^{vp} X_{ij} \tag{3.72}$$

$$\dot{p} = \dot{\lambda}^{vp} \tag{3.73}$$

with the normal to the yield surface that defines the direction of the viscoplastic strain given by:

$$N_{ij} = \frac{\partial f_d}{\partial \sigma_{ij}} = -\frac{\partial f_d}{\partial X_{ij}} \tag{3.78}$$

Finally, the evolution equation of the stress tensor in terms of the incremental evolution of the total and the viscoplastic strain tensor is determined by taking time derivative of Equation (3.68) as follows:

$$\dot{\sigma}_{ij} = E_{ijkl}\left(\dot{\varepsilon}_{kl} - \dot{\varepsilon}_{kl}^{vp}\right) = E_{ijkl}\left(\dot{\varepsilon}_{kl} - \dot{\lambda}^{vp} N_{ij}\right) \tag{3.79}$$

The evolution of the back stress in Equation (3.69) is given by:

$$\dot{X}_{ij} = \frac{2C\dot{\varepsilon}_{ij}^{vp}}{3} - \gamma\dot{\lambda}^{vp}X_{ij} \tag{3.80}$$

A numerical algorithm for the integration of the rate-dependent constitutive equations is required in order to update the stress and internal variables at each time step. A robust and accurate algorithm, radial-mapping algorithm, is used (Simo and Hughes, 1986; Krieg and Krieg, 1977; Ortiz and Simo, 1986). A fully implicit method based on the backward Euler scheme is used. The scheme is given, using the parameters defined above, as follows:

$$\begin{aligned}
\varepsilon_{n+1} &= \varepsilon_n + \Delta\varepsilon \\
\varepsilon_{n+1}^{vp} &= \varepsilon_n^{vp} + \Delta\lambda^{vp}N_{n+1} \\
N_{n+1} &= \frac{3(\tau_{n+1} - X_{n+1})}{2\sigma_{n+1}^{eq}} \\
X_{n+1} &= X_n + \frac{2C\Delta\lambda^{vp}N_{n+1}}{3} - \gamma\Delta\lambda^{vp}X_{n+1} \\
R_{n+1} &= R_n + \frac{\Delta\lambda^{vp}\vartheta k\left(\overline{B}^2 - 2R_{n+1}^2\right)}{2R_{n+1}} \\
\sigma_{n+1} &= \sigma_n + \Delta\sigma = E:\left(\varepsilon_{n+1} - \varepsilon_{n+1}^{vp}\right)
\end{aligned} \tag{3.81}$$

In the above scheme, n represents the number of the current time step and $n+1$ represents the next time step to step n.

By implementing the above constitutive relations into the ABAQUS simulation for the indentation problem, the equivalent plastic strain can be determined as a function of the indentation depth. Finite element simulations are performed by implementing the proposed viscoplasticity constitutive model in the commercial finite element program ABAQUS/Explicit through a user material subroutine coded as VUMAT including the radial return algorithm (Krieg and Krieg, 1997; Ortiz and Simo, 1986). In ABAQUS with VUMAT, the constitutive model is defined in a co-rotational coordinate system, in which the basis system rotates with the material. All stress and strain tensor quantities are defined with respect to the co-rotational basis system. This allows one to extend the standard finite element code with small strain to the analysis of the finite strain. Determining the material parameters of the proposed constitutive model is the important part in capturing the actual behavior of the material. As the constitutive model is dependent on both temperature and the strain rate, the stress-strain relations of the materials for different strain rates and various temperatures are required to obtain more accurate parameters. The parameters of different materials were obtained (Voyiadjis and Abed, 2006) through various experiments at different strain rates and temperatures (Tanner et al. 1999; Nemat-Nasser and Li, 1998; Voyiadjis and Abed, 2005a, 2005b, 2006; Barlat et al. 1997a, 1997b).

A cube with dimensions of 50 μm is modeled to represent the testing sample. The Berkovich is simulated on top of the cube and is modeled as a blunt pyramid (Figure 3.5). The tip of the

indenter is an equilateral triangle with 20-nm sides. The ABAQUS interaction module is used in order to model the contact between the indenter and the sample. Assigning a specific velocity to the indenter causes it to penetrate into the sample to a desired indentation depth. After the plastic deformation takes place, the indent can be viewed on the sample surface as shown in Figure 3.6. The pile-ups can be clearly visible at the sides of the indenter. This is attributable to high indentation occurrence in a small vicinity that allows the material to pile up at the periphery of the indenter. From the simulation, the equivalent plastic strain can be obtained as a function of the indentation depth.

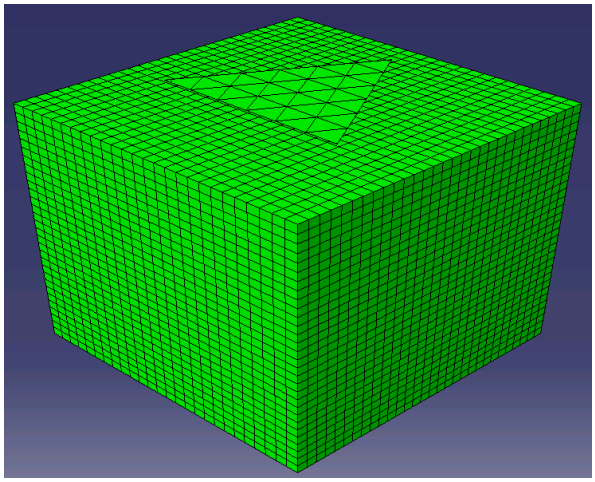

Figure 3.5 Modeled indenter and sample using the ABAQUS software before the simulation.

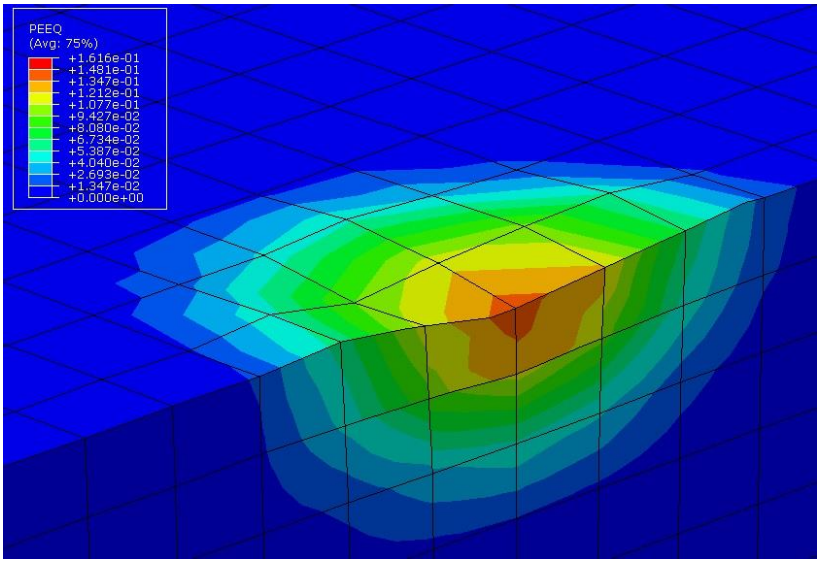

Figure 3.6. Equivalent plastic strain in contour plot after the indentation.

3.4 Nanoindentation Experiments and Sample Preparation

By comparing the hardness expression from the TRISE model and the results of the nanoindentation results, the material parameters can be determined and thus the expression of the length scale as a function of the equivalent plastic strain can be determined. In order to obtain better results through the nanoindentation experiments, especially on the purpose to capture the hardening-softening phenomenon, the surface of the testing sample must be smooth with a low roughness. Voyiadjis and Almasri (2010) performed nanoindentation experiments using the CSM option on samples that were not polished. Although it showed the hardening-softening effect in the hardness curve as a function of the indentation depth, there is a huge difference among different tests. Therefore, a hardness range was set in order to include all the testing curves. In order to obtain the hardness curves that are consistent with each other, the sample needs to be polished. For the samples used in this chapter, mechanical polishing using carbide polishing papers and the suspension with diamond particles of the 3 μm size. It shows that after the mechanical polishing, the roughness decreases greatly before the polishing is applied as shown in Figure 3.7. Nanovision option in the testing machine is applied in order to obtain the surface profile in the indented area as shown in Figure 3.8. It shows that the indented surface is smooth as the color representing the height of the surface is uniform. The pile-ups are also observed as shown in the simulations.

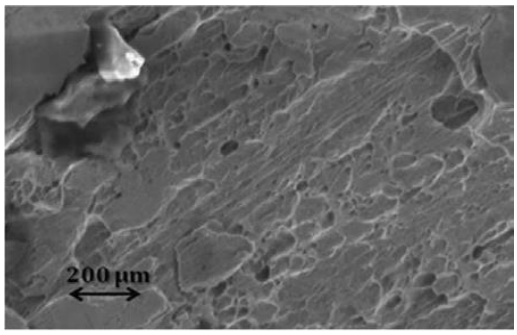

(a)

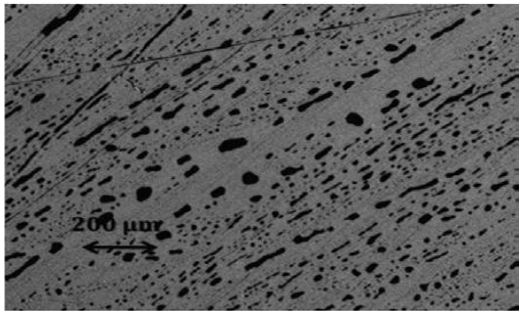

(b)

Figure 3.7. Surface of the sample (a) without polishing and (b) with mechanical polishing.

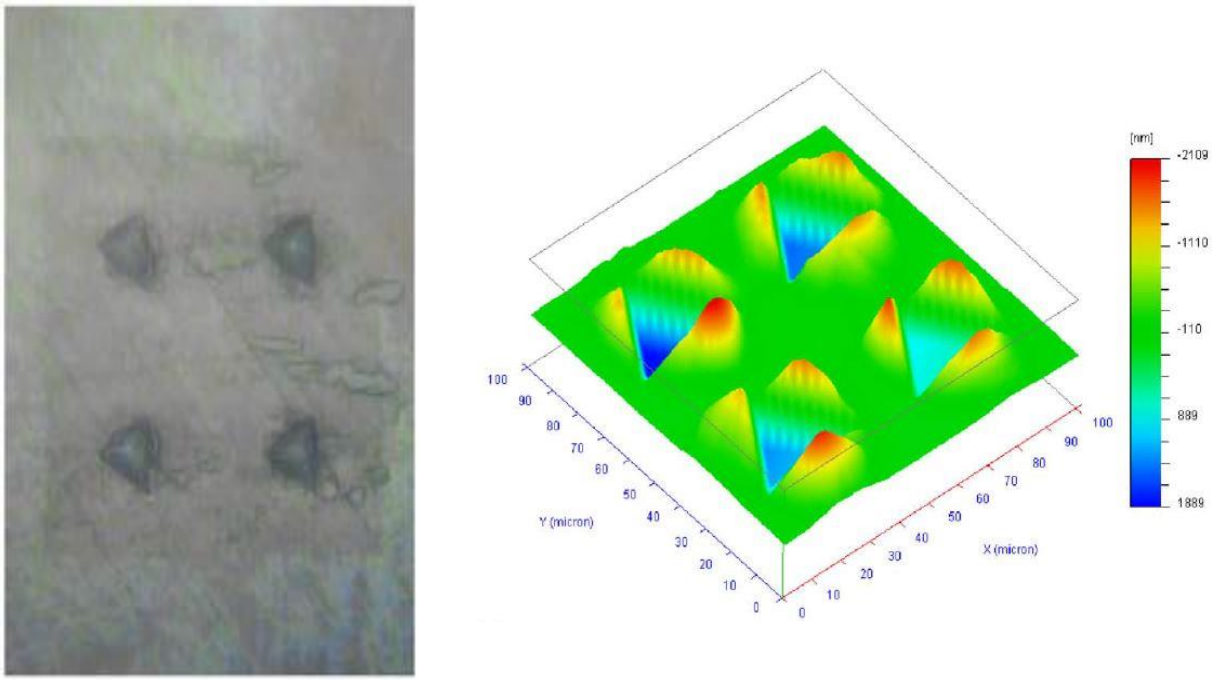

(a) (b)

Figure 3.8. (a) Microscope view of the indentations and (b) surface profile from Nanovision.

After the sample is polished, it is mounted on to sample tray of the Nanoindenter and then loaded to the stage of the machine. An optical in the Nanoindenter is used in order to find the positions for the indentations. Before performing the indentations on the desired sample, several indentations are performed on the fused silica sample. As the fused silica has a stable elastic modulus of $E = 72\ GPa$. The tests on the fused sample can determine whether the indenter tip is well calibrated by observing the elastic modulus measured for the fused silica sample. If the elastic modulus is $E = 72 \pm 2\ GPa$, it means the tip is well calibrated and the accurate value of hardness can be determined. Otherwise, a tip calibration must be followed in order to obtain the correct constants in tip area function in order to determine the hardness accurately. Before forcing the indenter into the testing sample, a microscope to indenter calibration is required in order to guarantee that the points selected under the microscope match exactly with the points that the indenter penetrates.

The nanoindentation experiments are performed using the "Continuum Stiffness Measurement (CSM)" option so that the hardness can be determined as a continuous function of the indentation depth. The CSM nanoidentation is the indentation depth control, which means the desired indentation depth can be input and the machine can stop loading once the certain depth is reached. With CSM option, the nanoindentation experiments can be performed at constant strain rates. The constant strain rates are obtained by adjusting the velocity of the loading procedure and therefore, the loading speed increases along with the indentation depth. The strain rates are numbers that can be taken as an input. As the CSM option can obtain a full hardness curve at a single indentation, one just needs to apply a few tests for the statistical consideration. Those

indentations should be spaced depending on the maximum indentation depth. In general, the spacing between two indentations should be about 20 to 30 times of the maximum indentation depth. The indentations, however, should not be made too far from each other. The surface condition changes in large areas, which may cause the inconsistent testing results.

In order to perform nanoindentation experiments at elevated temperatures, the hot stage is used and the hot stage mode of the machine is applied in order to obtain proper results. When performing tests at any temperature other than room temperature, the stage where the sample is mounted is heated so the sample is also heated. However, the indenter is still in room temperature before the penetration, resulting in the difference in temperature from the sample and the indenter. This causes the high thermal drift that cannot be corrected by the thermal drift correction segment of the testing procedure. Therefore, the CSM option cannot be used in the hot stage mode as it takes time to complete the whole procedure. In the hot stage mode, it applies the basic mode of the indentation in a short period. The basic mode is load control so the loading rate is high in order to avoid the thermal drift. Therefore, in order to obtain the hardness curve at other temperatures than the room temperature, the indentations must be made at different depths at different positions. Also for statistical consideration, at each depth, there must be multiple indentations on various positions.

3.5 Applications of the TRISE Model on Metals

3.5.1 The strain rate dependency during nanoindentations in metals

In order to investigate the rate dependency during the nanoindentation experiments, a strain rate parameter is incorporated in the expression of the length scale parameter. As the hardness expression derived from the TRISE model is a function of the length scale parameter, the hardness is also dependent on the strain rate. The hardness expression from the TRISE model needs to be compared with the results from nanoindentation experiments in order to determine the material parameters in the hardness expression and the length scale expression. Therefore, nanoindentation experiments are performed on polycrystalline copper and aluminum at different strain rates of $0.05\,s^{1-}$, $0.08\,s^{-1}$ and $0.10\,s^{-1}$. In order to isolate the strain rate effect, the temperature is set to be room temperature in the model and the grain size is presented in the model as an average grain size. The nanoindentation experiments are also performed in the room temperature. The hardness as a function of the indentation is also obtained by using the three strain rate values above. It shows that as the strain rate increases, there is an increase in the material hardness from both experiments and the model. Comparing the hardness curve from the model and the one from experiments, the material constants can be determined through curve fitting. Figure 3.9 and Figure 3.10 show that the hardness curve from the TRISE model shows a good agreement with the experimental results for both copper and aluminum.

From the comparison shown in Figures 3.9 and 3.10, the material parameters in the expression can be determined as shown in Table 3.1.

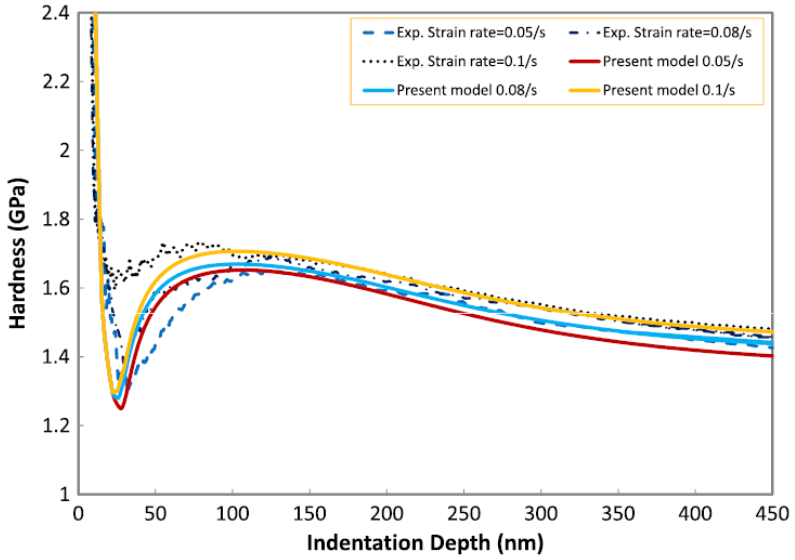

Figure 3.9 Hardness as a function of the indentation depth from TRISE model (solid lines) and nanoindentation experiments (dashed lines) for polycrystalline copper at different strain rates.

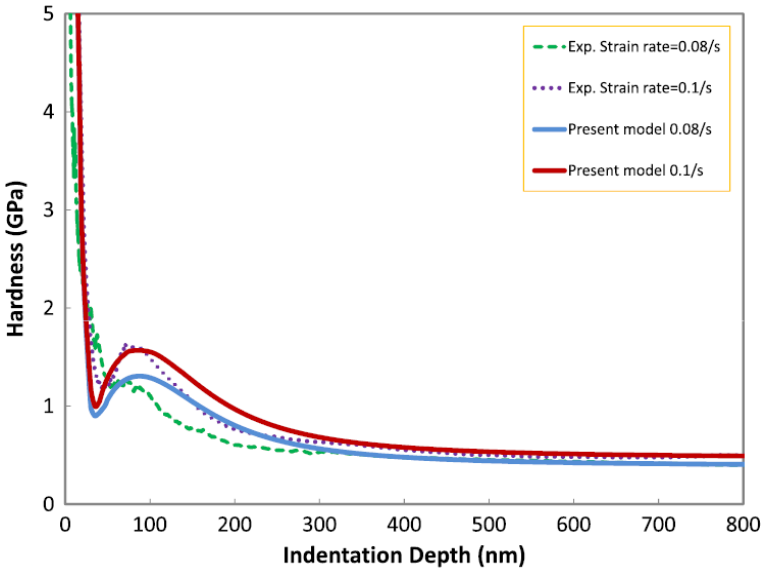

Figure 3.10 Hardness as a function of the indentation depth from TRISE model (solid lines) and nanoindentation experiments (dashed lines) for polycrystalline aluminum at different strain rates (Voyiadjis et al., 2011).

Table 3.1 Material parameters used in Equation (3.43)

Model parameters	h_1 (nm)	δ_1	δ_2	δ_3
Polycrystalline copper	26	2.1	1	0.01
Polycrystalline aluminum	41	1.9	1	0.01

Once the material parameters are determined, the expression of the material intrinsic length scale can be obtained. The rate dependency of the length scale is shown in Figure 3.11 by presenting the length scale as a function of the equivalent plastic strain at different strain rates (Faghihi and Voyiadjis, 2011). The length scales decrease with the increase of the equivalent plastic strain and approach to zero, as there is no strain gradient in large strains, providing the length scales should be equal to zero when the stain is large. It also shows that the length scale decreases with the increasing strain rate, leading to an increase in the hardness.

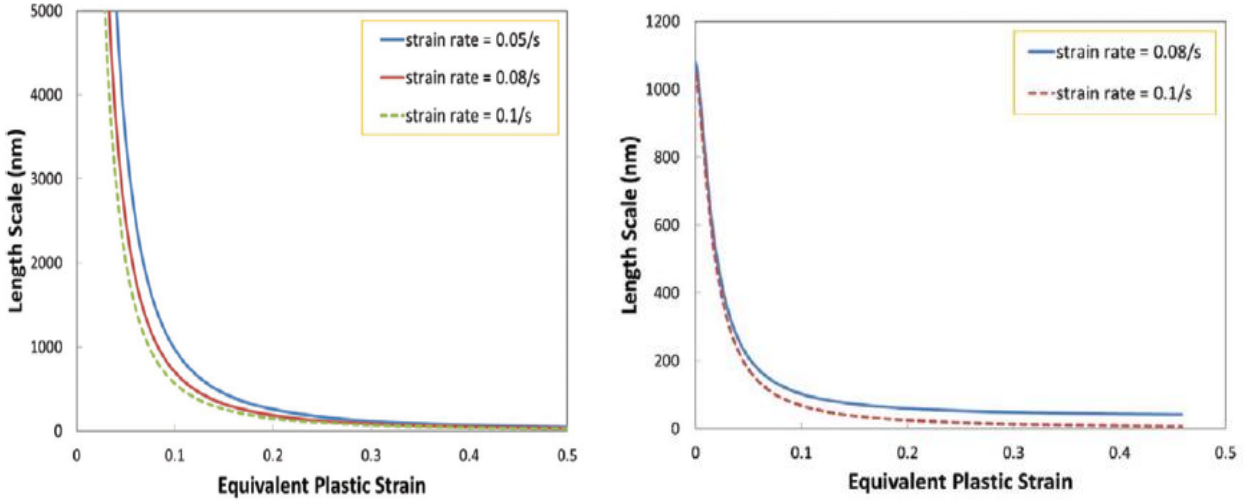

(a) (b)

Figure 3.11 Length scale as a function of the equivalent plastic strain at different strain rates for (a) polycrystalline copper and (b) polycrystalline aluminum (Faghihi and Voyiadjis, 2011).

3.5.2 Grain boundary effect during nanoindentations

The nanoindentation experiments on polycrystalline metals show the hardening-softening phenomenon from the hardness curves in Figures 3.9 and 3.10. The hardness expression from the TRISE model is capable in order to capture this phenomenon by incorporating a grain size parameter. The hardening-softening phenomenon in this research is believed to be mainly related to the interaction between the dislocations and the grain boundaries. In order to verify the attribution of the grain boundaries to the hardening-softening phenomenon, results from nanoindentation experiments of single crystalline samples are used. As there is no grain boundary in single crystalline materials, the dislocations do not accumulate during the entire indentation procedure. Therefore, there should be no hardening effect observed in nanoindentation experiments. The hardness expression from the TRISE model for single crystalline materials is used. Comparing the modeled hardness in Equation (3.40) and the results from the nanoindentations on single crystalline copper and aluminum as shown in Figure 3.12 (Voyiadjis et al., 2011), the material parameters are determined, which allows the determinations of the length scale for single crystalline materials. The fitting parameters for single crystalline models are determined from the comparison as shown in Table 3.2.

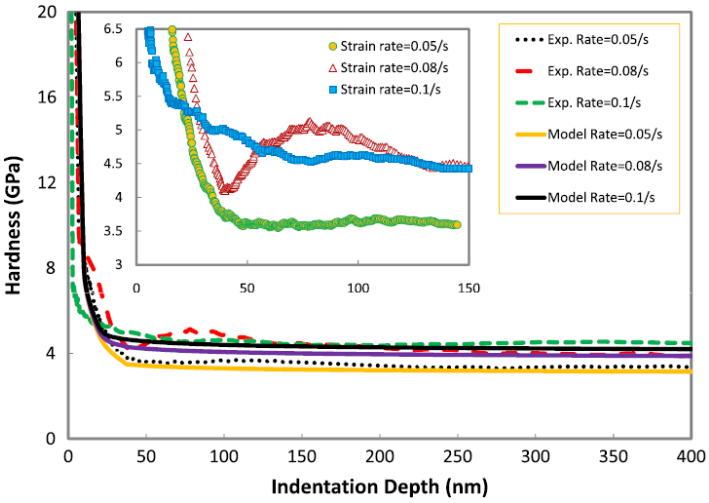

(a)

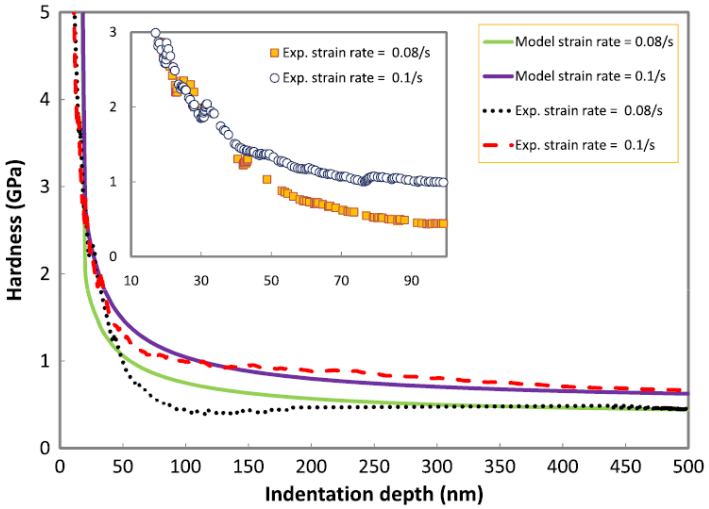

(b)

Figure 3.12 Hardness as a function of the indentation depth from TRISE model (solid lines) and nanoindentation experiments (dashed lines) for (a) copper single crystal and (b) aluminum single crystal at different strain rates (Voyiadjis et al., 2011).

Table 3.2 Material parameters used in Equation 3.40

Model parameters	h_1 (nm)	δ_1	δ_2	δ_3
Single crystal copper	32	7050	50	0.01
Single crystal aluminum	56	4000	48	0.01

With the material parameters determined, the length scale for single crystalline materials can be determined using Equation (3.23). The length scales as a function of the equivalent plastic strain for single crystal copper and aluminum are determined at different strain rates as shown in Figure 3.13 (Faghihi and Voyiadjis, 2011). The length scales in single crystalline materials

decrease with the increasing equivalent plastic strain and approach to zero when the strain is large.

The initial softening phenomenon is due to the GNDs generated due to the strain gradients in small deformation and the interaction between GNDs and SSDs. It is not dependent on the grain boundary effect. Therefore, there is indentation size effect in single crystals. However, as there is no grain boundary, the major obstacles of the moving dislocations, the dislocations do not accumulate during the indentation procedure. There is no increase in the dislocation density and thus the hardness solely decreases with the increasing indentation depth. By comparing the length scales from single crystalline and polycrystalline materials, it shows that the length scales of polycrystalline materials decreases faster with the increasing equivalent plastic strain than the ones of single crystalline materials. The values of the length scales in single crystals are much greater than the ones of polycrystallines.

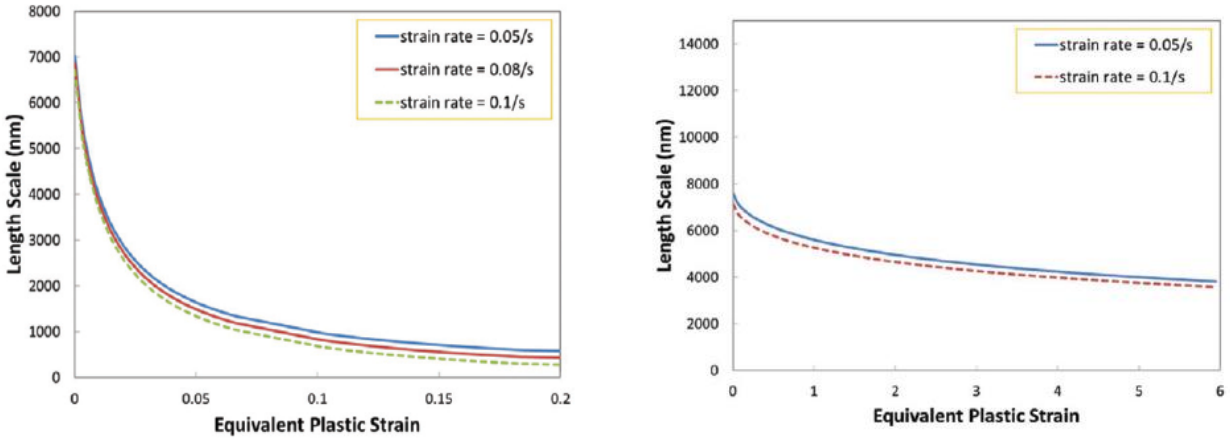

(a) (b)

Figure 3.13. Length scale as a function of the equivalent plastic strain at different strain rates for (a) single crystal copper and (b) single crystal aluminum (Faghihi and Voyiadjis, 2011).

3.6 Conclusion

The indentation size effect is captured through the strain plasticity theory enhanced continuum mechanics. The material length scale parameter is incorporated into the enhanced theory in order to characterize the indentation size effect for different materials. Physically based model is established in order to address the size effect and to determine the material intrinsic length scale. The use of the length scale allows the continuum theory to describe the mechanical behaviors in both macro- and micro-/nano-scales. The temperature and rate dependent indentation size effect (TRISE) is considered and a model for the hardness as a function of the indentation depth is derived through the length scale parameter. The material parameters in the expressions of hardness and length scale can be determine using the results from nanoindentation

experiments by curve fitting. The hardening-softening phenomenon during nanoindentations is investigated both theoretically and experimentally. In order to prove that this phenomenon is due to the interaction between the grain boundary and the dislocations, nanoindentation experiments are performed on polycrystalline and single crystalline metals. The hardness as a function of the indentation depth is also derived for polycrystalline and single crystalline materials, respectively, from the TRISE model. In order to determine the parameter of the equivalent plastic strain in the expressions of hardness and length scale, numerical simulation is applied through finite element method (FEM) using ABAQUS/Explicit software with a user material subroutine VUMAT. The VUMAT provides the temperature and rate dependent constitutive equations for FCC and BCC materials during the simulation of nanoindentation experiments for the indentation problem. By comparing the hardness curves from the TRISE model and the results of nanoindentation experiments, the material parameters are determined, allowing the length scale to be determined as a function of the equivalent plastic strain.

The research shows that the TRISE model is able to predict the indentation size effect. In addition, it is also capable in capturing the hardening-softening phenomenon. Nanoindentation experiments are performed on polycrystalline copper and aluminum. The material length scales are determined from the model and the experimental results. It shows that the length scale decreases with the increasing equivalent plastic strain. It approaches to zero when the strain value is large as there is no strain gradient in large deformation and thus the length scale is equal to zero. The material parameters from different materials differ, so the length scale can be used to characterize the mechanical behavior during nanoindentations.

The rate dependency of the length scale and the hardness is addressed both theoretically and experimentally. Nanoindentation experiments are performed on copper and aluminum at different strain rates. The parameter of the strain rate in the TRISE model can be input for different values. The experimental results and the TRISE model both show that as the strain rate increases, the hardness of materials increases. The length scales at different strain rates are determined from the model and experimental results. It shows that the length scale decreases with the increasing strain rate, leading to the increasing in hardness.

The grain boundary effect on the hardening-softening phenomenon is verified by investigating single crystal copper and aluminum. It shows in both the model and the experiments that there is no hardening-softening phenomenon in single crystalline materials as there is no grain boundary. The dislocations move without obstacles during the indentation procedure.

CHAPTER 4
MECHANICAL CHARACTERIZATION DURING NANOINDENTATION NEAR THE GRAIN GOUNDARY IN FCC METALS*

4.1 Introduction

Micro-hardness tests have been used for a long time to investigate the hardening effects due to the grain boundaries in polycrystalline materials (Westbrook and Aust, 1963; Aust et al., 1968). These tests showed that hardening effects are typically observed up to tens of micrometers from the grain boundary. No hardening can be observed in the absence of the grain boundary or other defects at this scale. The measurement of the hardening due to the grain boundary is under investigation through the nanoindentation technique. Significant hardening effects have been observed within a distance of the order of $1\mu m$ from the grain boundary under the low-load indentation experiments (Soifer et al., 2002; Soer and De Hossan, 2005).

Nanoindentation is widely employed in order to explore the mechanical properties in the submicron scales (Arzt, 1998). The hardness of the testing material decreases with the increasing indentation depth at small depths, which can be termed as indentation size effect (ISE). Recent experiments have shown that the hardness does not solely decrease with the increasing indentation but there is hardening-softening phenomenon (Yang and Vehoff, 2007). The experiments showed that the hardening-softening changed with various grain sizes. When the grain size is as much as $80\mu m$, there is no hardening effect observed. The influence of the grain boundaries in those polycrystalline samples are believed to contribute to the hardening during the experiments. The hardening effects are believed to be due to the interaction between the dislocations and the grain boundaries. The distance between the indenter tip and the grain boundary changes with different grain sizes. The experiments show that the hardness increases when the grain size decreases. Voyiadjis and Peters (2010) physically addressed the hardening-softening phenomenon encountered in nanoindentation experiments. They proposed that due to the difficulty for dislocations to transfer across the grain boundary, the dislocations accumulate near the grain boundary. The accumulated dislocation causes the increase in dislocation density, resulting in the hardening phenomenon. When the dislocations start to cross the grain boundary, the dislocation density decreases, which causes the softening phenomenon. The influence of the grain boundary on the hardening-softening phenomenon was verified by comparing nanoindentation experiment results from polycrystalline material and single crystalline material (Voyiadjis, et al., 2011). As there is no grain boundary in single crystals, no hardening-softening phenomenon is observed. The temperature and rate dependency of indentation size effect was investigated and a model based on the temperature and rate indentation size effect (TRISE) was established. The TRISE model incorporates the grain size as one of the variables in the

*This chapter previously appeared as [Voyiadjis, George Z., and Cheng Zhang. "The mechanical behavior during nanoindentation near the grain boundary in a bicrystal FCC metal." Materials Science and Engineering: A 621 (2015): 218-228.] and as [Zhang, Cheng, and George Z. Voyiadjis. "Rate-dependent size effects and material length scales in nanoindentation near the grain boundary for a bicrystal FCC metal." Materials Science and Engineering: A 659 (2016): 55-62.]. It is partially reprinted by permission of Elsevier.

expressions of hardness and length scales. The TRISE model predicted that as the grain size decreases, the hardening effect during nanoindentations is greater as shown in Figure 4.1 (Voyiadjis and Faghihi, 2010; Faghihi and Voyiadjis, 2010, 2012). The predicted hardness from TRISE model is compared with nanoindentation results for iron (Aifantis et al., 2006) and niobium (Wang and Ngan, 2004). The material length scales for the two metals are determined as shown in Figure 4.2. The length scales decrease with the decrease in the grain size.

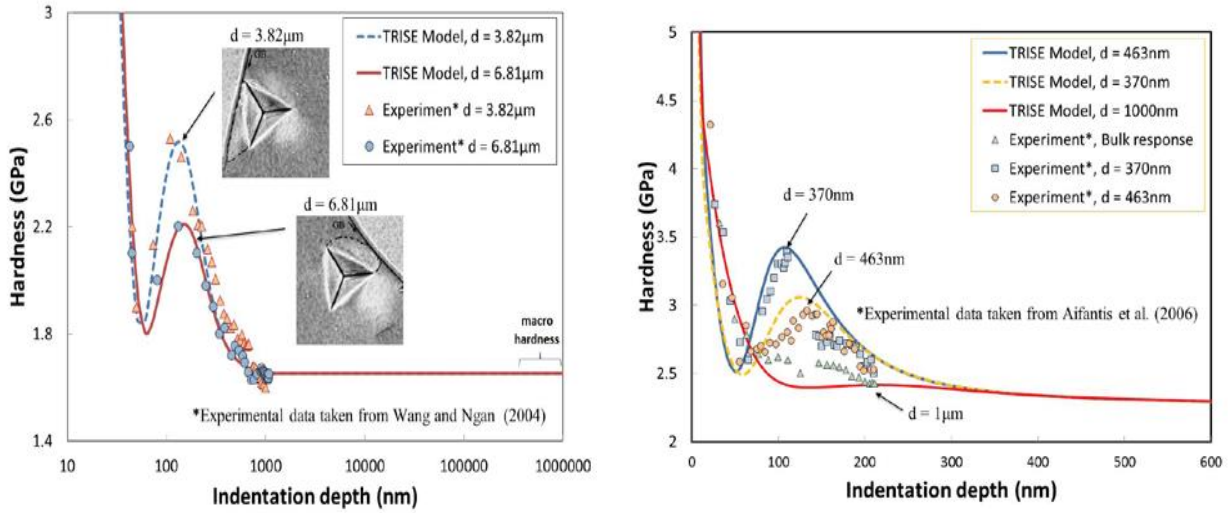

(a) (b)

Figure 4.1 Predicted hardness as a function of the indentation depth from the TRISE model for (a) niobium and (b) iron (Voyiadjis and Faghihi, 2010; Faghihi and Voyiadjis, 2010, 2012).

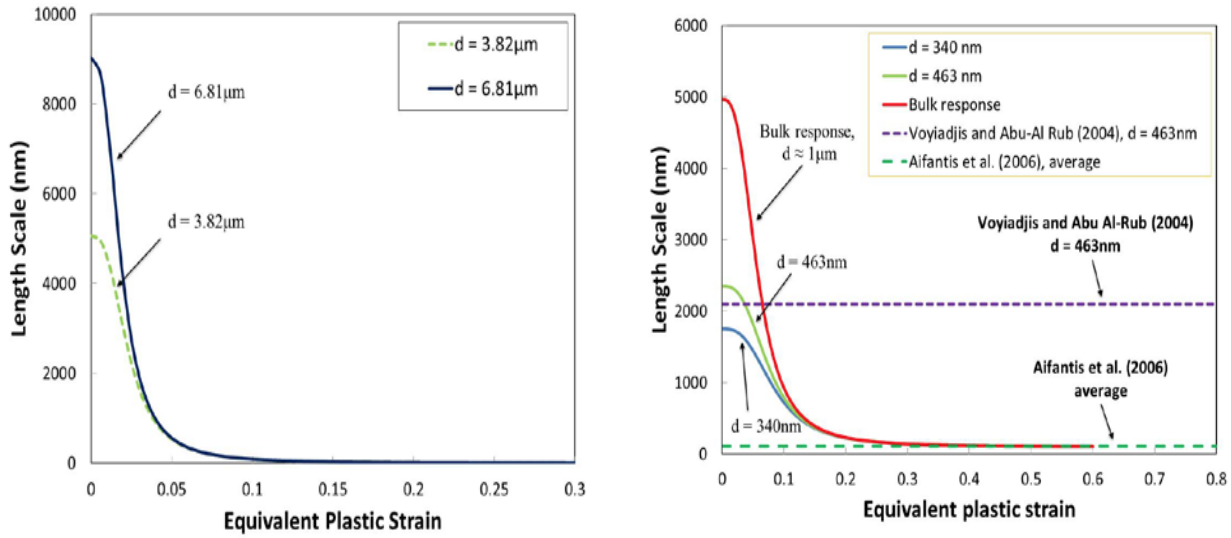

(a) (b)

Figure 4.2 Length scales for different grain sizes for (a) niobium and (b) iron (Voyiadjis and Faghihi, 2010; Faghihi and Voyiadjis, 2010, 2012).

However, in polycrystalline materials, besides the grain boundaries, there are other factors that may cause the hardening, triple junctions and the non-uniform grain size for instance. In order to investigate the influence of just the grain boundary, bicrystalline metals should be chosen. As there is only one grain boundary in a bicrystal sample, the hardening-soften phenomenon observed is attributed to the grain boundary effect. It has been shown in recent studies that typical yield excursions were observed when nanoindentation experiments were performed in the direct proximity of grain boundaries in body-centered cubic (BCC) metals (Wang and Ngan, 2004; Soer and De Hossan, 2005). It was proposed that the excursions are strain bursts due to dislocation pile-up and subsequent transmission across the grain boundary based on the load versus indentation depth curve. Nanoindentation experiments on several BCC bicrystals were performed in the close proximity of the single grain boundary at different distances from the grain boundary (Soer et al. 2005). The hardness at the maximum indentation depth increases with the decreasing distance between the indenter tip and the grain boundary, providing a new type of size effect that can be obtained through nanoindentation. The size effect related to the grain boundary can be captured. However, typical indentation size effect cannot be capture by Soer et al. (2005) as there is no information about the relationship between the hardness and the indentation depth. Voyiadjis and Zhang (2015) modified the TRISE model in order to address the size effect encountered in bicrystalline aluminum. Zhang and Voyiadjis (2016) verified the model through nanoindentation experiments on copper bicrystal and addressed the rate dependency during nanoindentation tests.

In this research, the grain boundary effect on the material hardness during nanoindentation experiments are investigated through bicrystal metals in order to isolate the influence of the grain boundary. Nanoindentation experiments are performed on bicrystal samples near the grain boundary at different distances to the grain boundary. The TRISE model is developed in order to be able to capture the size effect related to the grain boundary. As the TRISE model is able to predict the classical indentation size effect, with the modified model, the classical size effect and the size effect related to the grain boundary can be addressed in one model. By comparing the predicted hardness with the experimental results, the length scales that characterize the size effects are determined. The rate dependency is investigated from the TRISE model with different strain rate parameters and nanoindentation experiments at different strain rates. The material length scales are determined at different strain rates as well.

4.2 Determination of the Length Scales using Modified TRISE Model

In order to determine the length scales to characterize the size effects during nanoindentation, continuum mechanics enhanced with strain gradient plasticity theory in Chapter 3 is used. From the constitutive modeling, the length scale can be determined as follows:

$$l = (\alpha_G/\alpha_S)^2 (b_G/b_S) L_S M \bar{r} \tag{4.1}$$

The parameter L_S is defined as a function of the temperature, strain rate, equivalent plastic strain and the grain size for polycrystalline materials as follows:

$$L_S = \frac{g(T)d}{(1 + Cdp^{(1/m)})\left(1 + f(\dot{p})\right)} \tag{4.2}$$

In nanoindentaion experiments on bicrystal samples, the size effect related to the grain boundary is addressed by the distance between the indenter tip and the grain boundary. Moreover, in bicrystal samples, the grain size is in the macroscopic scale. Therefore, the grain size cannot be used to capture the size effect related grain boundaries. In order to characterize the grain boundary effect, the grain size *d* is replaced with the distance *r* between the indenter tip and the grain boundary as follows

$$l = (\alpha_G/\alpha_S)^2(b_G/b_S)M\bar{r}\left(\frac{\delta_1 de^{(-E_r/RT)}}{(1 + \delta_2 rp^{(1/m)})(1 + \delta_3(\dot{p})^q)}\right) \tag{4.3}$$

The hardness as a function of the indentation depth is derived from the TRISE model for bicrystals. For polycrystalline materials in Chapter 3, the GND density is calculated from the total dislocation length divided by the plastic deformation volume as follows:

$$\rho_G = \frac{\lambda}{V_{plastic}} = \frac{\frac{\pi}{b_G}\frac{h^2}{\tan\theta}}{\frac{\pi}{12}d^3 - 8.19h^3} \tag{4.4}$$

The volume of the plastic deformation is the volume of the semi-sphere with a diameter equal to the grain size minus the volume taken by the indenter in polycrystalline materials when the plastic zone expands and reaches the grain boundaries. For bicrystal samples, the interaction of the plastic zone with the grain boundary is shown in Figure 4.3 (Voyiadjis and Zhang, 2015).

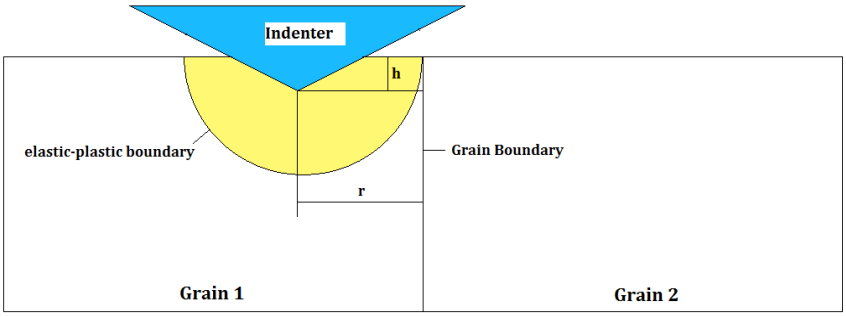

Figure 4.3 The interaction between the plastic zone and the grain boundary for a bicrystalline material.

In bicrystal samples, as the indenter penetrates, the plastic zone expands due to the movement of dislocations. When it reaches the grain boundary at an indentation depth *h*, the dislocations accumulate near the grain boundary, leading to the hardening effect. The volume of the plastic zone is equal to the semi-sphere with a radius of *r*, the distance between the indenter tip and the grain boundary. The calculation of the GND density is the same with the calculation in Chapter 3 as it depends on the geometry of the indenter. Using the new volume of the plastic deformation, the GND density in bicrystal samples are derived as follows:

$$\rho_G = \frac{\lambda}{V_{plastic}} = \frac{\frac{\pi}{b_G}\frac{h^2}{\tan\theta}}{\frac{2}{3}\pi r^3 - 8.19h^3} \tag{4.5}$$

With the GND density derived, the hardness as a function of the indentation depth for bicrystal sample is expressed as follows:

$$H = \delta_5 H_0 \left\{ 1 + \left[\frac{M\pi(h-h_1)^2}{\left(\delta_4 \frac{2\pi}{3} r^3 + 8.19(h-h_1)^3\right) c \tan^2\theta} \times \frac{\delta_1 r e^{-E_r/RT}}{(1+\delta_2 r p^{1/m})(1+\delta_3 \dot{p}^q)} \right]^{\beta/2} \right\}^{1/\beta} \tag{4.6}$$

where δ_1 through δ_5 are material parameters that need to be determined from the results of nanoindentation experiments. In order to obtain a better prediction using the model, the cyclic model is applied as shown in Chapter 3 Equations (3.44) and (3.45). The macro-hardness H_0 is obtained using Equation (3.47) in Chapter 3.

4.3 Sample Preparation

One of the specimens used in this research is an aluminum bicrystalline sample that is manufactured by the research group of Professor Jeff Kysar at Columbia University. It was grown from the melt with the Bridgman technique (Vukelic et al., 2009, 2011). It was mounted on a three circle goniometer and the orientations of its crystals were determined using Laue diffraction to within ±1°. The grain boundary between the crystals was a CSL Σ9 symmetrical tilt-type with the [110] direction parallel to the tilt axis of the adjoining grains. The specimen was cut from the as-grown bicrystal using a wire electro-discharge machine (EDM). A photo of the specimen surface is presented in Figure 4.4 and the grain boundary shown was determined during the manufacturing procedures. The other specimen is a copper bicrystal purchased in the supplying market.

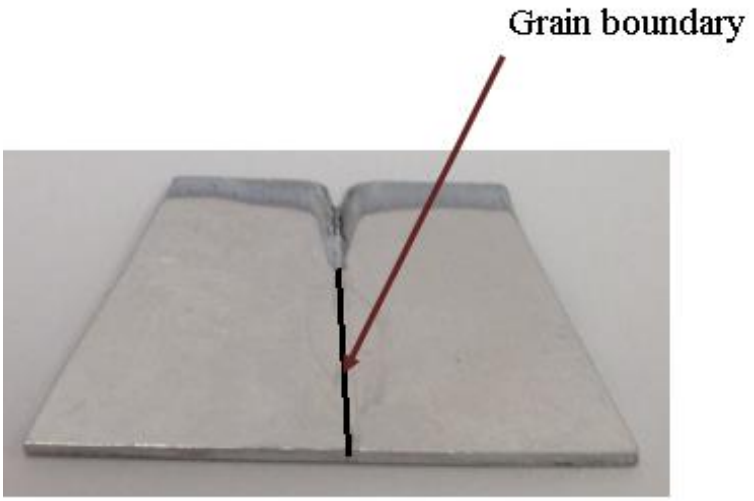

Figure 4.4 The photo of the bicrystalline specimen surface with grain boundary position shown.

To capture the ISE, one needs to verify the quality of the specimen, especially the surface roughness and oxidation layer. The oxidation layer is an unavoidable phenomenon caused by the chemical reaction between the surface of the specimen and the oxygen in the air. To limit the influence of the oxidation layer, one needs to perform the indentation tests as soon as possible after polishing the specimen. Moreover, the first 10 nm of indentation depth is not considered in the results because of the oxidation layer. In order to make the experimental results reliable, several mechanical and chemical-mechanical polishing steps were used to obtain a smooth and deformation-free surface. The specimen was firstly mechanically polished using increasingly finer polishing papers with silicon carbide abrasive particles to level the surface. Following that the mechanical polishing was performed using a polishing cloth with the suspension of 15 μm, 9 μm, 6 μm, 3 μm and 1 μm diamond particles. After each step, the state of surface was checked by visual inspection under a light microscope. Once no change of the state of the surface was observed, the polishing procedure moved to the next step. After the mechanical polishing steps residual plastic deformations remained on the surface, which would affect the results of nanoindentation experiments. Therefore, chemical-mechanical polishing was conducted with a water-based suspension containing 0.05 μm colloidal silica particles, which can remove the residual plastic deformation on the specimen surface. The chemical-mechanical polishing was performed in a vibratory polisher for 15 hours in order to make the grain boundary visible.

4.4 Nanoindentation Experiments near the Grain Noundary

After performing the mechanical and mechanical-chemical polishing steps, the grain boundary of each specimen was visibly observed as a straight line at the same position determined during manufacturing procedures. A pen mark was made on the grain boundary of the aluminum bicrystal sample and when the sample was moved under the microscope of the nanoindenter at a small magnification 10X, the grain boundary was still visible as shown in

Figure 4.5, a. However, under a 10X microscope, the distance between the indentation and the grain boundary cannot be captured. Two indentations were firstly made on two separate points on the grain boundary in order to identify the boundary. The grain boundary was then identified by a straight line connecting the two indentations as marks. After identifying the location of the grain boundary, a microscope of 40X was used and 15 indentations were performed in a straight line with 5 μm spacing at a constant strain rate of 0.05 s^{-1} as shown in Figure 4.5, b. Although plastic deformed zones of consecutive indentations are likely to overlap at such close spacing, no significant effect of interactions on the hardness measurements was found by comparing to the tests of a line of indentations with 20 μm spacing. In order to avoid the interactions among the indentations, the maximum depth of each of them was made at 500 nm. It is shown that the line of indentations crossed the grain boundary and the angle between the line of indentations and the grain boundary is 20°.

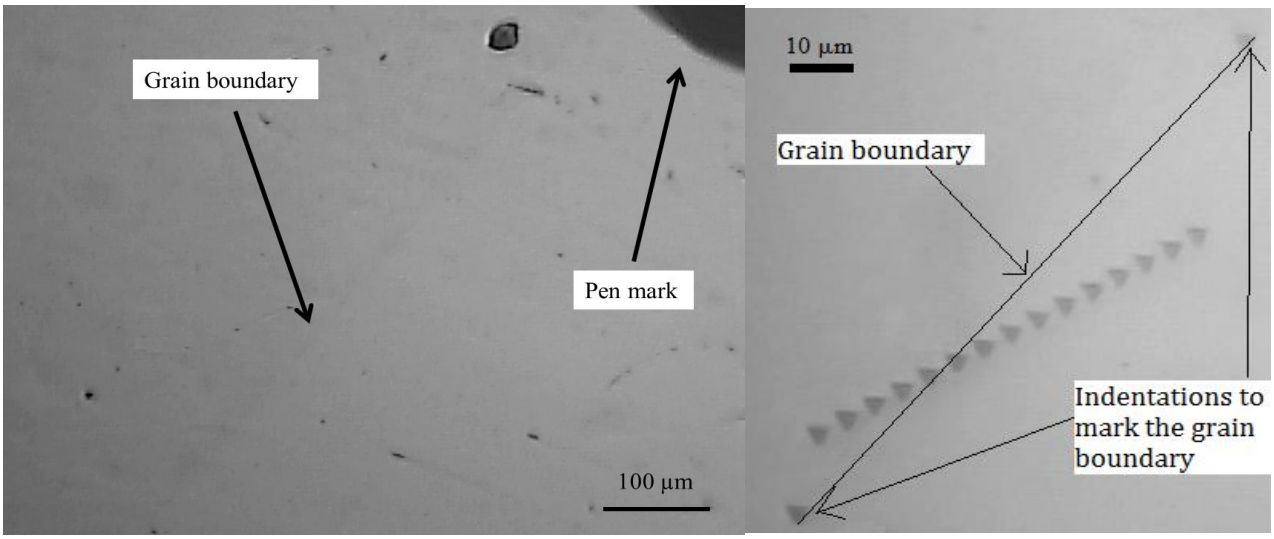

(a) (b)

Figure 4.5 (a) Visualization of the grain boundary under a 10X microscope. (b) Indentations and the grain boundary under 40X microscope. The grain boundary is represented by a straight line connecting the two indentations as marks.

Five indentations are made in the same grain to the left of the grain boundary. The crystalline structure at the positions of those five indentations is identical and the only difference is the distance *r* between the indentation and the grain boundary. These distances are shown in Figure 4.6. The corresponding experimental results for the five tests are shown in Figure 4.7. For tests 1 and 2, the hardness continuously decreases with the increasing indentation depth, showing that the material behaves as a single crystalline material and there is no grain boundary effect as the indentations are made too far from the grain boundary. For tests 3, 4 and 5, one observes both hardening and softening zones in the experimental results. It is observed that the hardening effect increases as the distance from the indentations to the grain boundary becomes smaller. This is due to the interaction between the GNDs created by the indenter and the grain boundary. At

closer distances from the grain boundary, the GNDs start to accumulate near the grain boundary for smaller indentation depths. As the indenter penetrates, there are more GNDs accumulated near the grain boundary than for indentations with higher distances from the grain boundary.

Therefore, it is clear from the experimental results that the indentations at a closer distance from the grain boundary have higher values of hardness in the hardening zone and it starts to harden at smaller indentation depths.

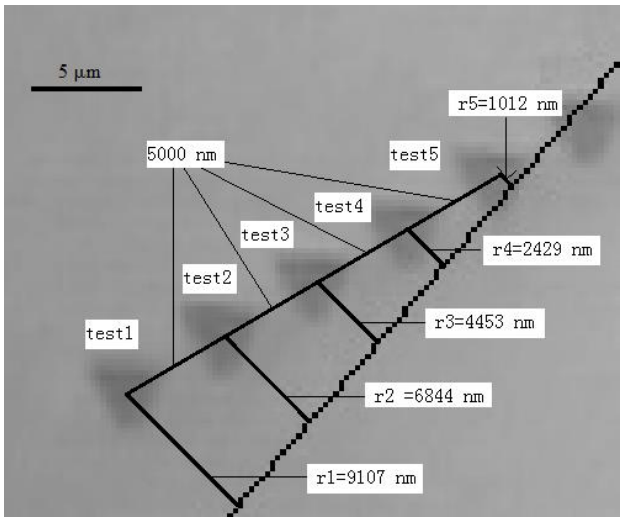

Figure 4.6 Distances from the indentations to the grain boundary.

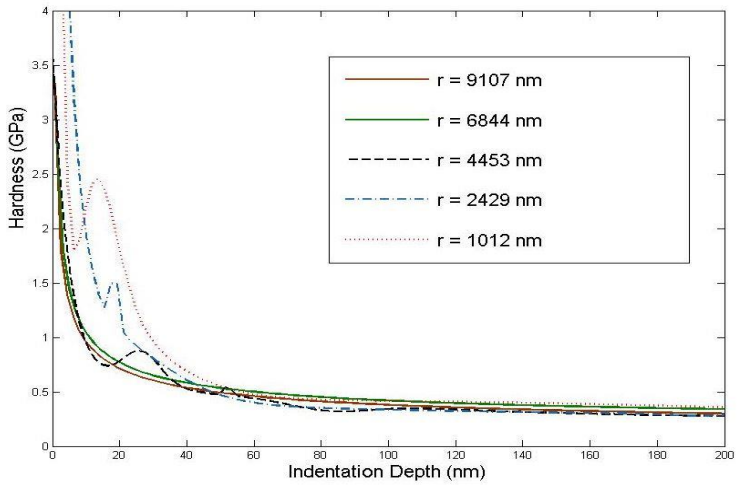

Figure 4.7 Hardness versus indentation depth curves for five indentations with different distances between the indenter and the grain boundary. The two solid curves represent the two indentations without hardening-softening effect as the two indentations were made far from the grain boundary. It shows from the three dashed curves that, as the distance of an indentation to the grain boundary becomes smaller, there is stronger hardening effect and the hardening effect starts earlier.

For the copper bicrystal, after all the polishing steps were completed, the grain boundary of the bicrystal sample was visualized under the low power microscope 10X inside the nanoindenter. However, the indentations made were small and barely visible under the low power microscope. A high power microscope 40X was required in order to observe the indentations, but the grain boundary was not visible under the microscope 40X. In this case, when the specimen was placed under the microscope 10X, two deep indentations were made right on the grain boundary in order to mark the position of the grain boundary. The grain boundary is represented by a straight line connecting the two marking indentations. With the two marking indentations, the position of the grain boundary can still be determined under the microscope 40X. A straight line of indentations were made near the grain boundary, with the angle between the line of indentations and the grain boundary to be 5°. The tests were performed using the Continuous Stiffness Measurement (CSM) option from the Nanoindenter XP. In general, the contact stiffness is required for the determination of hardness, as it is used in calculating the projected contact area. The value of the contact stiffness is usually determined from the initial unloading curve. Therefore, only one value of hardness is given for a single load cycle. However, the CSM option allows the continuous measurement of the contact stiffness during loading by superimposing a small oscillation on the primary loading signal and analyzing the resulting response of the system by means of a frequency-specific amplifier. With a continuous measure of the contact stiffness, the hardness can be obtained as a function of the indentation in a single loading-unloading loop, not just a single value. All the indentations were made into a depth of 300 nm at a constant strain rate of $0.05s^{-1}$. This group of experiments was designed in order to investigate the effect of the distance r on the indentation hardness. An image of these indentations was captured after all the indentations were made.

As shown in Figure 4.8, a straight line connecting the centers of the two marking indentations represents the grain boundary. The distance r can be measured from Figure 4.9. The indentations on the right side of the grain boundary shown in Figure 4.8 were used for the analysis in order to screen the effect of the grain structure.

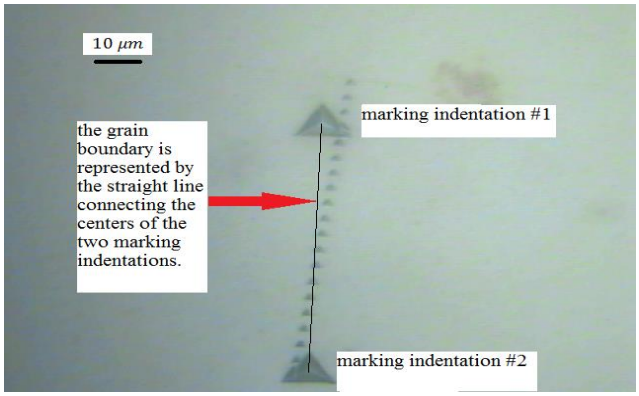

Figure 4.8 The identification of the grain boundary. The grain boundary is represented by the straight line connecting the two marking indentations.

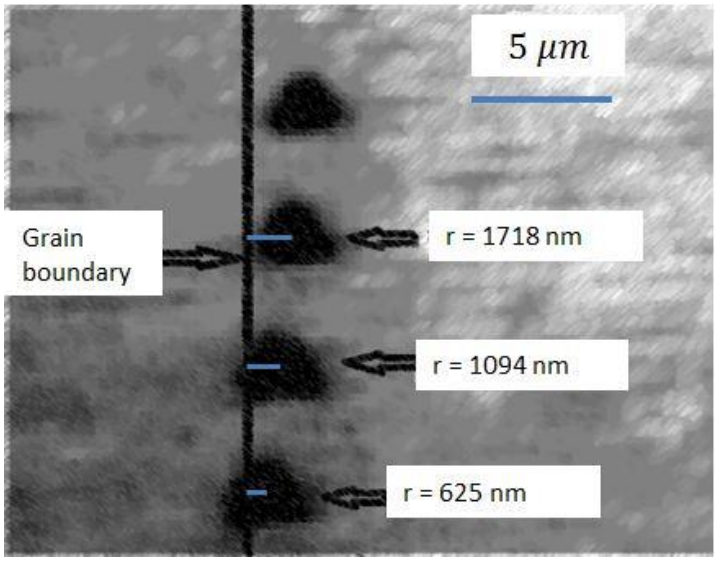

Figure 4.9 Distances between the indentations and the grain boundary. Three indentations with hardening-softening segments are marked and the corresponding distances to the grain boundary are given.

Three indentations in this group of experiments showed hardening-softening as shown in Figure 4.9. Others did not show such a phenomenon due to the large distances of those indentations from the grain boundary. Figure 4.10 shows clearly that as the distance r decreases, the hardness increases in the hardening-softening portion. The indentation right on the grain boundary is also presented in Figure 4.10 and it shows that no hardening-softening phenomenon is observed as there is no accumulation of dislocations since the dislocations are initiated and propagated from the grain boundary. When the distance r is smaller, the density of GNDs ρ_G is higher which causes the interactions between the dislocations and the grain boundary to become stronger. Therefore, there is an increase in the hardness in the hardening-softening portion of the hardness curve. The size effect of r is thus verified for the copper bicrystal. As the indentation depth keeps increasing, the hardness of the three indentations converges to the same value. This phenomenon can be predicted because after the hardening and softening, the effect of the grain boundary vanishes and the material hardness should approach the macrohardness. The three indentations were made at the same strain rate, so they must have the same value of the macrohardness. In order to prove that the increase in hardening is from the interaction between the dislocations and the grain boundary but not from the strain hardening due to the spherical tip in the Berkovich indenter, the elastic modulus as a function of the indentation depth is presented in Figure 4.11. It shows that when the indentation depth is greater than 20 nm, the elastic moduli for the three indentations with different values of r are close with each other around a constant value. This means that there is no strain hardening effect when the indentation depth is greater than 20 nm. Moreover, since the elastic modulus is not size-dependent, the three indentations should determine the same elastic modulus. It shows in Figure 4.10 that the hardening begins at

the depth of 50 nm, proving that the hardening is caused by the accumulation of dislocations near the grain boundary as no strain hardening is observed in the depth greater than 50 nm.

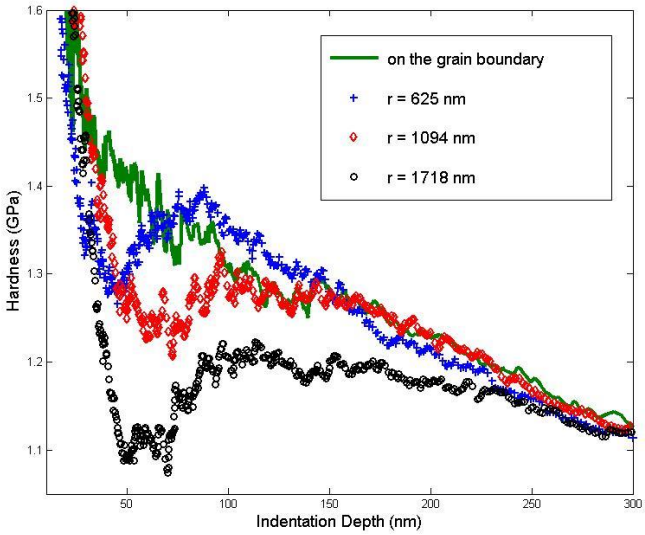

Figure 4.10 Hardness versus indentation depth curves from nanoindentation experiments for indentations with different values of r at the same strain rate of 0.05 s^{-1}. The solid (green) curve indicates the indentation made on the grain boundary. No hardening-softening is observed since the dislocations are initiated and propagated from the grain boundary without accumulation.

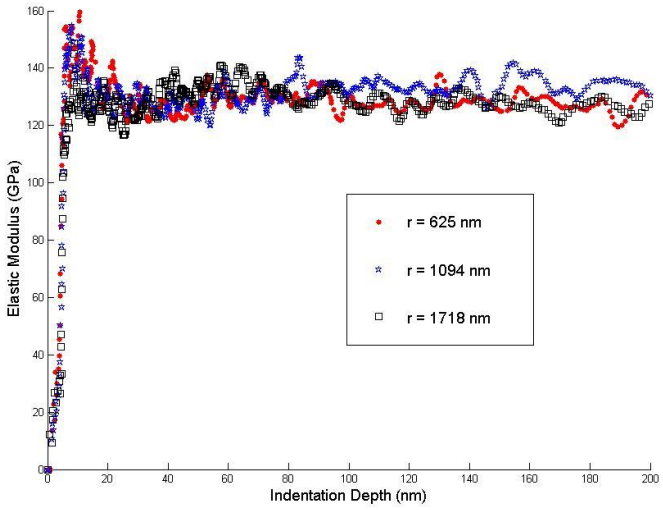

Figure 4.11 Elastic modulus as a function of the indentation depth for three indentations at different distances from the grain boundary. It shows that the moduli of the three indentations are close to each other when the indentation depth is greater than 20 nm.

4.5 Finite Element Simulation

In order to obtain the equivalent plastic strain as a function of the indentation depth, finite-element simulation is performed for the indentation problem using ABAQUS software. A cube with 50-μm sides is modeled to represent the tested sample. The Berkovich indenter is modeled on top of the cube as a blunt pyramid. The tip of the indenter is an equilateral triangle with 20-nm sides.

The ABAQUS interaction module is used to model the contact between the indenter and the sample. A special velocity is assigned to the indenter so that the indenter penetrates the sample to a depth of approximately 500 nm. After plastic deformation takes place, the indent can be observed at the sample surface as shown in Figure 4.12.

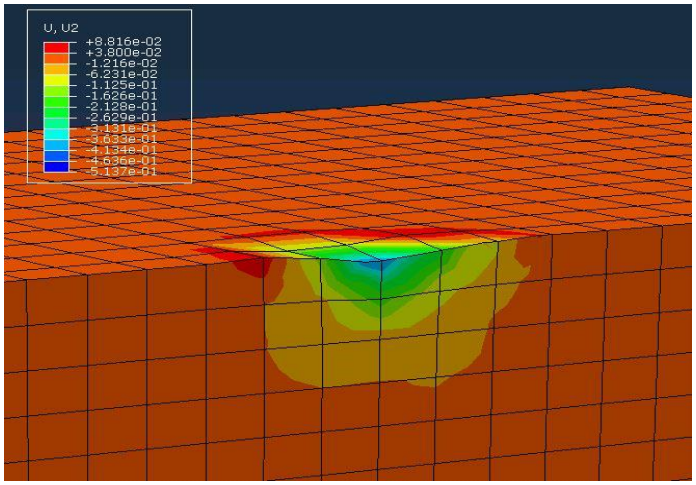

(a)

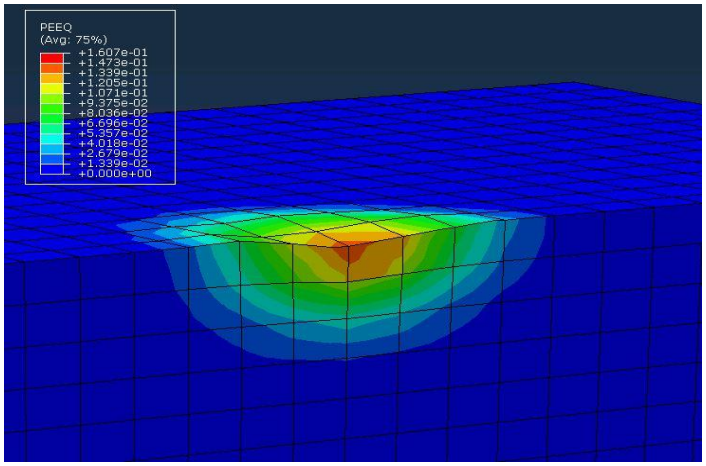

(b)

Figure 4.12 ABAQUS simulation results. (a) A contour plot of indentation depth, (b) A contour plot of the equivalent plastic strain.

4.6 Comparison between the Model and the Experiments

The hardness expressions from the TRISE model for bicrystals are compared with the hardness curves from the nanoindentation experiments for bicrystal aluminum as shown in Figure 4.13 and bicrystal copper as shown in Figure 4.14.

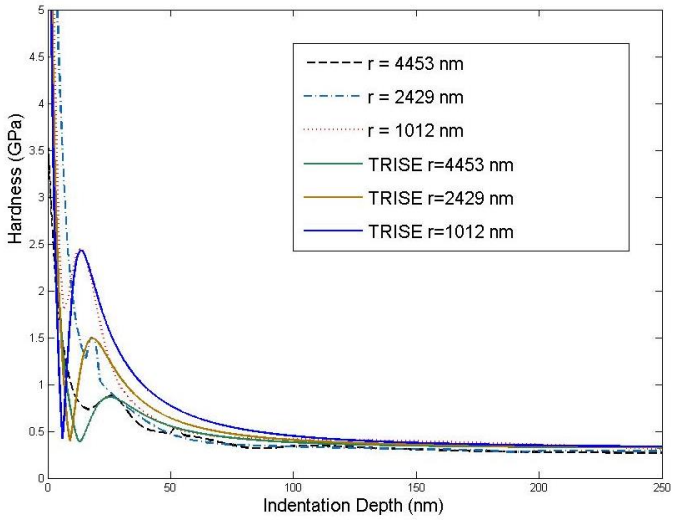

Figure 4.13. Comparison of TRISE model with experimental results for the three indentations with hardening-softening effect. The solid curves are obtained from TRISE model and the dashed curves are obtained from nano-indentation experiments.

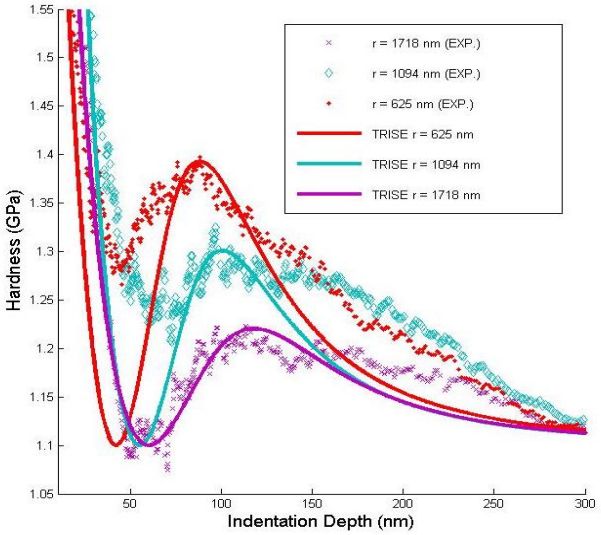

Figure 4.14 Comparison of hardness curves from TRISE model and nanoindentation experiments at various distances between the indenter and the grain boundary. Solid curves are predicted by the TRISE model.

The comparison shows that the TRISE model is firstly able to predict the indentation size effect as the hardness decreases with the increasing at small depths. The TRISE model is also able to predict the size effect related to the grain boundary, as for both specimens, the hardening becomes greater with the decreasing distance *r* between the indenter tip and the grain boundary. The models for bicrystal aluminum and copper show a good agreement with the experimental results. It also shows that the indentation depth in which the hardening starts becomes greater as the indentation moves away from the grain boundary. This is because when the distance *r* is greater, it requires greater indentation depth for the plastic zone to expand and reach the grain boundary.

The material parameters in the expressions of hardness and length scales are determined from curve fitting while comparing the model and the experiments. The length scale as a function of the equivalent plastic strain is determined for aluminum (Figure 4.15) and copper (Figure 4.16), respectively. The material parameters are presented in Table 4.1 for aluminum and for copper. It shows in both figures that the length scale decrease with the increasing equivalent plastic strain and approaches to zero when the strain is large. The indentation size effect is addressed by the length scales determined as there is higher strain gradient in small deformation, which requires a smaller length scale. It also follows the intrinsic property of the length scale that there is no gradient for large deformation and therefore the length scale is equal to zero. The length scale decreases as the distance *r* becomes smaller. The smaller length scale indicates a higher strain gradient, which leads to the increase in the material hardness.

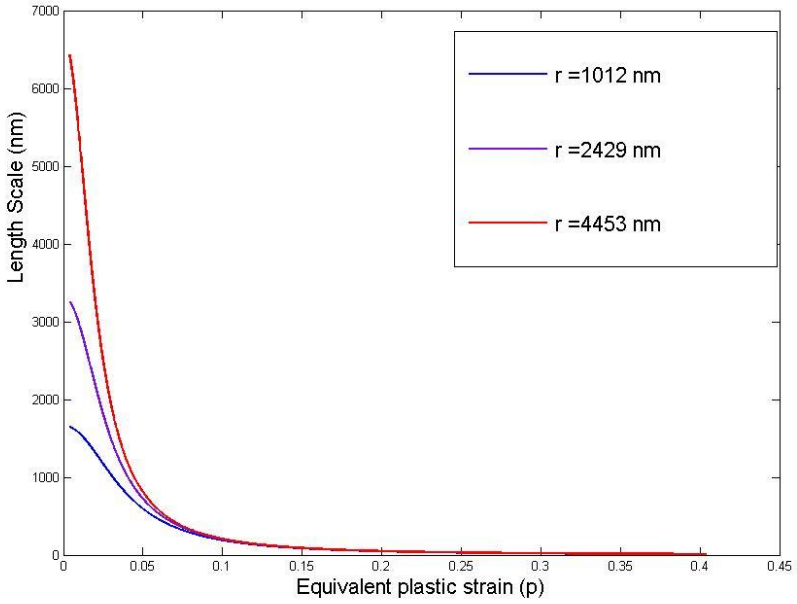

Figure 4.15 Material length scales versus equivalent plastic strain with different distances to the grain boundary for bicrystalline aluminum using the physically based model. Higher stain gradient can be observed for indentation closer to the grain boundary.

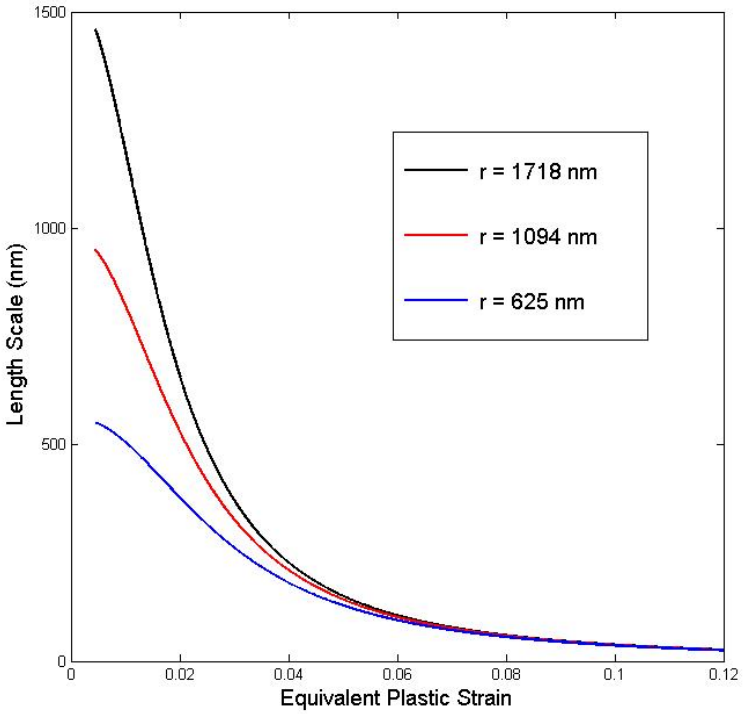

Figure 4.16 Material length scales versus equivalent plastic strain with different distances between the indenter and the grain boundary.

Table 4.1 Material parameters for bicrystal aluminum and copper.

Model Parameters	aluminum	copper
h_1 (nm)	10	42
δ_1	1.9	2.0
δ_2	135	3.0
δ_3	0.01	0.01
δ_4	1.61×10^{-6}	2.44×10^{-7}
δ_5	0.75	0.4

4.7 Rate Dependency of the Length Scale

The rate dependency of the length scale is investigated by incorporating a strain rate parameter in the expression in the length scale. As the hardness expression using the TRISE model is derived through the length scale, which means the hardness is rate dependent. Nanoindentation experiments are performed near the grain boundary of the copper bicrystal at different strain rates of $0.05\ s^{-1}$, $0.08\ s^{-1}$ and $0.10\ s^{-1}$ as shown in Figure 4.17. It shows from the experimental results that the hardness increases with the increasing strain rate.

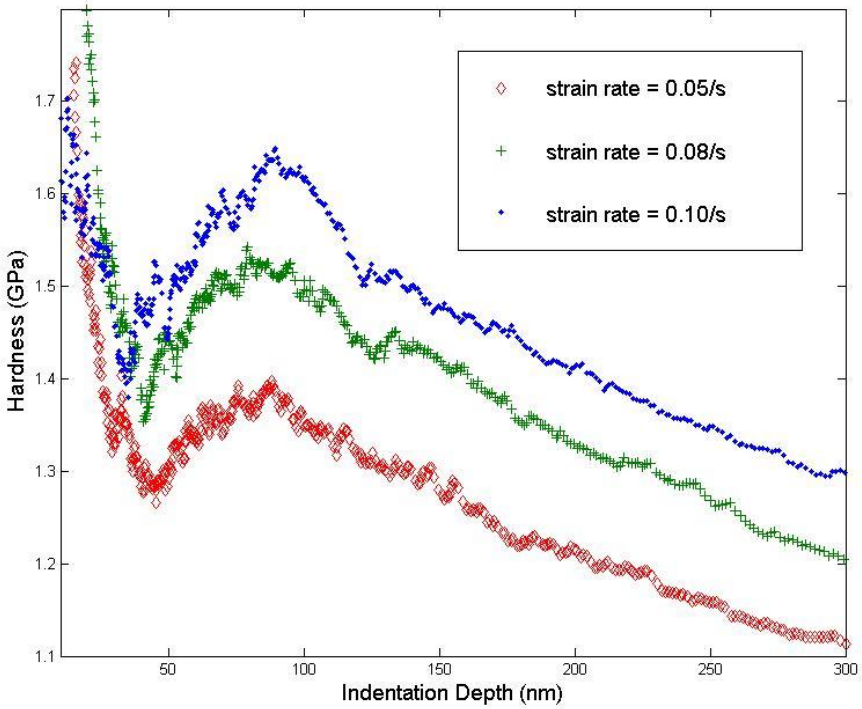

Figure 4.17 Hardness versus indentation depth curves from nanoindentation experiments for indentations with different strain rates but with the same r.

In order to determine the length scale, the equivalent plastic strain as a function of the indentation depth is required and it is usually determined using finite element simulation. The equivalent plastic strain during nanoindentation is also rate dependent. Therefore, there must be a rate dependent constitutive relation used during the simulation using ABAQUS. This is achieved by implementing a user material subroutine VUMAT during the simulation of indentation problems. After the simulation, the equivalent plastic strain is determined as a function of the indentation at different strain rates.

Comparing the hardness predicted by the TRISE model and the experimental results as shown in Figure 4.18, length scales for copper bicrystal at different strain rates are determined as shown in Figure 4.19. The comparison shows that the TRISE model predicts the rate dependency of hardness during nanoindentation very well. The hardness increases with higher value of the strain rate is used. The length scales show that the length scale decreases with the increasing, which causes the greater hardness at higher strain rates. It should be noted that the increase in hardness at different strain rates is due to the rate sensitivity. This sensitivity exists along the entire indentation depth. Therefore, as the strain rate increases, the hardness in the entire indentation depth increases. The amount of hardening is similar between the curves from different strain rates. This is because the distance between the indenter tip and the grain boundary is the same.

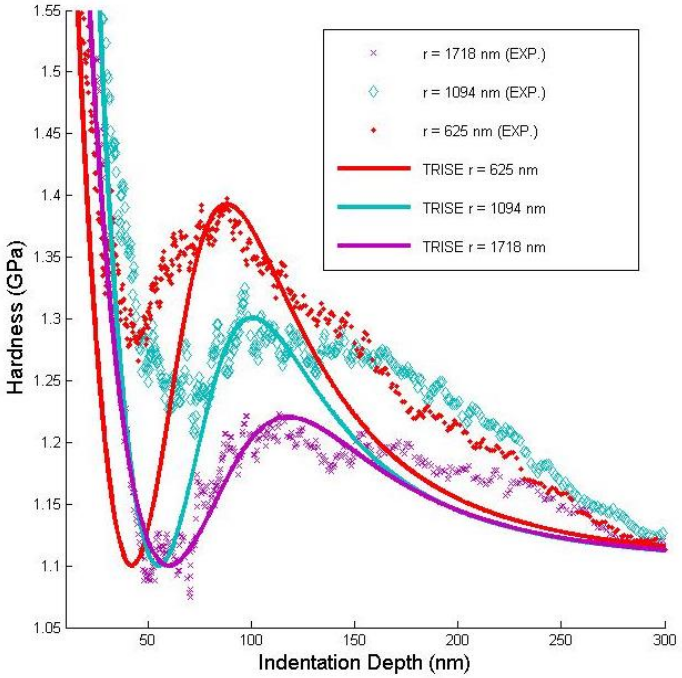

Figure 4.18 Comparison of hardness curves from TRISE model and nanoindentation experiments at various distances between the indenter and the grain boundary. Solid curves are predicted by the TRISE model.

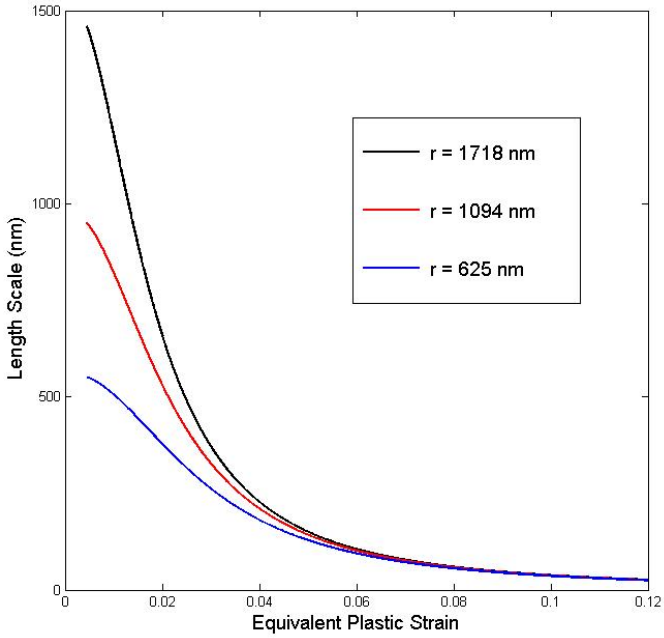

Figure 4.19 Material length scales versus equivalent plastic strain with different distances between the indenter and the grain boundary using Equation (21).

4.8 Conclusion

In this work, the contribution of the grain boundary to the hardening-softening phenomenon is investigated. The hardness increases with the decreasing grain size, which indicates that distance between the indenter and the grain boundary is an important factor related to the hardening-softening phenomenon. In order to isolate the grain boundary effect, bicrystal samples are used and nanoindentation experiments are performed near the grain boundary at different distances. The experimental results show that as the distance between the indenter tip and the grain boundary decreases, there is a higher hardening effect in the hardness curve from experiments.

In order to determine the length scale that is able to address the grain boundary effect, the TRISE model is modified for bicrystal samples. The distance r between the indenter tip and the grain boundary replaced the grain size factor because the grain size in bicrystals is in macroscopic scale. From the TRISE model and the experimental results, the length scale is determined in order to characterize both the indentation size effect and the grain boundary effect. The length scale becomes smaller when the distance r is smaller, indicating a higher strain gradient that leads to a greater hardness.

The rate dependency of bicrystals in nanoindentation is investigated. Nanoindentation experiments are performed at different strain rate with the same distance to the grain boundary. The equivalent plastic strain is determined using ABAQUS with VUMAT that provides the rate dependent constitutive relation. The TRISE model shows that the hardness increases with the increasing strain rates by giving different strain rate values into the hardness expression. Length scales at different strain rates are determined from the TRISE model and the experimental results. It shows that the length scale is rate dependent and it decreases with the increasing strain rate.

CHAPTER 5
NONLOCAL GRADIENT PLASTICITY THEORY

5.1 Introduction

It has been observed in the experiments of materials with microstructures that an initial evolution of defects is induced in the original material state in the form of localized zones during the process of cold-working, machining and forming, etc. The localized defects lead to a non-uniform material behavior. The defect may accumulate and interact with each other in the localized zones, which causes that the failure of materials is initiated in those localized zones due to further loadings.

As the localizations take place in small volumes in materials, the governing characteristic length scale of defects and their interactions is much lower than the local state variables used in the continuum theory. This leads to the loss of the statistical homogeneity in the representative volume element (RVE). Strong size effects are induced so that all the macroscopic functions used are sensitive to the properties within the RVE. The material behaviors are governed by mechanisms at different scales. The classical continuum theory does not contain the material intrinsic length scale, which leads to the numerical stability problems such as mesh size and mesh alignment sensitivities (Bammann et al., 1999; Glema, et al., 2000; Li et al., 2002; Voyiadjis et al. 2001; Voyiadjis and Abu Al-Rub, 2003; Voyiadjis and Abed, 2005; Voyiadjis and Dorgan, 2001). Nonlocal theory, which introduces the material intrinsic length scale in the constitutive equations, can be used in order to describe the long-range microstructural behaviors at a material point to be dependent not only on the state of the point itself but also the state of its neighboring space.

The integral models of nonlocal theory was reported by Kroner (1967) and Eringen and Edelen (1972) by incorporating the nonlocal terms through the integral equations of elasticity. The nonlocal anisotropic formulations based on the nonlocal tensorial variables were addressed by Bazant and Ozbolt (1990). A global averaging procedure is required in the integration using nonlocal models. However, this procedure cannot be easily linearized, which makes the integral models computationally inefficient.

Using Taylor series expansion, the integral models can be approximated to the gradient theories. Gradient theories include the higher-order gradients with coefficients that represent length scales associated with the nonlocal theories in the terms of the constitutive equations. Bammann and Aifantis (1982) and Aifantis (1984) incorporated a nonlocal terms through a gradient approach in order to describe the plastic deformation such as dislocation patterns and shear bands. Muhlhaus and Aifantis (1991) introduced the nonlocal behavior into the plasticity model through gradient terms in the yield function. Voyiadjis et al. (2001) and Voyiadjis and Dorgan (2001) proposed a multiscale model for plasticity and damage by incorporating the internal variables and the corresponding gradients in the potential functions as well as the yield and damage criteria. Dorgan and Voyiadjis (2003) proposed a formulation at the macroscale in

the plasticity potential function using nonlocal plasticity theory and gave the microstructural basis through the dislocation theory.

Size effects have shown their great importance in many engineering applications. Fleck et al. (1994) and Stolken and Evans (1998) reported the micro-torsion tests of thin wires and micro-bending tests of thin beams respectively and showed that the mechanical response increased with the decreasing diameter of the wire and the decreasing thickness of the beam. Size effect in nanoindentation experiments was reported by many researchers that the indentation hardness increased with the decreasing indentation depth or the decreasing indenter size (Stelmashenko et al., 1993; DeGuzman e al., 1993; Ma and Clarke, 1995; McElhaney et al., 1998; Swadener et al., 2002a, 2002b; Voyiadjis and Peters 2010). Huber et al. (2002) showed that the indentation of thin films showed an increase in the yield strength as the film thickness decreased. It has also been found that in nanoindentation experiments of polycrystalline materials, the hardness increased with the decreasing grain size (Yang and Vehoff, 2007) and that in nanoindentation experiments of bicrystalline materials near the grain boundary, the hardness increased as the distance between the indenter and the grain boundary decreased (Voyiadjis and Zhang, 2015; Zhang and Voyiadjis, 2016). These experiments presented the increase in strength with decreasing size in the micro and nano scales. Therefore, the mechanical responses are size dependent. In order to characterize this size dependency, a material length scale is required. The classical continuum plasticity theory (Hill, 1998) does not contain a length scale parameter and therefore, it is not able to predict the size effect encountered in experiments. Atomistic simulations, on the other hand, are not computational possible in predicting the size effect in the micro and mesoscale. Therefore, the classical theory needs to be enhanced with the gradient theory that incorporates the length scale parameter in the constitutive equations in order to bridge the gap between the macro-scale and the micro/nano-scale. In the last two decades, researchers have related the size dependency of mechanical properties to the strain gradients in a localized volume that leads to geometrically necessary dislocations (GNDs) (Fleck et al., 1994; Arsenlis and Parks, 1999; Busso et al., 2000; Nix and Gao, 1998; Abu Al-Rub and Voyiadjis, 2004; Voyiadjis and Abu Al-Rub, 2005; Voyiadjis et al., 2011; Voyiadjis and Zhang, 2015). Fleck and Hutchinson (1997) applied the phenomenological method to simplify the integral format of nonlocal theory through the couple stress theory. The plastic strain at a given point is dependent on its local counterpart and the strain gradient due to the non-uniform deformation in the small volume. The proposed relation verified the experimental observations by Fleck and Hutchinson (1993). Abu Al-Rub and Voyiadjis (2004) and Voyiadjis and Abu Al-Rub (2005) proposed a more general formulation of the coupling between the local plastic strain and the strain gradient.

In order to determine the length scale, the nonlocal model with length scale needs to be compared with the experimental results. Nanoindentation experiments have been found to be the most effective way to determine the length scale. In the macro-scale, the nonlocal theory provides the constitutive relation through the properties at a local point and the strain gradient together with a length scale parameter. In the micro-scale, Taylor hardening law was adapted and developed through the GNDs and statistically stored dislocations (SSDs) (Nix and Gao, 1998;

Gao and Huang, 2003; Abu Al-Rub and Voyiadjis 2004; Voyiadjis and Abu Al-Rub, 2005; Voyiadjis and Almasri, 2009). The hardness expression was given through Tabor's relation (Tabor, 1951) between hardness and flow stress (Voyiadjis and Peters, 2010). Therefore, with the length scale to be determined, the mechanical responses at different scales can be characterized. At the beginning, the length scales were determined as constant values in the scale of a few micrometers (Nix and Gao, 1998; McElhaney et al., 1998; Yuan and Chen, 2001). However, it has been shown that for different problems, it may require different values for the length scales (Begley and Hutchinson, 1998). Abu Al-Rub and Voyiadjis (2004) and Voyiadjis and Abu Al-Rub (2005) proposed an expression of length scale that is proportional with the mean free path of SSDs. As the mean free path of SSDs changes with the indentation procedure, the length scale is not a fixed value but a variable length scale.

In this chapter, the formulation of nonlocal gradient theory is given starting from the integral format in order to support the equations used in Chapters 3 and 4. The nonlocal theory is presented in both macro-scale and micro-scale. The gradient formulation is given through a thermodynamic consistent framework. Isotropic hardening and kinematic hardening are presented in the micro-scale basis. Shear band problem is taken as an example for the mesh refinement in finite element simulations.

5.2 Weak Form of the Nonlocal Formulation

The mechanical responses of a material at a given point depend not only on the local counterparts but also on the state in the neighboring space through a nonlocal gradient term. The classical continuum theory is thus enhanced with the gradient theory in order to characterize the long-range microstructural interactions. Taking plastic strain for an example, at a given material point *x*, the nonlocal measurement of plastic strain $\overline{p}$ is expressed through the weighted average of its local counterpart p over the surrounding volume V at a small distance $|d| \leq L_c$ from x as follows:

$$\overline{\boldsymbol{p}} = \frac{1}{V}\int_V \boldsymbol{w}(d)\boldsymbol{p}(x+d)\,dV \tag{5.1}$$

where L_c is an internal characteristic length; $\boldsymbol{w}(d)$ is a weight function that decays smoothly with distance d. $\boldsymbol{w}(d)$ is given by

$$\boldsymbol{w}(d) = \boldsymbol{I}w(d) \tag{5.2}$$

where $\boldsymbol{I}$ is an identity tensor that may be replaced by another tensor in order to induce anisotropic behaviors of materials.

The local tensor $\boldsymbol{p}$ in Equation (5.1) can be approximated using a Taylor series expansion at *d=0* (Muhlhaus and Aifantis, 1991; Vardoulakis and Aifantis, 1991) such that

$$\boldsymbol{p}(x+d) = \boldsymbol{p}(x) + \nabla \boldsymbol{p}(x)d + \frac{1}{2!}\nabla^2 \boldsymbol{p}(x)d^2 + \frac{1}{3!}\nabla^3 \boldsymbol{p}(x)d^3 + \cdots \tag{5.3}$$

where ∇^i denotes the *i*th order of the gradient operator. If only isotropic behavior is considered, the integrals of the odd terms in Equation (5.3) vanish. By truncating the Taylor series after the quadratic term, and combining Equations (5.1) and (5.3) yields

$$\overline{\boldsymbol{p}} = \frac{1}{V}\int_V w(d)\boldsymbol{p}(x)\, dV + \frac{1}{2!\,V}\int_V w(d)\nabla^2 \boldsymbol{p}(x)d^2\, dV \tag{5.4}$$

Equation (5.4) can be rewritten as a partial differential equation as follows

$$\overline{\boldsymbol{p}} = \boldsymbol{p} + \left(\frac{1}{2!\,V}\int_V w(d)d^2\, dV\right)\nabla^2 \boldsymbol{p} \tag{5.5}$$

with

$$\frac{1}{V}\int_V w(d)\, dV = 1 \tag{5.6}$$

Therefore, Equation (5.5) can be simplified as follows

$$\overline{\boldsymbol{p}} = \boldsymbol{p} + l^2\nabla^2 \boldsymbol{p} \tag{5.6}$$

In Equation (5.6), the gradient term $l^2\nabla^2\boldsymbol{p}$ is taken as an approximation of the nonlocal strain gradient in the neighboring space of the material point at *x*. *l* is the length scale that weighs the gradient term.

Fleck and Hutchinson (1993) developed a phenomenological theory of strain gradient plasticity based on gradients of rotation, which fits with the framework of the couple stress theory. By assuming that the strain energy density is only dependent on second von Mises invariant of strain, Fleck and Hutchinson (1997) further simplified the expression based on that the strain energy density depends only on the overall effective strain as follows:

$$\overline{p} = \sqrt{p^2 + l^2\eta^2} \tag{5.7}$$

where $\overline{p}$ is the total plastic strain; p is the local counterpart of the plastic strain; η is the strain gradient due to the non-uniform deformation in a small volume; l is the length scale that characterizes the influence of the strain gradient.

Abu Al-Rub and Voyiadjis (2004) and Voyiadjis and Abu Al-Rub (2005) developed a more general expression of Equation (5.7) such that

$$\overline{p} = [p^\gamma + (l\eta)^\gamma]^{1/\gamma} \tag{5.8}$$

where γ is the fitting parameter. Therefore, Equation (5.7) that was proposed by Fleck and Hutchinson (1997) assumes $\gamma = 2$. The gradient term is expressed as follows

$$l\eta = c_1\eta_{iik}\eta_{jjk} + c_2\eta_{ijk}\eta_{ijk} + c_3\eta_{ijk}\eta_{kji} \tag{5.9}$$

where c_1, c_2 and c_3 are material coefficients of length square dimension.

Aifantis and his co-workers (Aifantis, 1984, 1987; Zbib and Aifantis, 1988; Muhlhaus and Aifantis, 1991) proposed the coupling between the local strain and the strain gradient as $\gamma = 1$. The gradient term is expressed as follows

$$l\eta = l\|\nabla p\| = l\sqrt{\nabla p \cdot \nabla p} \tag{5.10}$$

de Borst and his co-workers (de Borst and Muhlhaus, 1992; de Borst et al., 1993; de Borst and Pamin, 1996) proposed the gradient term as follows

$$l\eta = a^2\nabla^2 p \tag{5.11}$$

with $l = \sqrt{a}$.

Gao and co-workers proposed the mechanism based strain gradient theory and the Taylor based nonlocal theory of plasticity (Nix and Gao, 1998; Gao et al., 1999a, 1999b; Huang et al., 2000; Gao and Huang, 2001, 2003). They gave different values of γ such that

$$\overline{p} = \sqrt{p^2 + l\eta} \tag{5.12}$$

This type of equation has been applied by many authors to solve the size effect problems at small scales such as micro-bending, micro-torsion, particle reinforced composites, micro-electro-mechanical systems (MEMS), indentations, crack tips and void growth (Begley and Hutchinson, 1998; Stolken and Evans, 1998; Saha et al., 2001; Gao et al., 1999, 2000; Guo et al., 2001; Xue et al., 2002a, 2002b, 2002c; Wang et al., 2003).

5.3 Thermodynamically Consistent Gradient Formulation

In order to describe the isotropic hardening and kinematic hardening, the thermodynamic framework uses the Helmholtz free energy that depends on the internal state variables such that:

$$\Psi = \Psi\left(\varepsilon_{ij}^e, T, k_{ij}, \nabla^2 k_{ij}, p, \nabla^2 p\right) \tag{5.13}$$

where ε_{ij}^e is the elastic strain; T is the temperature in Kelvin; k_{ij} and p are the local measure of the kinematic and isotropic hardening; $\nabla^2 k_{ij}$ and $\nabla^2 p$ are the gradients of kinematic and

isotropic hardening, respectively. It needs to be mentioned that the nonlocal expressions of isotropic and kinematic hardening are given as follows (Dorgan and Voyiadjis, 2003)

$$\overline{p} = p + A\nabla^2 p \tag{5.14}$$

$$\overline{k}_{ij} = k_{ij}^2 + B\nabla^2 k_{ij} \tag{5.15}$$

The internal variables for kinematic hardening and isotropic hardening are assumed to be independent of each other in order to identify the two properties separately. It is quite common to treat quantities to be independent even though they are related (Dorgan and Voyiadjis, 2003).

Based on the above assumption, Equation (5.13) can be rewritten as the quadratic form in terms of its internal state variables as follows

$$\begin{aligned}\rho\Psi = \frac{1}{2}\left(\varepsilon_{ij} - \varepsilon_{ij}^p\right)\boldsymbol{E}_{ijkl}\left(\varepsilon_{kl} - \varepsilon_{kl}^p\right) + \frac{1}{2}a_1 p^2 + \frac{1}{2}a_2(\nabla^2 p)^2 + \frac{1}{2}b_1 k_{ij}k_{ij} \\ + \frac{1}{2}b_2\nabla^2 k_{ij}\nabla^2 k_{ij}\end{aligned} \tag{5.16}$$

where the matrix $\boldsymbol{E}_{ijkl}$ is the fourth order elastic stiffness tensor; ε_{ij} is the total strain; ε_{ij}^p is the plastic strain; a_1, a_2, b_1 and b_2 are coefficients that are dependent on material and geometrical properties. By taking the time derivative of Equation (5.13), one can obtain the following expression

$$\dot{\Psi} = \frac{\partial\Psi}{\partial\varepsilon_{ij}^e}\dot{\varepsilon}_{ij}^e + \frac{\partial\Psi}{\partial T}\dot{T} + \frac{\partial\Psi}{\partial k_{ij}}\dot{k}_{ij} + \frac{\partial\Psi}{\partial\nabla^2 k_{ij}}\nabla^2\dot{k}_{ij} + \frac{\partial\Psi}{\partial p}\dot{p} + \frac{\partial\Psi}{\partial\nabla^2 p}\nabla^2\dot{p} \tag{5.17}$$

Substitution of Equation (5.17) into the Clausus-Duhem inequality gives the following equation

$$\begin{aligned}\left(\sigma_{ij} - \rho\frac{\partial\Psi}{\partial\varepsilon_{ij}^e}\right)\dot{\varepsilon}_{ij}^e - \rho\left(\frac{\partial\Psi}{\partial T} + s\right)\dot{T} + \sigma_{ij}\dot{\varepsilon}_{ij}^p - \frac{q}{T}\cdot\nabla T - \rho\frac{\partial\Psi}{\partial\nabla^2 k_{ij}}\nabla^2\dot{k}_{ij} - \rho\frac{\partial\Psi}{\partial k_{ij}}\dot{k}_{ij} \\ - \rho\frac{\partial\Psi}{\partial p}\dot{p} - \frac{\partial\Psi}{\partial\nabla^2 p}\nabla^2\dot{p} \geq 0\end{aligned} \tag{5.18}$$

From Equation (5.18) the thermodynamic state laws can be determined as follows:

$$\sigma_{ij} = \rho\frac{\partial\Psi}{\partial\varepsilon_{ij}^e} \tag{5.19}$$

$$s = -\frac{\partial\Psi}{\partial T} \tag{5.20}$$

$$C = \rho\frac{\partial\Psi}{\partial p} \tag{5.21}$$

$$\nabla^2 C = \frac{\partial\Psi}{\partial\nabla^2 p} \tag{5.22}$$

$$D_{ij} = \rho \frac{\partial \Psi}{\partial k_{ij}} \tag{5.23}$$

$$\nabla^2 D_{ij} = \rho \frac{\partial \Psi}{\partial \nabla^2 k_{ij}} \tag{5.24}$$

where C and D_{ij} are defined as the thermodynamic conjugate terms corresponding to the nonlocal internal state variables. Compare Equations (5.21) through (5.24) with Equation (5.16), one can derive the local conjugate terms as follows

$$C = a_1 p \tag{5.25}$$

$$\nabla^2 C = a_2 \nabla^2 p \tag{5.26}$$

$$D_{ij} = b_1 k_{ij} \tag{5.27}$$

$$\nabla^2 D_{ij} = b_2 \nabla^2 k_{ij} \tag{5.28}$$

By assuming $a_1 = a_2 = a$ and $b_1 = b_2 = b$, the conjugate terms can be written as follows

$$C = ap \tag{5.29}$$

$$\nabla^2 C = a \nabla^2 p \tag{5.30}$$

$$D_{ij} = b k_{ij} \tag{5.31}$$

$$\nabla^2 D_{ij} = b \nabla^2 k_{ij} \tag{5.32}$$

Therefore, the nonlocal measure of the conjugate terms can be written as the same format shown in Equations (5.14) and (5.15) as follows

$$\overline{C} = a\overline{p} = C + A\nabla^2 p \tag{5.33}$$

$$\overline{D}_{ij} = b\overline{k}_{ij} = D_{ij} + B\nabla^2 k_{ij} \tag{5.34}$$

The value of the thermodynamic conjugate forces can be obtained through the evolution relations of the internal state variables, which are obtained by assuming the physical existence of the dissipation potential at the macro-scale (Dorgan and Voyiadjis, 2003). The dissipation processes are given from the thermodynamic conjugate forces and the respective flux variables as follows

$$\Pi = \sigma_{ij} \dot{\varepsilon}_{ij}^p - C\dot{p} - \nabla^2 C \nabla^2 \dot{p} - D_{ij} \dot{k}_{ij} - \nabla^2 D_{ij} \nabla^2 \dot{k}_{ij} \tag{5.35}$$

The evolution equations of the macro-scale internal state variables can be obtained through the generalized normality rule of thermodynamics. In this regard, the macro-scale dissipation potential is defined in terms of the gradient dependent internal state variables as a continuous and convex scalar valued function of the flux variables (Voyiadjis and Deliktas, 2000, 2001) as follows

$$\Theta = \Theta\left(\dot{\varepsilon}_{ij}^{p}, T, \dot{p}, \nabla^2\dot{p}, \dot{k}_{ij}, \nabla^2\dot{k}_{ij}\right) \tag{5.36}$$

By using the Legendre-Fenchel transformation of the dissipation potential, one can obtain complementary laws in the form of the evolution laws of flux variables as function of the dual variables as follows

$$\Theta' = \Theta'\left(\sigma_{ij}, C, \nabla^2 C, D_{ij}, \nabla^2 D_{ij}\right) = F\left(\sigma_{ij}, C, \nabla^2 C, D_{ij}, \nabla^2 D_{ij}\right) \tag{5.37}$$

The objective function is constructed using the Lagrange multiplier in the following form:

$$\Omega = \Pi - \dot{\lambda}F \tag{5.38}$$

In order to obtain the plastic strain rate, the objective function is extremized by taking derivative over σ_{ij} as follows:

$$\frac{\partial \Omega}{\partial \sigma_{ij}} = 0 \tag{5.39}$$

The evolution equation of the plastic strain can be obtained as follows:

$$\dot{\varepsilon}_{ij}^{p} = \dot{\lambda}\frac{\partial F}{\partial \sigma_{ij}} \tag{5.40}$$

The plastic potential function F is defined as follows

$$\begin{aligned} F = f + \frac{w_1}{2}\overline{C}^2 + \frac{w_2}{2}\overline{D}_{ij}\overline{D}_{ij} = f + \frac{w_1}{2}\left[C^2 + 2AC\nabla^2 C + A^2(\nabla^2 C)^2\right] \\ + \frac{w_2}{2}\left(D_{ij}D_{ij} + 2BD_{ij}\nabla^2 D_{ij} + B^2\nabla^2 D_{ij}\nabla^2 D_{ij}\right) \end{aligned} \tag{5.41}$$

where w_1 and w_2 are constants that adjust the units of the equation; f is a yield function of von Mises type and is defined as follows

$$f = \left\{\frac{3}{2}\left(s_{ij} - D_{ij}\right)\left(s_{ij} - D_{ij}\right)\right\}^{1/2} - \sigma_{yp} - C \equiv 0 \tag{5.42}$$

where s_{ij} is the deviatoric component of the stress tensor which can be given as follows

$$s_{ij} = \sigma_{ij} - \frac{1}{3}\sigma_{mm}\delta_{ij} \tag{5.43}$$

The gradient dependent evolution equation of the isotropic hardening flux variable can be obtained using the generalized normality rule of thermodynamics:

$$\dot{p} = -\dot{\lambda}\frac{\partial F}{\partial C} = -\dot{\lambda}\left(w_1\overline{C} - 1\right) \tag{5.44}$$

$$\nabla^2\dot{p} = -\dot{\lambda}\frac{\partial F}{\partial \nabla^2 C} = -\dot{\lambda}w_1 A\overline{C} \tag{5.45}$$

The evolution of the conjugate forces and the gradient can be obtained by taking time derivative of Equations (5.29) and (5.30) such that:

$$\dot{C} = a\dot{p} = a\dot{\lambda}\left(1 - w_1\overline{C}\right) \tag{5.46}$$

$$\nabla^2\dot{C} = a\nabla^2\dot{p} = -aw_1 A\dot{\lambda}\overline{C} \tag{5.47}$$

For kinematic hardening, the gradient dependent evolution equation are obtained through the generalized normality rule as well as for the isotropic hardening as follows

$$\dot{k}_{ij} = -\dot{\lambda}\frac{\partial F}{\partial D_{ij}} = -\dot{\lambda}\left(\frac{\partial f}{\partial D_{ij}} + w_2\overline{D}_{ij}\right) \tag{5.48}$$

$$\nabla^2\dot{k}_{ij} = -\dot{\lambda}\frac{\partial F}{\partial \nabla^2 D_{ij}} = -\dot{\lambda}w_2 B\overline{D}_{ij} \tag{5.49}$$

It can be derived from Equations (5.41) and (5.42) that

$$-\frac{\partial f}{\partial D_{ij}} = \frac{\partial f}{\partial s_{ij}} = \frac{\partial f}{\partial \sigma_{ij}} = \frac{\partial F}{\partial \sigma_{ij}} \tag{5.50}$$

Using Equations (5.46) and (5.48), the Frederick-Armstrong equation can be modified so that the evolution of the kinematic hardening component shows a nonlocal behavior through the gradient term as follows

$$\dot{k}_{ij} = \dot{\varepsilon}^p_{ij} - \dot{\lambda}w_2 D_{ij} - \dot{\lambda}w_2 B\nabla^2 D_{ij} \tag{5.51}$$

The evolution of the thermodynamic conjugate forces and gradient can be obtained by taking time derivative of Equations (5.31) and (5.32) such that

$$\dot{D}_{ij} = b\dot{k}_{ij} = b(\dot{\varepsilon}^p_{ij} - \dot{\lambda}w_2\overline{D}_{ij}) \tag{5.52}$$

$$\nabla^2\dot{D}_{ij} = b\nabla^2\dot{k}_{ij} = -bw_2 B\dot{\lambda}\overline{D}_{ij} \tag{5.53}$$

The Lagrange multiplier can be determined through the consistency condition for plasticity ($\dot{f} \equiv 0$) as follows

$$\dot{f} \equiv \frac{\partial f}{\partial \sigma_{ij}} : \dot{\sigma}_{ij} + \frac{\partial f}{\partial C} : \dot{C} + \frac{\partial f}{\partial D_{ij}} : D_{ij} = 0 \tag{5.54}$$

From the assumption of associative plasticity and additive decomposition of the elastic strain, Equation (5.54) can be rewritten as follows

$$\dot{f} = \frac{\partial f}{\partial \sigma_{ij}} \left[E_{ijkl} \left(\dot{\varepsilon}_{kl} - \dot{\lambda} \frac{\partial f}{\partial \sigma_{kl}} \right) - b\dot{\lambda} \frac{\partial f}{\partial \sigma_{ij}} + bw_2 \dot{\lambda} \overline{D}_{ij} \right] - a\dot{\lambda}\left(1 - w_1 \overline{C}\right) = 0 \tag{5.55}$$

The Lagrange multiplier can then be solved as follows

$$\dot{\lambda} = \frac{1}{h} \frac{\partial f}{\partial \sigma_{ij}} E_{ijkl} \dot{\varepsilon}_{kl} \tag{5.56}$$

where *h* is the hardening modulus and is defined as follows

$$h = \frac{\partial f}{\partial \sigma_{ij}} E_{ijkl} \frac{\partial f}{\partial \sigma_{kl}} + a\left(1 - w_1 \overline{C}\right) + \left(\frac{\partial f}{\partial \sigma_{ij}} \right) \left(\frac{\partial f}{\partial \sigma_{ij}} \right) b - bw_2 \frac{\partial f}{\partial \sigma_{ij}} \overline{D}_{ij} \tag{5.57}$$

The constitutive equation of this model is defined through the Hookean stress-strain relation as follows

$$\dot{\sigma}_{ij} = E_{ijkl} \dot{\varepsilon}^e_{kl} = E_{ijkl} \left(\dot{\varepsilon}_{kl} - \dot{\lambda} \frac{\partial f}{\partial \sigma_{kl}} \right) \tag{5.58}$$

Plugging the multiplier determined in Equation (5.56) into Equation (5.58) yields the constitutive law as follows:

$$\dot{\sigma}_{ij} = G_{ijkl} \dot{\varepsilon}^e_{kl} \tag{5.59}$$

where the modulus G_{ijkl} is defined as follows

$$D_{ijkl} = E_{ijkl} - \frac{1}{h} E_{ijmn} \frac{\partial f}{\partial \sigma_{mn}} \frac{\partial f}{\partial \sigma_{pq}} E_{pqkl} \tag{5.60}$$

5.4 Nonlocal Theory in the Microstructural Basis

Dislocation theory is widely used in order to provide a micro-mechanical justification for the thermodynamic consistent model. Dislocation density has been used in order to bridge the

macro- and micro-scale (Bammann and Aifantis, 1982; Fleck and Hutchinson, 1993; Menzel and Steinmann, 2000; Voyiadjis and Abu Al-Rub, 2005).

The shear plastic strain is dependent on the mobile dislocation density and can be defined as follows (Conrad et al., 1985)

$$\gamma^p = \rho^m b l \tag{5.61}$$

where b is the magnitude of the Burgers vector; l is the internal length scale parameter which is assumed to be the free path of trapped dislocations. The plastic strain in the macro-scale can be derived using Schmid orientation tensor as follows

$$\varepsilon_{ij}^p = \gamma^p M_{ij} \tag{5.62}$$

where M_{ij} is the symmetric Schmid orientation tensor.

The evolution of the plastic strain can then be found by taking the time derivative of Equation (5.62) and by plugging in Equation (5.61) as follows

$$\dot{\varepsilon}_{ij}^p = M_{ij}\left(\dot{\rho}^m b l + \rho^m b \dot{l}\right) \tag{5.63}$$

where $\dot{l}$ is the average dislocation glide velocity.

Walgraef and Aifantis (1985, 1988) proposed the reaction-diffusion equations in order to express the evolution of the immobile and mobile dislocations as follows

$$\dot{\rho}^i = J^i \nabla^2 \rho^i + g\left(\rho^i\right) - f\left(\rho^i, \rho^m\right) \tag{5.64}$$

$$\dot{\rho}^m = J^m \nabla^2 \rho^m + f\left(\rho^i, \rho^m\right) \tag{5.65}$$

where J^i and J^m are diffusion-like coefficients for the immobile and mobile dislocations and can be approximated as follows (Aifantis, 1987; Walgraef and Aifantis, 1988; Aifantis, 1999a, 1999b):

$$J^i \approx \frac{\rho^m \dot{l} y_d^3}{4} \tag{5.66}$$

$$J^m \approx \frac{\dot{l}^2}{2\xi {\rho_0^i}^2} \tag{5.67}$$

where ξ is the pinning rate of mobile dislocations by immobile diploes; ρ_0^i is a reference homogeneous solution of the immobile dislocation density; y_d is the mean height of immobile diploles; $g\left(\dot{\rho}^i\right)$ is the production/annihilation of immobile dislocations which can be expressed as follows

$$g(\rho^i) = \alpha(\rho_0^i - \rho^i) \tag{5.68}$$

$f(\rho^i, \rho^m)$ indicates the interaction between immobile and mobile dislocations that can be defined as follows

$$f(\rho^i, \rho^m) = \beta\rho^i - \xi\rho^m{\rho^i}^2 \tag{5.69}$$

where β is the freeing rate of immobile dislocations for increasing stress.

Therefore, the evolution for the immobile and mobile dislocations are defined as follows

$$\dot{\rho}^i = \frac{\rho^m \dot{l} y_d^3}{4}\nabla^2\rho^i + \alpha(\rho_0^i - \rho^i) - \left(\beta\rho^i - \xi\rho^m{\rho^i}^2\right) \tag{5.70}$$

$$\dot{\rho}^m = \frac{\dot{l}^2}{2\xi{\rho_0^i}^2}\nabla^2\rho^m + \left(\beta\rho^i - \xi\rho^m{\rho^i}^2\right) \tag{5.71}$$

The evolution of the scalar isotropic hardening variable is normally expressed in terms of the second order plastic strain rate tensor. Therefore, the evolution of the isotropic hardening is defined through the equivalent plastic strain rate as follows

$$\dot{p} = \dot{\varepsilon}_{eq}^p = \sqrt{\frac{2}{3}\dot{\varepsilon}_{ij}^p\dot{\varepsilon}_{ij}^p} \tag{5.72}$$

Using Equation (5.63) and (5.65), the isotropic hardening in the macro-scale can be expressed in terms of dislocation densities as follows

$$\dot{p} = \dot{\varepsilon}_{eq}^p = \left[b\dot{l}\left(\rho^m + \frac{l}{\dot{l}}J^m\nabla^2\rho^m\right) + blf(\rho^i, \rho^m)\right]\sqrt{\frac{2}{3}M_{ij}M_{ij}} \tag{5.73}$$

Comparing Equation (5.73) with the evolution of the isotropic hardening defined in Equation (5.44), the following relations can be derived as

$$\dot{\lambda} = blf(\rho^i, \rho^m)\sqrt{\frac{2}{3}M_{ij}M_{ij}} - \dot{\lambda}w_1 a(p + A\nabla^2 p) = b\dot{l}\left(\rho^m + \frac{l}{\dot{l}}J^m\nabla^2\rho^m\right)\sqrt{\frac{2}{3}M_{ij}M_{ij}} \tag{5.74}$$

From the above equation, the coefficients in the gradient theory can be defined on a microstructural basis as follows

$$w_1 = l^{-1} \tag{5.75}$$

$$a = \frac{-\dot{l}}{f(\rho^i, \rho^m)} \tag{5.76}$$

$$A = \frac{l}{\dot{l}} J^m \tag{5.77}$$

The kinematic hardening variable is the cumulative effect from the flux related backstresses. Bammann and Aifantis (1982) defined the backstress through immobile and mobile dislocation density as follows

$$D_{ij}^i = -\pi^i \rho^i M_{ij} \tag{5.78}$$

$$D_{ij}^m = -\pi^m \rho^m M_{ij} \tag{5.79}$$

where π^i and π^m are constants and M_{ij} is the symmetric macroscopic Schmid orientation tensor. The total backstress is obtained as the sum of the components from the immobile dislocations and the mobile dislocations such that

$$D_{ij} = D_{ij}^i + D_{ij}^m = -\left(\pi^i \rho^i + \pi^m \rho^m\right) M_{ij} \tag{5.80}$$

Assuming that the slip system remains unchanged along with time, the evolution of the backstress can be obtained by taking time derivative of Equation (5.80) as follows

$$\dot{D}_{ij} = -\left(\pi^i \dot{\rho}^i + \pi^m \dot{\rho}^m\right) M_{ij} \tag{5.81}$$

The evolution of the backstress can be obtained from Equations (5.64) and (5.65) in terms of the dislocation densities and the dislocation density gradients as follows

$$\dot{D}_{ij} = -\left[\pi^i J^i \nabla^2 \rho^i + \pi^i g\left(\rho^i\right) + \left(\pi^m - \pi^i\right) f\left(\rho^i, \rho^m\right) + \pi^m J^m \nabla^2 \rho^m\right] M_{ij} \tag{5.82}$$

In order to relate the above equation with Equation (5.52), the Laplacian of the kinematic hardening is defined through the use of Equation (5.80) as follows by assuming that the Laplacian of the constants π^i and π^m are zero and that $\nabla^2 M_{ij}$ can be neglected

$$\nabla^2 D_{ij} = -\left(\pi^i \nabla^2 \rho^i + \pi^m \nabla^2 \rho^m\right) M_{ij} \tag{5.83}$$

Substituting Equations (5.80) and (5.83) into Equation (5.34) gives the nonlocal form of the backstress in terms of dislocation densities and the Laplacian of dislocation densities as follows

$$\overline{D}_{ij} = -\left(\pi^i \rho^i + \pi^i B \nabla^2 \rho^i + \pi^m \rho^m + \pi^m B \nabla^2 \rho^m\right) M_{ij} \tag{5.84}$$

It can be seen from Equation (5.84) that the nonlocal kinematic hardening backstress can be decomposed into the components due to immobile and mobile dislocations.

Using Equations (5.52), (5.63), (5.74) and (5.84), the following relation can be determined as

$$\dot{D}_{ij} = abM_{ij}\left\{w_2 lf(\rho^i,\rho^m)\sqrt{\frac{2}{3}M_{pq}M_{pq}}\left[\pi^i(\rho^i + B\nabla^2\rho^i) + \pi^m(\rho^m + B\nabla^2\rho^m)\right] + \dot{\rho}^m l + \rho^m \dot{l}\right\} \tag{5.85}$$

Substituting Equations (5.64) and (5.65) into Equation (5.85) gives the following equation as

$$\begin{aligned}\dot{D}_{ij} = {} & ablf(\rho^i,\rho^m)M_{ij} + ablw_2\rho^i f(\rho^i,\rho^m)\pi^m M_{ij}\sqrt{\frac{2}{3}M_{pq}M_{pq}} \\ & + b\rho^m\left[a\dot{l} + w_2 alf(\rho^i,\rho^m)\pi^m\sqrt{\frac{2}{3}M_{pq}M_{pq}}\right]M_{ij} \\ & + b\nabla^2\rho^i\left[Balw_2\pi^i f(\rho^i,\rho^m)\sqrt{\frac{2}{3}M_{pq}M_{pq}}\right]M_{ij} \\ & + \mathrm{b}\nabla^2\rho^m\left[J^m al + w_2 alf(\rho^i,\rho^m)B\pi^m\sqrt{\frac{2}{3}M_{pq}M_{pq}}\right]M_{ij}\end{aligned} \tag{5.86}$$

Comparing Equation (5.82) with Equation (5.86) gives the following relations as

$$-\pi^i J^i = abw_2 lf(\rho^i,\rho^m)B\pi^i\sqrt{\frac{2}{3}M_{pq}M_{pq}} \tag{5.87}$$

$$-\pi^m J^m = ablJ^m + ablw_2 f(\rho^i,\rho^m)B\pi^m aw_2 lf(\rho^i,\rho^m)A\pi^i\sqrt{\frac{2}{3}M_{pq}M_{pq}} \tag{5.88}$$

$$\begin{aligned}(\pi^m - \pi^i)f(\rho^i,\rho^m) - \pi^i g(\rho^i) = {} & b\left\{\rho^i\left[alw_2 f(\rho^i,\rho^m)\pi^m aw_2 lf(\rho^i,\rho^m)A\pi^i\sqrt{\frac{2}{3}M_{pq}M_{pq}}\right]\right. \\ & \left. + alf(\rho^i,\rho^m) + \rho^m\left[a\dot{l} + alw_2 f(\rho^i,\rho^m)\pi^m\sqrt{\frac{2}{3}M_{pq}M_{pq}}\right]\right\}\end{aligned} \tag{5.89}$$

The following ratio can be determined from Equations (5.87) and (5.88) such that

$$\frac{\pi^i J^i}{alw_2 f(\rho^i,\rho^m)B\pi^i\sqrt{\frac{2}{3}M_{pq}M_{pq}}} = \frac{\pi^m J^m}{J^m al + alw_2 f(\rho^i,\rho^m)B\pi^m\sqrt{\frac{2}{3}M_{pq}M_{pq}}} \tag{5.90}$$

The constant w_2 can be expressed in terms of the coefficient *B* as follows

$$w_2 = \left[B\pi^m \frac{(J^m - J^i)}{J^i J^m} f(\rho^i,\rho^m)\sqrt{\frac{2}{3}M_{pq}M_{pq}}\right]^{-1} \tag{5.91}$$

The coefficient *b* can then be expressed as follows

$$b = \frac{\pi^m}{al}\left(\frac{J^i}{J^m} - 1\right) \tag{5.92}$$

The coefficient *B* can be defined as follows

$$B = \left[\pi^i J^m g(\rho^i) + (\pi^m J^i - \pi^i J^m) f(\rho^i,\rho^m)\right] \times \left[\pi^m J^i J^m(\rho^i + \rho^m)\right]^{-1} \tag{5.93}$$

Substituting Equation (5.93) into Equation (5.92) gives the expression of w_2 as follows

$$\begin{aligned} w_2 = &\left[\frac{(J^i J^m)^2}{J^m - J^i} f(\rho^i,\rho^m)\right] \\ &\times \left\{ f(\rho^i,\rho^m)\sqrt{\frac{2}{3}M_{pq}M_{pq}}\left[(\pi^m J^i - \pi^i J^m) f(\rho^i,\rho^m) + \pi^i J^m g(\rho^i)\right.\right. \\ &\left.\left. + \rho^m(\pi^m J^i - \pi^m J^m)\frac{\dot{l}}{l}\right]\right\} \end{aligned} \tag{5.94}$$

From the isotropic hardening and kinematic hardening problems, it can be seen that the coefficients are not constants but vary with the dislocation glide velocity and the immobile and mobile dislocation densities as well as with the functions $g(\rho^i)$ and $f(\rho^i,\rho^m)$.

5.5 Shear Band Problem

Shear band, or more generally, strain localization, is a narrow zone of intense plastic shear strain due to the non-uniform deformation, developing severe deformation of ductile materials. Shear band precedes failure as extreme deformation within the shear band leads to intense damage and fracture. The width and direction of the shear bands depend on the material parameters, geometry, boundary conditions, loading distribution and loading rates. The

conditions for bifurcation into a shear band have been given by Hill (1962), Rudnicki and Rice (1975) and Rice (1976) about the discussions of several aspects of shear band localization for various material models.

Shear band is an example of a material instability, corresponding to an abrupt loss of homogeneity of deformation occurring in a solid sample subject to a loading path compatible with continued uniform deformation. The finite element simulations of material instability problems converge to meaningful results upon further refinement of the finite element mesh. The width of the shear band is governed by the intrinsic length scale of a material. However, the classical continuum theory is not able to address this problem as it does not incorporate a length scale parameter in the constitutive equation. Using classical continuum theory, the width of the shear band is introduced through the mesh size and the simulations show that the results are mesh-sensitive. Therefore, in order to remedy the spurious mesh sensitivity of numerical results, an internal length scale is incorporated in the continuum theory. Biaxial compression and a strip in tension are taken as two examples. Both problems are simulated using finite element software ABAQUS. Comparisons are made between the simulations using continuum theory with different mesh sizes and the simulations using nonlocal theory with internal length scales. The simulations using the classical continuum theory are performed by ABAQUS Standard package, while the simulations using nonlocal theory are performed by ABAQUS Standard package with a UMAT user-subroutine which provides the nonlocal constitutive equation with the length scale.

The biaxial compression problem is shown in Figure 5.1 (Abu Al-Rub and Voyiadjis, 2005). The specimen is placed on a smooth rigid plane and the upper edge is constrained to remain horizontal. A vertical deformation is applied to represent a compressive force. The central point of the bottom plate is fixed to avoid rigid body displacement. The forces are set to zero on both sides of the specimen and the horizontal displacements are assumed to be zero along the boundaries as well. The yield strength at the lower-left corner of the specimen is set to be slightly lower than the rest part (10% reduction).

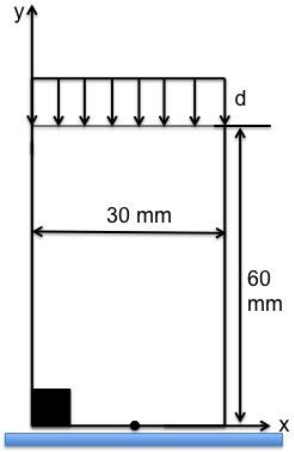

Figure 5.1 Biaxial compression test configuration with an imperfection in the bottom left corner (Abu Al-Rub and Voyiadjis, 2005).

The biaxial compression problem was firstly simulated using the standard plasticity model where the length scale l is set to be zero (Abu Al-Rub and Voyiadjis, 2005). Three different meshes with 15×30, 30×60 and 45×90 integrated eight-noded elements with 3×3 integration points are analyzed. The contour plots of the effective plastic strain are shown in Figure 5.2 for the different meshes respectively. It shows in Figure 5.2 that the width of the strain localization zone (shear band) is dependent on the mesh size, which is not physically sound.

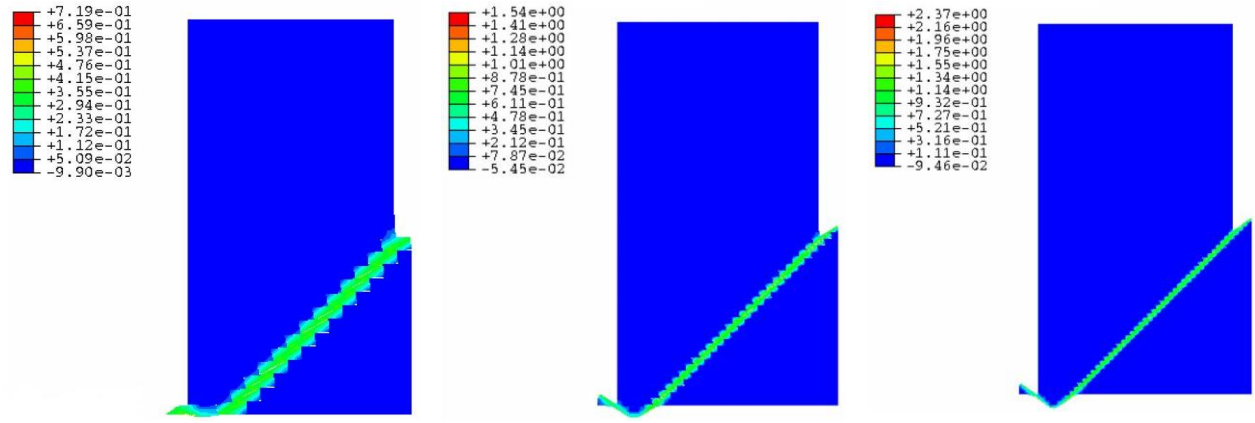

(a) (b) (c)

Figure 5.2 Contour plots of effective plastic strain from different meshes: (a) 15×30, (b) 30×60 and (c) 45×90 with l=0. (Abu Al-Rub and Voyiadjis, 2005)

The simulations were repeated through the nonlocal model with the length scale parameter to be 2.5 mm. The results in Figure 5.3 show that the width of the shear band is dependent on the length scale parameter but not the mesh size.

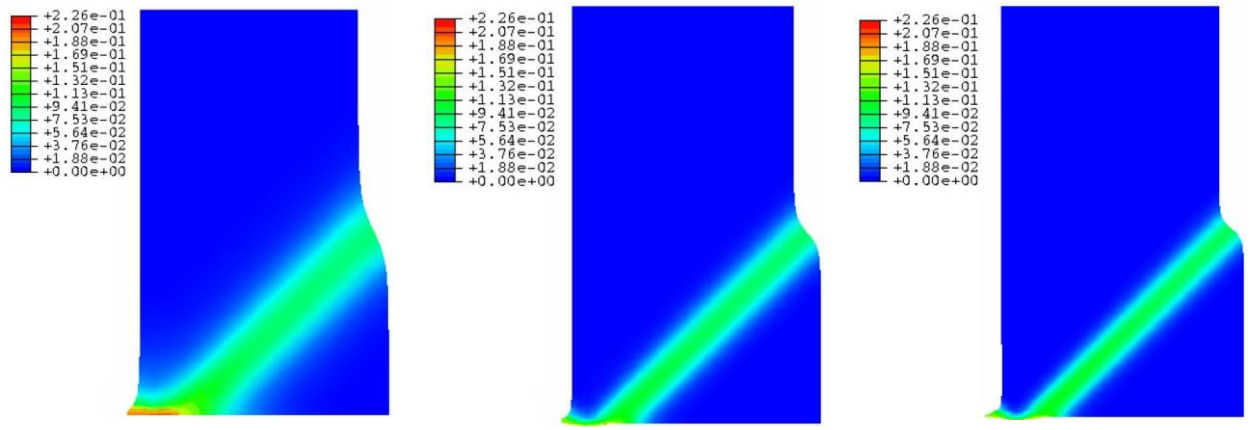

(a) (b) (c)

Figure 5.3 Contour plots of effective plastic strain from different meshes: (a) 15×30, (b) 30×60 and (c) 45×90 with l=2.5 mm. (Abu Al-Rub and Voyiadjis, 2005)

Another example of strip tension problem was solved through the finite element from the standard plasticity model and the nonlocal gradient model. The specimen is shown in Figure 5.4

(Abu Al-Rub and Voyiadjis, 2005). The strip is constrained at the bottom and a displacement is imposed at the top. Two meshes with 10×20 and 20×40 were used with a four-noded quadrilateral plane-strain element. The width of the specimen towards the top was increased slightly in order to avoid a homogenous solution. Therefore, the shear band was initiated at the bottom-left corner with an inclination of 45°.

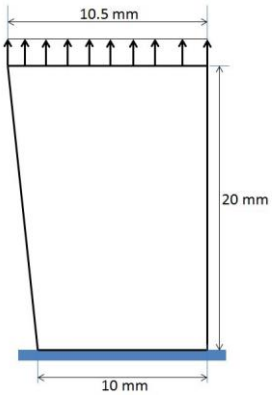

Figure 5.4 Strip in tension problem description (Abu Al-Rub and Voyiadjis, 2005).

The results with l=0 is presented in Figure 5.5 (Abu Al-Rub and Voyiadjis, 2005). It shows that the width of the shear band decreases with the mesh size, which is not realistic. If an internal length scale of 2.5 mm is assigned in the nonlocal gradient model, it shows in Figure 5.6 (Abu Al-Rub and Voyiadjis, 2005) that the effective plastic strain is localized in the shear band with a width that is independent on the mesh size, which is realistic.

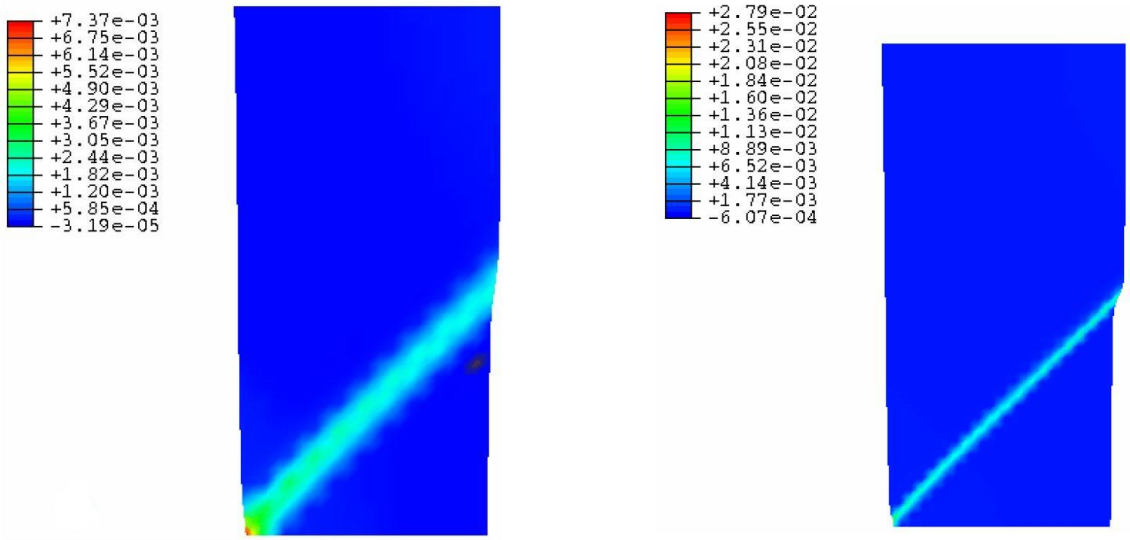

(a) (b)

Figure 5.5 Contour plots of effective plastic strain from different meshes: (a) 10×20 and (b) 20×40 with length scale l=0 (Abu Al-Rub and Voyiadjis, 2005).

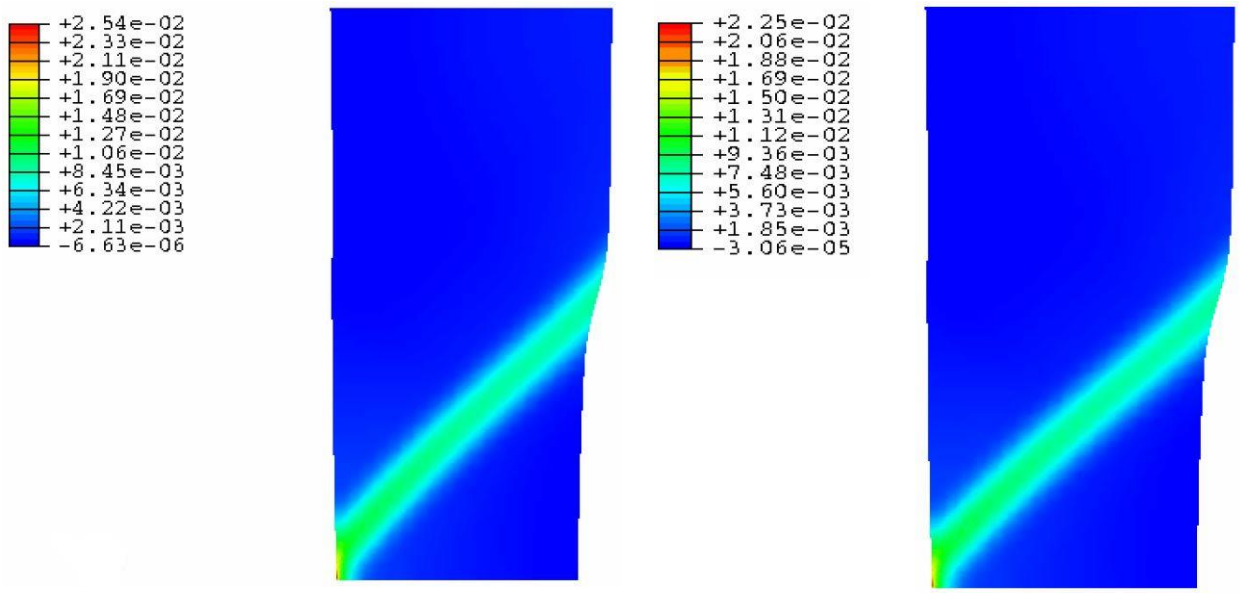

(a) (b)

Figure 5.6 Contour plots of effective plastic strain from different meshes: (a) 10×20 and (b) 20×40 with length scale l=2.5 mm (Abu Al-Rub and Voyiadjis, 2005).

From the two examples above, it can be seen that when solving strain localization problem numerically, a length scale parameter is necessary the size of the localization zone is intrinsic and can be represented by the length scale. The classical continuum theory does not introduce a length scale parameter and therefore, it is not capable in predicting the strain localization problem. Nonlocal theory which incorporates the length scale parameter in the constitutive equation is required and by giving a certain value to the length scale, the simulations will be physically based consistent.

5.6 Conclusion

The nonlocal theory is given in this chapter beginning with the integral format. Taylor series expansion is used in order to approximate the nonlocal measurement in order to reduce the computational cost. Considering various approach of the coupling between the local plastic strain and the strain gradient, a general form of the coupling is obtained in Equation (5.8), which is the starting equation in determining the physically based length scale in Chapters 3 and 4. The nonlocal theory is given from the macro-scale through the thermodynamic consistent model and the micro-scale through the dislocation mechanism.

Shear band problem is given as an example of the importance of the nonlocal theory. Finite element simulation results are compared from simulations using the local plasticity theory and simulations using the nonlocal gradient model. It shows in the results that the simulations are mesh-dependent from the classical continuum theory without a length scale parameter. It also

shows that by assigning a length scale, the simulation results become intrinsic and related to the value of the length scale. Therefore, the finite element simulations with nonlocal model that incorporates the length scale parameter are able to provide more realistic mesh independent results.

CHAPTER 6
SUMMARY, CONCLUSION AND FUTURE PERSPECTIVE

The summary of researches in this dissertation is presented in this Chapter. In addition, the conclusions from this work are deduced. Suggestions and future perspectives based on this researched are also presented.

6.1 Summary

Size effects in metal have been found in many micro-/nano-mechanical tests at small length scales. In nanoindentation tests, instead of the constant hardness shown in macro-hardness tests, the hardness increases at smaller indentation depths. This observation is termed as the indentation size effect (ISE). In order to capture the ISE, the classical continuum mechanics theory is not sufficient as it only predicts the macro-hardness. Strain gradient plasticity theory needs to be enhanced into the classical continuum theory, as strain gradients are presented when the plastic deformation is small. The plastic strain at a local point is not only dependent on the strain at this point but also on the strain gradient in the neighboring space. The strain gradient plasticity theory incorporates a length scale parameter in the constitutive equation in order to characterize the effect of strain gradients on the mechanical behavior of materials.

Nanoindentation is widely employed in order to explore the mechanical behavior in the micro-/nano-scales. It is also frequently applied in order to determine the length scale for the ISE. The determination of the length scale relies on the results from the nanoindentation experiments. Therefore, the accurate testing results are required. The nanoindentation technique measures the material hardness through the load that forces the indenter to penetrate and the projected area of the indenter at certain indentation depth. The projected area is determined not from the direct imaging of the impression but from an area function depending on the indentation depth. The accuracy of the area function thus becomes very important. The area function varies with the geometry of the tip and geometry of the tip may change slightly after frequent uses. In order to determine the correct area function, tip calibration is applied on the fused silica sample. The fused silica sample has an elastic modulus of $72\ GPa$ and does not change along with time as it is very stable. The elastic modulus does not change due to the indentation size effect. The accurate measurement of nanoindentation gives a constant elastic modulus for the fused silica in the entire indentation depth. The calibration procedure followed so that the load-indentation depth data is used to calculate the desired elastic modulus of fused silica. The area function can be determined from curving fitting.

Nanoindentation is very sensitive to the surface conditions, such as surface roughness and strain hardening layer on the surface. The indentation depth is usually in the submicron and nanometers and the ISE is captured even in the smaller indentation depths about tens of nanometers. Therefore, the sample must be prepared carefully for a low surface roughness and deformation-free surface. Mechanical polishing is always applied in order to decrease the surface

roughness by using the polishing particles with decreasing sizes. However, mechanical polishing induces plastic deformation on the surface and even in the material underneath the surface. The deformation is observed by scratches on the surface and the scratches become smaller with the decreasing size of the polishing particles. The smallest size of the polishing particles is $0.05\ \mu m$. Even with this size, the thickness of the deformation layer still can affect the observation of the ISE. Electro-polishing can be applied to remove the deformation without inducing new deformation and to create a deformation-free surface. However, there are many limitations for the electro-polishing such as the choice of the voltage, current and electrolyte. A chemical-mechanical polishing in a vibratory polished can be used instead the electro-polishing to remove the deformation layer.

Instead of the ISE, it has been shown in recent experiments that there is a hardening-softening region in the hardness-indentation depth curve. This phenomenon is attributed to the interaction between dislocations and the grain boundary. Experiments on samples with different grain sizes show that the hardness increases with the decreasing grain size. It is also shown from experiments on single crystals that there is no hardening-softening observed since there is no grain boundary. In order to isolate the influence of the grain boundary, bicrystal samples are used as there is only one grain boundary. Nanoindentation experiments in close proximity of the grain boundary are performed on bicrystals with different distances from the grain boundary. Length scales are determined and vary with the different distances.

In order to investigate the rate dependent of the length scale, a model based on the temperature and rate indentation size effect (TRISE) is developed. The TRISE model is able to predict the classical ISE and the hardening-softening phenomenon. Strain rate is one of the parameters in the TRISE model. By giving different strain rates, the length scale with different strain rates can be determined. The TRISE model is modified for the application in bicrystals by replacing the grain size parameter for polycrystalline materials with the distance between the indenter tip and the grain boundary for bicrystal samples. Nanoindentation experiments are performed on bicrystals near the grain boundary with different distances. From the modified TRISE model and the experimental results, the length scales at different distances are determined, proving a new type of size effect.

6.2 Conclusions

The following conclusions are drawn from the work of this dissertation:

1. The TRISE model is able to predict the indentation size effect. The length scale determined from the model and nanoindentation experiments shows that it decreases with the increase of equivalent plastic strain. This characterizes the fact that the strain gradient becomes greater when the deformation is smaller.

2. The length scale approaches to zero when the strain is large. This is true because for large deformation, there is no strain gradient and thus the length scale is equal to zero.

3. The hardening-softening phenomenon can be captured by the TRISE model for polycrystalline materials by incorporating a grain size parameter. The hardness increases with the decreasing grain size. The length scale with different grain sizes is determined and shows that it decreases as the grain size decreases, resulting in a greater hardness.

4. The rate dependency during nanoindentation can be captured by the TRISE model. It shows from the model that the hardness increases with the increasing strain rate, which matches with the experimental observation. The length scale at different strain rates is determined and it shows that the length scale decreases with the increasing strain rate.

5. In order to isolate the grain boundary effect, bicrystal samples are used for nanoindentation experiments near the grain boundary at different distances. The experimental results show that the hardening effect becomes greater when the distance between the indenter tip and the grain boundary becomes smaller. The TRISE model is modified for bicrystal samples and is able to predict the size effect induced by the proximity of the grain boundary. The length scale at different distances is determined from the modified TRISE model and the nanoindentation experiments on bicrystal samples. It shows that the length scale decreases when the distance is smaller.

6.3 Suggestions and future perspectives

The modified TRISE model for bicrystal shows that it is able to predict the behaviors in bicrystal face-centered cubic (FCC) metals from the research on bicrystal copper and aluminum. The compatibility to body-centered cubic (BCC) metals is suggested to be investigated.

The hardening-softening phenomenon is believed to be the interaction between the grain boundary and the dislocations. In this research, the dislocation density is calculated based on the work of Nix and Gao (1998) and Yang and Vehoff (2007). The experimental observation of the dislocation density is not shown. Electron backscatter diffraction (EBSD) shows from the measure of the lattice parameters, the dislocation density can be determined. The in-situ dislocation density can be obtained through the EBSD in combination with FIB.

The transmission of dislocations across the grain boundary depends on the misorientation from two grains. With different misorientations, the energy required for a transfer is different. This may lead to the difference in the dislocation accumulation, resulting in the change of hardness in the hardening effect. Crystal plasticity needs to be used to characterize the difference between different misorientations.

BIBLIOGRAPHY

Part I: by the Author

Voyiadjis, George Z., Danial Faghihi, and Cheng Zhang. "Analytical and experimental determination of rate-and temperature-dependent length scales using nanoindentation experiments." Journal of Nanomechanics and Micromechanics 1, no. 1 (2011): 24-40.

Voyiadjis, George Z., and Cheng Zhang. "The mechanical behavior during nanoindentation near the grain boundary in a bicrystal FCC metal." Materials Science and Engineering: A 621 (2015): 218-228.

Zhang, Cheng, and George Z. Voyiadjis. "Rate-dependent size effects and material length scales in nanoindentation near the grain boundary for a bicrystal FCC metal." *Materials Science and Engineering: A* 659 (2016): 55-62.

Part II: by Other Authors

Abed, Farid H., and George Z. Voyiadjis. "A consistent modified Zerilli-Armstrong flow stress model for BCC and FCC metals for elevated temperatures." Acta Mechanica 175, no. 1-4 (2005): 1-18.

Abed, Farid H., and George Z. Voyiadjis. "Adiabatic shear band localizations in BCC metals at high strain rates and various initial temperatures." International Journal for Multiscale Computational Engineering 5, no. 3-4 (2007a).

Abed, Farid H., and George Z. Voyiadjis. "Thermodynamic consistent formulations of viscoplastic deformations in FCC metals." Journal of engineering mechanics 133, no. 1 (2007b): 76-86.

Abu Al-Rub, Rashid K., and George Z. Voyiadjis. "A direct finite element implementation of the gradient-dependent theory." International Journal for Numerical Methods in Engineering 63, no. 4 (2005): 603-629.

Al-Rub, Rashid K. Abu, and George Z. Voyiadjis. "Analytical and experimental determination of the material intrinsic length scale of strain gradient plasticity theory from micro-and nano-indentation experiments." International Journal of Plasticity 20, no. 6 (2004): 1139-1182.

Al-Rub, Rashid K. Abu, and George Z. Voyiadjis. "Determination of the material intrinsic length scale of gradient plasticity theory." International Journal for Multiscale Computational Engineering 2, no. 3 (2004).

Aifantis, Elias C. "On the microstructural origin of certain inelastic models." Journal of Engineering Materials and technology 106, no. 4 (1984): 326-330.

Aifantis, Elias C. "The physics of plastic deformation." International Journal of Plasticity 3, no. 3 (1987): 211-247.

Aifantis, Elias C. "On the role of gradients in the localization of deformation and fracture." International Journal of Engineering Science 30, no. 10 (1992): 1279-1299.

Aifantis, Elias C. "Gradient deformation models at nano, micro, and macro scales." Journal of Engineering Materials and Technology 121, no. 2 (1999a): 189-202.

Aifantis, Elias C. "Strain gradient interpretation of size effects." International Journal of Fracture 95, no. 1-4 (1999b): 299-314.

Aifantis, K. E., W. A. Soer, J. Th M. De Hosson, and J. R. Willis. "Interfaces within strain gradient plasticity: theory and experiments." Acta Materialia 54, no. 19 (2006): 5077-5085.

Almasri, Amin H., and George Z. Voyiadjis. "Effect of strain rate on the dynamic hardness in metals." Journal of Engineering Materials and Technology 129, no. 4 (2007): 505-512.

Almasri, Amin H., and George Z. Voyiadjis. "Nano-indentation in FCC metals: experimental study." Acta Mechanica 209, no. 1-2 (2010): 1-9.

Almasri, Amin H., and George Z. Voyiadjis. "Physically based constitutive model for body centered cubic metals with applications to iron." Journal of engineering mechanics 134, no. 7 (2008): 521-529.

Andrews, E. W., A. E. Giannakopoulos, E. Plisson, and S. Suresh. "Analysis of the impact of a sharp indenter." International journal of solids and structures 39, no. 2 (2002): 281-295.

Anton, Richard J., and Ghatu Subhash. "Dynamic Vickers indentation of brittle materials." Wear 239, no. 1 (2000): 27-35.

Arsenlis, A., and D. M. Parks. "Crystallographic aspects of geometrically-necessary and statistically-stored dislocation density." Acta Materialia 47, no. 5 (1999): 1597-1611.

Arzt, El. "Size effects in materials due to microstructural and dimensional constraints: a comparative review." Acta materialia 46, no. 16 (1998): 5611-5626.

Aust, K. T., R. E. Hanneman, P. Niessen, and J. H. Westbrook. "Solute induced hardening near grain boundaries in zone refined metals." Acta Metallurgica 16, no. 3 (1968): 291-302.

Bammann, D. J., and E. C. Aifantis. "A model for finite-deformation plasticity." Acta Mechanica 69, no. 1-4 (1987): 97-117.

Bammann, D. J., D. Mosher, D. A. Hughes, N. R. Moody, and P. R. Dawson. Using spatial gradients to model localization phenomena. No. SAND99-8588. Sandia National Labs., Albuquerque, NM (US); Sandia National Labs., Livermore, CA (US), 1999.

Bammann, Douglas J. "A model of crystal plasticity containing a natural length scale." Materials Science and Engineering: A 309 (2001): 406-410.

Bammann, Douglas John, and E. C. Aifantis. "On a proposal for a continuum with microstructure." Acta Mechanica 45, no. 1-2 (1982): 91-121.

Barlat, F., R. C. Becker, Y. Hayashida, Y. Maeda, M. Yanagawa, K. Chung, J. C. Brem et al. "Yielding description for solution strengthened aluminum alloys." International Journal of Plasticity 13, no. 4 (1997a): 385-401.

Barlat, F., Y. Maeda, K. Chung, M. Yanagawa, J. C. Brem, Y. Hayashida, D. J. Lege et al. "Yield function development for aluminum alloy sheets." Journal of the Mechanics and Physics of Solids 45, no. 11 (1997b): 1727-1763.

Bazant, Zdenek P., and Joško Ozbolt. "Nonlocal microplane model for fracture, damage, and size effect in structures." Journal of Engineering Mechanics 116, no. 11 (1990): 2485-2505.

Begley, Matthew R., and John W. Hutchinson. "The mechanics of size-dependent indentation." Journal of the Mechanics and Physics of Solids 46, no. 10 (1998): 2049-2068.

Bishop, J. F. W., and Rodney Hill. "CXXVIII. A theoretical derivation of the plastic properties of a polycrystalline face-centred metal." The London, Edinburgh, and Dublin Philosophical Magazine and Journal of Science 42, no. 334 (1951): 1298-1307.

Busso, E. P., F. T. Meissonnier, and N. P. O'dowd. "Gradient-dependent deformation of two-phase single crystals." Journal of the Mechanics and Physics of Solids 48, no. 11 (2000): 2333-2361.

Chen, S. H., and T. C. Wang. "Interface crack problems with strain gradient effects." International journal of fracture 117, no. 1 (2002): 25-37.

Chen, Xi, Nagahisa Ogasawara, Manhong Zhao, and Norimasa Chiba. "On the uniqueness of measuring elastoplastic properties from indentation: the indistinguishable mystical materials." Journal of the Mechanics and Physics of Solids 55, no. 8 (2007): 1618-1660.

Chong, Arthur CM, and David CC Lam. "Strain gradient plasticity effect in indentation hardness of polymers." Journal of Materials Research 14, no. 10 (1999): 4103-4110.

Conrad, H., A. F. Sprecher, S. L. Mannan, E. C. Aifantis, and J. P. Hirth. "The Mechanics of Dislocations." ASM (1985): 225.

De Borst, Rene, and Jerzy Pamin. "Some novel developments in finite element procedures for gradient-dependent plasticity." International Journal for Numerical Methods in Engineering 39, no. 14 (1996): 2477-2505.

De Borst, René, and Hans-Bernd Mühlhaus. "Gradient- dependent plasticity: Formulation and algorithmic aspects." International Journal for Numerical Methods in Engineering 35, no. 3 (1992): 521-539.

De Borst, R., L. J. Sluys, H-B. Muhlhaus, and Jerzy Pamin. "Fundamental issues in finite element analyses of localization of deformation." Engineering computations 10, no. 2 (1993): 99-121.

De Guzman, Melissa Shell, Gabi Neubauer, Paul Flinn, and William D. Nix. "The role of indentation depth on the measured hardness of materials." In MRS proceedings, vol. 308, p. 613. Cambridge University Press, 1993.

Delincé, Marc, P. J. Jacques, and Thomas Pardoen. "Separation of size-dependent strengthening contributions in fine-grained Dual Phase steels by nanoindentation." Acta materialia 54, no. 12 (2006): 3395-3404.

Dieter, G. E., and D. Bacon. "Mechanical Metallurgy, vol. 3McGraw-Hill." New York (1986).

Dorgan, Robert J., and George Z. Voyiadjis. "Nonlocal dislocation based plasticity incorporating gradients of hardening." Mechanics of materials 35, no. 8 (2003): 721-732.

Dowling, Norman E. Mechanical behavior of materials: engineering methods for deformation, fracture, and fatigue. Prentice hall, 1993.

Elmustafa, A. A., and D. S. Stone. "Indentation size effect in polycrystalline FCC metals." Acta Materialia 50, no. 14 (2002): 3641-3650.

Faghihi, D., and G. Z. Voyiadjis. "Size effects and length scales in nanoindentation for body-centred cubic materials with application to iron." Proceedings of the Institution of Mechanical Engineers, Part N: Journal of Nanoengineering and Nanosystems 224, no. 1-2 (2010): 5-18.

Faghihi, Danial, and George Z. Voyiadjis. "Determination of nanoindentation size effects and variable material intrinsic length scale for body-centered cubic metals." Mechanics of Materials 44 (2012): 189-211.

Fleck, N. A., and J. W. Hutchinson. "A phenomenological theory for strain gradient effects in plasticity." Journal of the Mechanics and Physics of Solids 41, no. 12 (1993): 1825-1857.

Fleck, N. A., and J. W. Hutchinson. "Strain gradient plasticity." Advances in applied mechanics 33 (1997): 296-361.

Fleck, N. A., G. M. Muller, M. F. Ashby, and J. W. Hutchinson. "Strain gradient plasticity: theory and experiment." Acta Metallurgica et Materialia 42, no. 2 (1994): 475-487.

Follansbee, P_S, G. Regazzoni, and U. F. Kocks. "The transition to drag-controlled deformation in copper at high strain rates." Mechanical Properties at High Rates of Strain, 1984 (1984): 71-80.

Gao, H., Y. Huang, and W. D. Nix. "Modeling plasticity at the micrometer scale." Naturwissenschaften 86, no. 11 (1999a): 507-515.

Gao, H., Y. Huang, W. D. Nix, and J. W. Hutchinson. "Mechanism-based strain gradient plasticity—I. Theory." Journal of the Mechanics and Physics of Solids 47, no. 6 (1999b): 1239-1263.

Gao, Huajian, and Yonggang Huang. "Geometrically necessary dislocation and size-dependent plasticity." Scripta Materialia 48, no. 2 (2003): 113-118.

Gao, Huajian, and Yonggang Huang. "Taylor-based nonlocal theory of plasticity." International Journal of Solids and Structures 38, no. 15 (2001): 2615-2637.

Gilman, J. J., and W. G. Johnston. "Dislocations and mechanical properties of crystals." Fisher, J., Johnston, W., Thomson, R., Vreeland, T.(eds.) (1957): 116.

Glema, Adam, Tomasz Łodygowski, and Piotr Perzyna. "Interaction of deformation waves and localization phenomena in inelastic solids." Computer Methods in Applied Mechanics and Engineering 183, no. 1 (2000): 123-140.

Gracio, J. J. "The double effect of grain size on the work hardening behaviour of polycrystalline copper." Scripta metallurgica et materialia 31, no. 4 (1994): 487-489.

Guo, Y., Y. Huang, H. Gao, Z. Zhuang, and K. C. Hwang. "Taylor-based nonlocal theory of plasticity: numerical studies of the micro-indentation experiments and crack tip fields." International Journal of Solids and Structures 38, no. 42 (2001): 7447-7460.

Haque, M. A., and M. T. A. Saif. "A review of MEMS-based microscale and nanoscale tensile and bending testing." Experimental mechanics 43, no. 3 (2003): 248-255.

Hill, Rodney. "Acceleration waves in solids." Journal of the Mechanics and Physics of Solids 10, no. 1 (1962): 1-16.

Hill, Rodney. The mathematical theory of plasticity. Vol. 11. Oxford university press, 1998.

Huang, Y., Z. Xue, H. Gao, W. D. Nix, and Z. C. Xia. "A study of microindentation hardness tests by mechanism-based strain gradient plasticity." Journal of Materials Research 15, no. 08 (2000): 1786-1796.

Huber, N., W. D. Nix, and H. Gao. "Identification of elastic-plastic material parameters from pyramidal indentation of thin films." In Proceedings of the Royal Society of London A: Mathematical, Physical and Engineering Sciences, vol. 458, no. 2023, pp. 1593-1620. The Royal Society, 2002.

Hwang, K. C., H. Jiang, Y. Huang, and H. Gao. "Finite deformation analysis of mechanism-based strain gradient plasticity: torsion and crack tip field." International Journal of Plasticity 19, no. 2 (2003): 235-251.

Joslin, D. L., and W. C. Oliver. "A new method for analyzing data from continuous depth-sensing microindentation tests." Journal of Materials Research 5, no. 1 (1990): 123-126.

Kocks, U. F. "The relation between polycrystal deformation and single-crystal deformation." Metallurgical and Materials Transactions 1, no. 5 (1970): 1121-1143.

Koeppel, B. J., and G. Subhash. "Characteristics of residual plastic zone under static and dynamic Vickers indentations." Wear 224, no. 1 (1999): 56-67.

Krieg, R. D., and D. B. Krieg. "Accuracies of numerical solution methods for the elastic-perfectly plastic model." Journal of Pressure Vessel Technology 99, no. 4 (1977): 510-515.

Kröner, E. "Elasticity theory of materials with long range cohesive forces." International Journal of Solids and Structures 3, no. 5 (1967): 731-742.

Kumar, A., and R. Gg Kumble. "Viscous drag on dislocations at high strain rates in copper." Journal of Applied Physics 40, no. 9 (1969): 3475-3480.

Li, Shaofan, Wing Kam Liu, Ares J. Rosakis, Ted Belytschko, and Wei Hao. "Mesh-free Galerkin simulations of dynamic shear band propagation and failure mode transition." International Journal of solids and structures 39, no. 5 (2002): 1213-1240.

Lim, Yong Yee, Andrew J. Bushby, and M. Munawar Chaudhri. "Nano and macro indentation studies of polycrystalline copper using spherical indenters." In MRS Proceedings, vol. 522, p. 145. Cambridge University Press, 1998.

Lim, Yong Yee, and M. Munawar Chaudhri. "The effect of the indenter load on the nanohardness of ductile metals: an experimental study on polycrystalline work-hardened and annealed oxygen-free copper." Philosophical Magazine A 79, no. 12 (1999): 2979-3000.

Lu, Jun, Subra Suresh, and Guruswami Ravichandran. "Dynamic indentation for determining the strain rate sensitivity of metals." Journal of the Mechanics and Physics of Solids 51, no. 11 (2003): 1923-1938.

Ma, Qing, and David R. Clarke. "Size dependent hardness of silver single crystals." Journal of Materials Research 10, no. 04 (1995): 853-863.

McElhaney, K. W., J. J. Vlassak, and W. D. Nix. "Determination of indenter tip geometry and indentation contact area for depth-sensing indentation experiments." Journal of Materials Research 13, no. 05 (1998): 1300-1306.

Menzel, A., and P. Steinmann. "On the continuum formulation of higher gradient plasticity for single and polycrystals." Journal of the Mechanics and Physics of Solids 48, no. 8 (2000): 1777-1796.

Miyahara, Kensuke, Saburo Matsuoka, and Nobuo Nagashima. "Nanoindentation Measurement for a Tungsten (001) Single Crystal." JSME International Journal Series A Solid Mechanics and Material Engineering 41, no. 4 (1998): 562-568.

Moon, D. W., and T. Vreeland Jr. "Dislocation Velocity in Single and Polycrystalline Silicon-Iron." Journal of applied physics 39, no. 3 (1968): 1766-1770.

Muhlhaus, H. B., and E. C. Aifantis. "The influence of microstructure-induced gradients on the localization of deformation in viscoplastic materials." Acta mechanica 89, no. 1-4 (1991): 217-231.

Nemat-Nasser, Sia, and Yulong Li. "Flow stress of fcc polycrystals with application to OFHC Cu." Acta Materialia 46, no. 2 (1998): 565-577.

Nix, William D., and Huajian Gao. "Indentation size effects in crystalline materials: a law for strain gradient plasticity." Journal of the Mechanics and Physics of Solids 46, no. 3 (1998): 411-425.

Nye, J. F. "Some geometrical relations in dislocated crystals." Acta metallurgica 1, no. 2 (1953): 153-162.

Oliver, Warren Carl, and George Mathews Pharr. "An improved technique for determining hardness and elastic modulus using load and displacement sensing indentation experiments." Journal of materials research 7, no. 06 (1992): 1564-1583.

Orowan, E. "Mechanical strength properties and real structure of crystals." Z. Kristallogr 89, no. 3/4 (1934): 327-343.

Ortiz, M., and J. C. Simo. "An analysis of a new class of integration algorithms for elastoplastic constitutive relations." International Journal for Numerical Methods in Engineering 23, no. 3 (1986): 353-366.

Rice, James R. The localization of plastic deformation. Division of Engineering, Brown University, 1976.

Rudnicki, John Walter, and J. R. Rice. "Conditions for the localization of deformation in pressure-sensitive dilatant materials." Journal of the Mechanics and Physics of Solids 23, no. 6 (1975): 371-394.

Saha, Ranjana, Zhenyu Xue, Young Huang, and William D. Nix. "Indentation of a soft metal film on a hard substrate: strain gradient hardening effects." Journal of the Mechanics and Physics of Solids 49, no. 9 (2001): 1997-2014.

Schmid, Erich, and Walter Boas. "Plasticity of crystals." (1950).

Senseny, P. E., J. Duffy, and R. H. Hawley. "Experiments on strain rate history and temperature effects during the plastic deformation of close-packed metals." Journal of Applied Mechanics 45, no. 1 (1978): 60-66.

Shioiri, J., and K. Satoh. "An ultrasonic study of the rate controlling mechanism of dislocation motion at high rates of strain." Le Journal de Physique Colloques 46, no. C5 (1985): C5-3.

Simo, J. C., and T. J. R. Hughes. "On the variational foundations of assumed strain methods." Journal of Applied Mechanics 53, no. 1 (1986): 51-54.

Soer, W. A., K. E. Aifantis, and J. Th M. De Hosson. "Incipient plasticity during nanoindentation at grain boundaries in body-centered cubic metals." Acta Materialia 53, no. 17 (2005): 4665-4676.

Soer, W. A., and J. Th M. De Hosson. "Detection of grain-boundary resistance to slip transfer using nanoindentation." Materials Letters 59, no. 24 (2005): 3192-3195.

Soifer, Ya M., A. Verdyan, M. Kazakevich, and E. Rabkin. "Nanohardness of copper in the vicinity of grain boundaries." Scripta materialia 47, no. 12 (2002): 799-804.

Staker, M. R., and D. L. Holt. "The dislocation cell size and dislocation density in copper deformed at temperatures between 25 and 700 C." Acta Metallurgica 20, no. 4 (1972): 569-579.

Stelmashenko, N. A., M. G. Walls, L. M. Brown, and Yu V. Milman. "Microindentations on W and Mo oriented single crystals: an STM study." Acta Metallurgica et Materialia 41, no. 10 (1993): 2855-2865.

Stölken, J. S., and A. G. Evans. "A microbend test method for measuring the plasticity length scale." Acta Materialia 46, no. 14 (1998): 5109-5115.

Swadener, J. G., E. P. George, and G. M. Pharr. "The correlation of the indentation size effect measured with indenters of various shapes." Journal of the Mechanics and Physics of Solids 50, no. 4 (2002a): 681-694.

Swadener, J. G., A. Misra, R. G. Hoagland, and M. Nastasi. "A mechanistic description of combined hardening and size effects." Scripta materialia 47, no. 5 (2002b): 343-348.

Tabor, D. "The hardness and strength of metals." Journal of the Institute of Metals 79, no. 1 (1951): 1-18.

Tanner, Albert B., Robert D. McGinty, and David L. McDowell. "Modeling temperature and strain rate history effects in OFHC Cu." International Journal of Plasticity 15, no. 6 (1999): 575-603.

Vardoulakis, I., and E. C. Aifantis. "A gradient flow theory of plasticity for granular materials." Acta Mechanica 87, no. 3-4 (1991): 197-217.

Voyiadjis, G. Z., and I. N. Basuroychowdhury. "A plasticity model for multiaxial cyclic loading and ratchetting." Acta Mechanica 126, no. 1-4 (1998): 19-35.

Voyiadjis, G. Z., and R. J. Dorgan. "Gradient formulation in coupled damage-plasticity." Archives of Mechanics 53, no. 4-5 (2001): 565-597.

Voyiadjis, George Z., and Farid H. Abed. "Effect of dislocation density evolution on the thermomechanical response of metals with different crystal structures at low and high strain rates and temperatures." Archives of Mechanics 57, no. 4 (2005a): 299-343.

Voyiadjis, George Z., and Farid H. Abed. "Implicit algorithm for finite deformation hypoelastic–viscoplasticity in fcc metals." International journal for numerical methods in engineering 67, no. 7 (2006): 933-959.

Voyiadjis, George Z., and Farid H. Abed. "Microstructural based models for bcc and fcc metals with temperature and strain rate dependency." Mechanics of Materials 37, no. 2 (2005b): 355-378.

Voyiadjis, George Z., and Amin H. Almasri. "A physically based constitutive model for fcc metals with applications to dynamic hardness." Mechanics of Materials 40, no. 6 (2008): 549-563.

Voyiadjis, George Z., and Amin H. Almasri. "Variable material length scale associated with nanoindentation experiments." Journal of engineering mechanics 135, no. 3 (2009): 139-148.

Voyiadjis, George Z., Amin H. Almasri, and Taehyo Park. "Experimental nanoindentation of BCC metals." Mechanics Research Communications 37, no. 3 (2010): 307-314.

Voyiadjis, George Z., and Rashid K. Abu Al-Rub. "Gradient plasticity theory with a variable length scale parameter." International Journal of Solids and Structures 42, no. 14 (2005): 3998-4029.

Voyiadjis, George Z., and Rashid K. Abu Al-Rub. "Thermodynamic based model for the evolution equation of the backstress in cyclic plasticity." International Journal of Plasticity 19, no. 12 (2003): 2121-2147.

Voyiadjis, George Z., and N. Ellis Buckner. "Indentation of a half- space with a rigid indentor." International journal for numerical methods in engineering 19, no. 10 (1983): 1555-1578.

Voyiadjis, George Z., and Babur Deliktas. "Multi-scale analysis of multiple damage mechanisms coupled with inelastic behavior of composite materials." Mechanics research communications 27, no. 3 (2000): 295-300.

Voyiadjis, George Z., Babur Deliktas, and Elias C. Aifantis. "Multiscale analysis of multiple damage mechanisms coupled with inelastic behavior of composite materials." Journal of Engineering Mechanics 127, no. 7 (2001): 636-645.

Voyiadjis, George Z., Babur Deliktas, Danial Faghihi, and Adam Lodygowski. "Friction coefficient evaluation using physically based viscoplasticity model at the contact region during high velocity sliding." Acta mechanica 213, no. 1-2 (2010): 39-52.

Voyiadjis, George Z., and Danial Faghihi. "Variable (intrinsic) material length scale for face-centred cubic metals using nano-indentation." Proceedings of the Institution of Mechanical Engineers, Part N: Journal of Nanoengineering and Nanosystems 224, no. 3 (2010): 123-147.

Voyiadjis, George Z., and Rick Peters. "Size effects in nanoindentation: an experimental and analytical study." Acta Mechanica 211, no. 1-2 (2010): 131-153.

Voyiadjis, George Z., Andrew A. Poe, and Panos D. Kiousis. "Finite-strain, elasto-plastic solution for contact problems." Journal of Engineering Mechanics 112, no. 3 (1986): 273-292.

Vukelic, S., I. C. Noyan, J. W. Kysar, and Y. L. Yao. "Characterization of Heterogeneous Response of Al Bicrystal Subject to Micro Scale Laser Shock Peening." Experimental Mechanics 51, no. 5 (2011): 793-796.

Vukelic, Sinisa, Youneng Wang, Jeffrey W. Kysar, and Y. Lawrence Yao. "Dynamic material response of aluminum single crystal under microscale laser shock peening." Journal of Manufacturing Science and Engineering 131, no. 3 (2009): 031015.

Walgraef, Daniel, and Elias C. Aifantis. "On the formation and stability of dislocation patterns—III: Three-dimensional considerations." International journal of engineering science 23, no. 12 (1985): 1365-1372.

Walgraef, Daniel, and Elias Aifantis. "Plastic instabilities, dislocation patterns and nonequilibrium phenomena." Res mechanica 23, no. 2-3 (1988): 161-195.

Wang, M. G., and A. H. W. Ngan. "Indentation strain burst phenomenon induced by grain boundaries in niobium." Journal of materials research 19, no. 08 (2004): 2478-2486.

Wang, W., Y. Huang, K. J. Hsia, K. X. Hu, and A. Chandra. "A study of microbend test by strain gradient plasticity." International Journal of Plasticity 19, no. 3 (2003): 365-382.

Wang, Zhigang, Hongbin Bei, Easo P. George, and George M. Pharr. "Influences of surface preparation on nanoindentation pop-in in single-crystal Mo." Scripta Materialia 65, no. 6 (2011): 469-472.

Westbrook, J. H., and K. T. Aust. "Solute hardening at interfaces in high-purity lead—I Grain and twin boundaries." Acta Metallurgica 11, no. 10 (1963): 1151-1163.

Xiang, Y., and J. J. Vlassak. "Bauschinger effect in thin metal films." Scripta Materialia 53, no. 2 (2005): 177-182.

Xue, Z., Y. Huang, K. C. Hwang, and M. Li. "The influence of indenter tip radius on the micro-indentation hardness." Journal of Engineering Materials and Technology 124, no. 3 (2002a): 371-379.

Xue, Z., Y. Huang, and M. Li. "Particle size effect in metallic materials: a study by the theory of mechanism-based strain gradient plasticity." Acta Materialia 50, no. 1 (2002b): 149-160.

Xue, Zhenyu, M. Saif, and Yonggang Huang. "The strain gradient effect in microelectromechanical systems (MEMS)." Microelectromechanical Systems, Journal of 11, no. 1 (2002c): 27-35.

Yang, B., and H. Vehoff. "Dependence of nanohardness upon indentation size and grain size–a local examination of the interaction between dislocations and grain boundaries." Acta Materialia 55, no. 3 (2007): 849-856.

Yuan, Huang, and Jian Chen. "Identification of the intrinsic material length in gradient plasticity theory from micro-indentation tests." International journal of solids and structures 38, no. 46 (2001): 8171-8187.

Zbib, H. M., and E. C. Aifantis. "On the gradient-dependent theory of plasticity and shear banding." Acta mechanica 92, no. 1-4 (1992): 209-225.

Zbib, H. M., and E. C. Aifantis. "On the localization and postlocalization behavior of plastic deformation. I: On the initiation of shear bands." Res Mechanica 23, no. 2-3 (1988): 261-277.

APPENDIX
ELSEVIER LICENSES

1. Elsevier License Number One

1.1 Confirmation Letter

Copyright Clearance Center <rightslink@marketing.copyright.com>
Fri 3/18/2016 11:35 AM
To: Cheng Zhang <czhan16@lsu.edu>;

Dear Mr. Cheng Zhang,

Thank you for placing your order through Copyright Clearance Center's RightsLink service. Elsevier has partnered with RightsLink to license its content. This notice is a confirmation that your order was successful.

Your order details and publisher terms and conditions are available by clicking the link below: http://s100.copyright.com/CustomerAdmin/PLF.jsp?ref=59a83541-b146-4653-ab2e-3018aaf8659d

Order Details
Licensee: Cheng Zhang
License Date: Mar 18, 2016
License Number: 3832010596485
Publication: Materials Science and Engineering: A
Title: Rate-dependent size effects and material length scales in nanoindentation near the grain boundary for a bicrystal FCC metal
Type of Use: reuse in a thesis/dissertation
Total: 0.00 USD

To access your account, please visit https://myaccount.copyright.com.

Please note: Online payments are charged immediately after order confirmation; invoices are issued daily and are payable immediately upon receipt.

To ensure that we are continuously improving our services, please take a moment to complete our customer satisfaction survey.

B.1:v4.2

1.2 Order Details

The following is the license issued with more details. Please note that the portion to be allowed for reuse is “full article”.

Supplier	Elsevier Limited The Boulevard, Langford Lane Kidlington, Oxford, OX5 1GB, UK
Registered Company Number	1982084
Customer Name	Cheng Zhang
Customer Address	4606 Y A Tittle Ave Apt 20 Baton Rouge, LA 70820
License Number	3832010596485
License Date	Mar 18, 2016
Licensed Content Publisher	Elsevier
Licensed Content Publication	Materials Science and Engineering: A
Licensed Content Title	Rate-dependent size effects and material length scales in nanoindentation near the grain boundary for a bicrystal FCC metal
Licensed Content Author	Cheng Zhang, George Z. Voyiadjis
Licensed Content Date	6 April 2016
Licensed Content Volume Number	659
Licensed Content Issue Number	n/a
Number of Pages	8
Start Page	55
End Page	62
Type of Use	reuse in a thesis/dissertation
Portion	full article
Format	both print and electronic
Are you the author of this Elsevier article?	Yes
Will you be translating?	No
Title of Your Thesis/Dissertation	Constitutive Modeling and Experiments for the Micro and Nano Behaviors in Metals
Expected Completion Date	May 2016
Estimated Size (Number of Pages)	100
Elsevier VAT Number	GB 494 6272 12

2. Elsevier License Number Two

2.1 Confirmation Letter

Copyright Clearance Center <rightslink@marketing.copyright.com>
Fri 3/18/2016 11:37 AM
To: Cheng Zhang <czhan16@lsu.edu>;

Dear Mr. Cheng Zhang,

Thank you for placing your order through Copyright Clearance Center's RightsLink service. Elsevier has partnered with RightsLink to license its content. This notice is a confirmation that your order was successful.

Your order details and publisher terms and conditions are available by clicking the link below: http://s100.copyright.com/CustomerAdmin/PLF.jsp?ref=f45073a1-565e-4b91-af70-577f2b40e615

Order Details
Licensee: Cheng Zhang
License Date: Mar 18, 2016
License Number: 3832010667499
Publication: Materials Science and Engineering: A
Title: The mechanical behavior during nanoindentation near the grain boundary in a bicrystal FCC metal
Type of Use: reuse in a thesis/dissertation
Total: 0.00 USD

To access your account, please visit https://myaccount.copyright.com.

Please note: Online payments are charged immediately after order confirmation; invoices are issued daily and are payable immediately upon receipt.

To ensure that we are continuously improving our services, please take a moment to complete our customer satisfaction survey.

B.1:v4.2

2.2 Order Details

The following is the license issued with more details. Please note that the portion to be allowed for reuse is “full article”.

Supplier	Elsevier Limited The Boulevard, Langford Lane Kidlington, Oxford, OX5 1GB, UK
Registered Company Number	1982084
Customer Name	Cheng Zhang
Customer Address	4606 Y A Tittle Ave Apt 20 Baton Rouge, LA 70820
License Number	3832010667499
License Date	Mar 18, 2016
Licensed Content Publisher	Elsevier
Licensed Content Publication	Materials Science and Engineering: A
Licensed Content Title	Rate-dependent size effects and material length scales in nanoindentation near the grain boundary for a bicrystal FCC metal
Licensed Content Author	George Z. Voyiadjis, Cheng Zhang
Licensed Content Date	5 January 2015
Licensed Content Volume Number	621
Licensed Content Issue Number	n/a
Number of Pages	11
Start Page	218
End Page	228
Type of Use	reuse in a thesis/dissertation
Portion	full article
Format	both print and electronic
Are you the author of this Elsevier article?	Yes
Will you be translating?	No
Title of Your Thesis/Dissertation	Constitutive Modeling and Experiments for the Micro and Nano Behaviors in Metals
Expected Completion Date	May 2016
Estimated Size (Number of Pages)	100
Elsevier VAT Number	GB 494 6272 12

VITA

Cheng Zhang was born in 1985 in the city of Anshan, Liaoning Province, China. Cheng received his primary and high school in Anshan, China. Cheng entered the University of Science and Technology of China in the city of Hefei, Anhui Province, China in August 2004. Cheng graduated with a bachelor's degree in Macromolecular Materials and Engineering in July 2008. Shortly after receiving his bachelor's degree, Cheng jointed the doctoral program under the supervision of Boyd Professor George Z. Voyiadjis in Engineering Science at Louisiana State University in August 2008. The completed research work is presented in this dissertation. Cheng Zhang has been involved in researches in several areas, such as the constitutive modeling of mechanical behaviors in metals in the submicron scales, nanoindentation experiments, sample preparations and multiscale simulations of solid materials. His future plans involve continued research on materials characterization with the aid of submicron scale testing, microscopy techniques and multi-scale modeling.